DYNAMICS AND PROCESSES DURING THE 1959 KĪLAUEA IKI ERUPTION

A DISSERTATION SUBMITTED TO THE GRADUATE DIVISION OF THE
UNIVERSITY OF HAWAI'I IN PARTIAL FULFILLMENT
OF THE REQUIREMENTS FOR THE DEGREE OF

DOCTOR OF PHILOSOPHY

IN

GEOLOGY AND GEOPHYSICS

MAY 2009

By
Wendy K. Stovall

Dissertation Committee:

Bruce F. Houghton, Chairperson
Julia E. Hammer
Sarah A. Fagents
Don A. Swanson
Gary M. Barnes

We certify that we have read this dissertation and that, in our opinion, it is satisfactory in scope and quality as a dissertation for the degree of Doctor of Philosophy in Geology and Geophysics.

DISSERTATION COMMITTEE

_____
Chairperson

_____

_____

_____

The important thing is to strive toward a goal which is not immediately visible.
That goal is not the concern of the mind, but of the spirit.
– Antoine de Saint-Exupéry

At start of spring I open a trench in the ground.
I put into it the winter's accumulation of paper,
pages I do not want to read again, useless words, fragments, errors.
And I put into it the contents of the outhouse: light of the sun,
growth of the ground, finished with one of their journeys.
To the sky, to the wind, then and to the faithful trees, I confess my sins:
that I have not been happy enough, considering my good luck;
have listened to too much noise;
have been inattentive to wonders;
have lusted after praise.
And then upon gathering refuse of mind and body,
I close the trench, folding shut again the dark, the deathless earth.
Beneath that seal the old escapes into the new.
– Wendell Berry

Someday after mastering winds, waves, tides and gravity, we shall harness the energies of
love, and then, for the second time in the history of the world, man will discover fire.
– Teilhard de Chardin

Happiness is the consequence of personal effort...participate relentlessly in the
manifestation of your own blessings.
– Elizabeth Gilbert

Thank you very much to my undergraduate mentor, Karen Grove, for pushing me toward excellence from the start.

I must give sincere and bursting heartfelt gratitude to my family. Thank you to my mother, Sandy Brown, who is my rock and my best friend. Thank you to my father, Bill Stovall, who bragged on me constantly and developed a fan club for me at his office. Thank you to my uncle, Steve Stovall, who sent me messages of encouragement and made me want to succeed. Thanks also to my stepfather, Terry Brown, for cheering me on and to my stepmother, Ti Stovall, for understanding what grad school is all about.

My friends are an extension of my family, thank you for believing in me for days, months, and years. Special thanks to all the house mates I've had in Hawai'i: Lisa Tam, Derek Payne (for seeing me through a lot of it), Lisa Swinnard, Malin Klawonn, Leila Marzeki, Scott Wishart and Chris Nepple. I am grateful for my outside of school friends, who attempted to understand me: Dori Mondon, Chris Marchetti, Robb Jeter, David Tibor, Sara Coppin (soulmate roommate), Erin Coppin, Susan, Simon, Isis and Theo Bird, Zach and Bekki Diener, and Brandon Olander. Extra special thanks to Andrea (Steffaine) Steffke, who went through this process with me as an amazing friend, a super house mate, a source of entertainment, and as someone I could always depend on to be real.

My health was greatly enhanced by help from Kareen Tanoue (pilates), the gym, Eiji Takeda (acupuncture) and Judy. Thank you all for your concern for my wellbeing.

Abstract

This dissertation examines aspects of the formation of the lava lake and pyroclastic products from the 1959 eruption of Kīlauea Iki, Kīlauea volcano Hawai'i. This short-lived but powerful eruption contained 17 fountaining episodes and produced a cone and tephra blanket as well as a lava lake that interacted with the vent and fountain during all but the first episode of the eruption.

The Kīlauea Iki lava lake includes relics associated with lake filling, draining and crustal overturn. The process of crustal overturn is driven by the advance of a flow front of fresh, low-density lava over an older, higher density surface crust. Density differences between foundering crust and over-riding and underlying lava were determined to be 200 and 740 kg m^{-3} respectively. Crustal overturn is driven by these large density differences between the foundering and resurfacing units. During every major explosive episode, fountaining lava ponded in the lake to levels above that of the vent before draining back into the conduit, during and at the close of the episode. Vertical rinds of lava coating the lava lake walls formed during lake-filling, as lava cooled and solidified against vertical faces. During drainage, horizontal lava shelves solidified against the lakeward edges of vertical rinds as relics of lake-surface crust or accretion at the surface of the lava lake.

Microtextural analysis of Hawaiian fountaining products from the opening and closing episodes of the Kīlauea Iki eruption are used to infer vesiculation processes within the fountain and shallow conduit. Vesicle number densities for all clasts are high ($10^6 – 10^7$ cm^{-3}) and scale with increasing fountain height. Post-fragmentation expansion of bubbles within the thermally-insulated fountain overprints the pre-fragmentation

bubble populations, leading to a reduction in bubble number density and increase in mean bubble size. However, early quenched rims of some clasts have vesicle-number densities approaching 10^7 cm^{-3}, probably a valid approximation to magma conditions near fragmentation. The extent of evolution of clasts from low vesicle-to-melt ratio and corresponding high vesicle-number density to higher vesicle-to-melt ratio and lower vesicle-number density corresponds to the length of residence time within the fountain.

Table of Contents

Chapter 3: Features of lava lake filling and draining and their implications for eruption dynamics

Chapter 4: Eruption dynamics of Hawaiian-style fountains: the case study of episode 1 of the Kīlauea Iki 1959 eruption

Chapter 5: High fountaining Hawaiian eruptions: episodes 15 and 16 of the 1959 Kīlauea Iki eruption

List of Tables

List of Figures

Chapter 5: High fountaining Hawaiian eruptions: episodes 15 and 16 of the 1959 Kīlauea Iki eruption

Appendix

CHAPTER 1

Introduction

1.1 Dissertation overview

This dissertation explores the nature of explosive and effusive products from the 1959 eruption of Kīlauea Iki, Kīlauea volcano, Hawai'i. Chapter 1 serves as the background information for the setting of the Hawaiian Islands, Kīlauea volcano and the eruption of 1959. Chapters 2 and 3 focus on surficial features of the lava lake that were emplaced during the eruption. Along the north margin of the lake, solidified relics of dynamic processes such as crustal overturn, lake filling, and lake draining are preserved. In chapter 2, a frozen record of crustal overturn is described and shown to be driven by density differences between cooled crust and underlying and overlying lava. In chapter 3, I describe and interpret vertical rinds of lava and lava shelves located along the northern margin wall of the lava lake in the context of lake filling and drainage during the final episodes of the Kīlauea Iki eruption. Chapters 4 and 5 use microtextural analysis of pyroclasts to interpret ascent and eruption processes during the opening and closing episodes of the Kīlauea Iki eruption. Chapter 4 focuses on episode 1 and provides insight into processes of post-fragmentation expansion of pyroclastic material occurring in a Hawaiian fountain. In chapter 5, vesicularity studies of episodes 15 and 16, the final two high-fountaining episodes of Kīlauea Iki eruption, examine constraints on extremely-high Hawaiian fountaining eruptions. These studies provide further understanding of the spectrum of eruption processes that are typical of Hawaiian volcanism.

1.2 Volcanological setting

The Hawaiian archipelago is located in the central Pacific Ocean and comprises eight

main islands centered near 20º50'N, 156º56'W (Figure 1.1). These islands are the young

subaerial expression of the Hawaiian-Emperor seamount chain that stretches from the

Aleutian Trench to Lō'ihi seamount, 35 km offshore from the island of Hawai'i.

Formation of the chain has been attributed to hotspot volcanism (Decker, 1987 and

references therein) whereby partial melting of the mantle occurs at $\geq$ 80 km depth with

buoyant rise of a plume through the lithosphere (Tilling and Dvorak, 1993). In this

theory, northwesterly movement of the Pacific plate over the melting region has resulted

in the formation of chain of basaltic seamounts and islands (Decker, 1987). The typical

life cycle of a Hawaiian volcano is a progression through stages of submarine shield-

building, subaerial shield-building, post-shield lava effusion, and eventual rejuvenation

involving eruption of relatively alkalic magmas (Macdonald et al., 1983).

The island of Hawai'i, or "The Big Island" (Figure 1.2), is the southernmost in the

Hawaiian chain centered over the mantle plume (Frey and Rhodes, 1983). This island is

made up of seven submarine and subaerial volcanoes. In order of decreasing age, the

volcanoes are Mahukona, Kohala, Mauna Kea, Hualalai, Mauna Loa, Kīlauea and Lō'ihi

(Moore and Clague, 1992). The oldest and youngest of these are submarine volcanoes.

Mahukona was once subaerially exposed, but due to erosion and subsidence, it is now

below sea level (Moore and Clague, 1992). Kohala, Mauna Kea and Hualalai are in the

post-shield stage of volcanism; the latter is the most active of this group (Macdonald et

al., 1983). Mauna Loa and Kīlauea are the subaerial-shield-building volcanoes on the

island of Hawai'i and erupt primarily tholeiitic basalt (Macdonald et al., 1983). Recent

studies of isotopic variation in erupted lavas from Mauna Loa and Kīlauea volcanoes

indicate that the melting region which feeds the Hawaiian hotspot plume is only 5–10 km

wide at depth based on interpreted incorporation of small-scale compositional

heterogeneities (Marske et al., 2007).
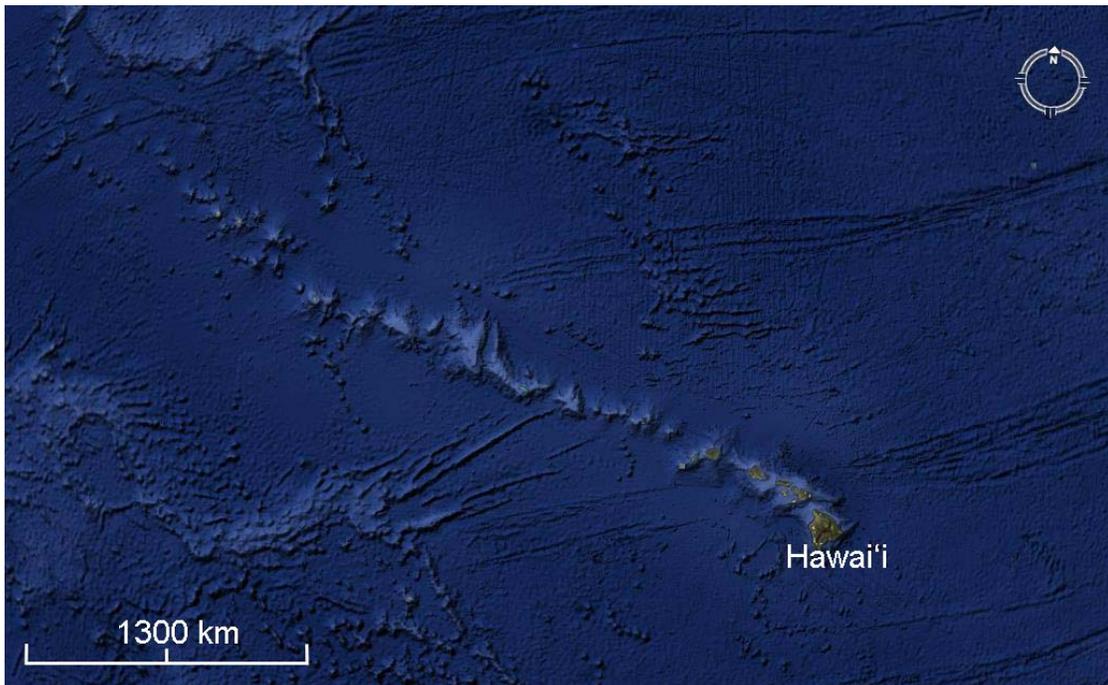
Figure 1.1 Map of Hawaiian archipelago**.**
Island of Hawaiʻi labeled; map made using Google Earth.

1.3 Kīlauea volcano

1.3.1 Plumbing system geometry
Kīlauea volcano is the southeastern-most of the five subaerial volcanoes, and much of

what is known today is based on the fundamental study of Eaton and Murata (1960). It is

the most active of all volcanoes on the island (Decker, 1987; Tilling and Dvorak, 1993)

and, as of March 2009, has been in continuous eruption since 1983 (Heliker and Mattox,

2003; Poland et al., 2008). The magma pathway beneath the volcano has been defined by

earthquake foci and indicates a pipe-like vertically-oriented feature in the lithosphere

3

(Tilling and Dvorak, 1993 and references therein). Between 20 and 7 km depth the seismically defined feature narrows and extends into an aseismic zone between 7 and 2 km depth (Tilling and Dvorak, 1993). The location for the summit magma storage region is within this zone and, based on geodetic measurements, is inferred to be 1–4 km deep and approximately 1–2 km southeast of Halemaumau pit crater (Cervelli and Miklius, 2003; Fiske and Kinoshita, 1969; Yang et al., 1992). The geometry of Kīlauea's shallow magma reservoir is debated, with arguments for either a plexus of dikes and sills (Fiske and Kinoshita, 1969) or a continuous, somewhat-spherical molten body (Yang et al., 1992). Pietruszka and Garcia (1999) argue for a simple geometry with a molten core surrounded by crystal mush, based on systematic changes in trace element abundances and isotopic ratios among historic summit lavas.

1.3.2 Eruption dynamics and types of activity

1.3.2.1 Vesiculation of ascending basaltic melts

Basaltic explosive activity occurs frequently at volcanoes such as Stromboli and Etna in Italy as well as Kīlauea (e.g., Chester et al., 1985; Chouet et al., 1997; Parfitt and Wilson, 1995). Vesiculation drives the magmatic explosivity of these large and long-lived basaltic systems. The explosivity of an eruption at any given time is thought to reflect the amount, depth, rate and style of degassing that has occurred in the magma during its ascent. A key factor is whether the system can be regarded as open or closed with respect to the exsolving vapor phase. Large bubbles are able to rise freely through the melt in open-system degassing due to mechanical decoupling of the volatile phase from the melt.

4

In closed systems, the volatiles remain coupled with the melt, and gas is not lost during

ascent prior to fragmentation.
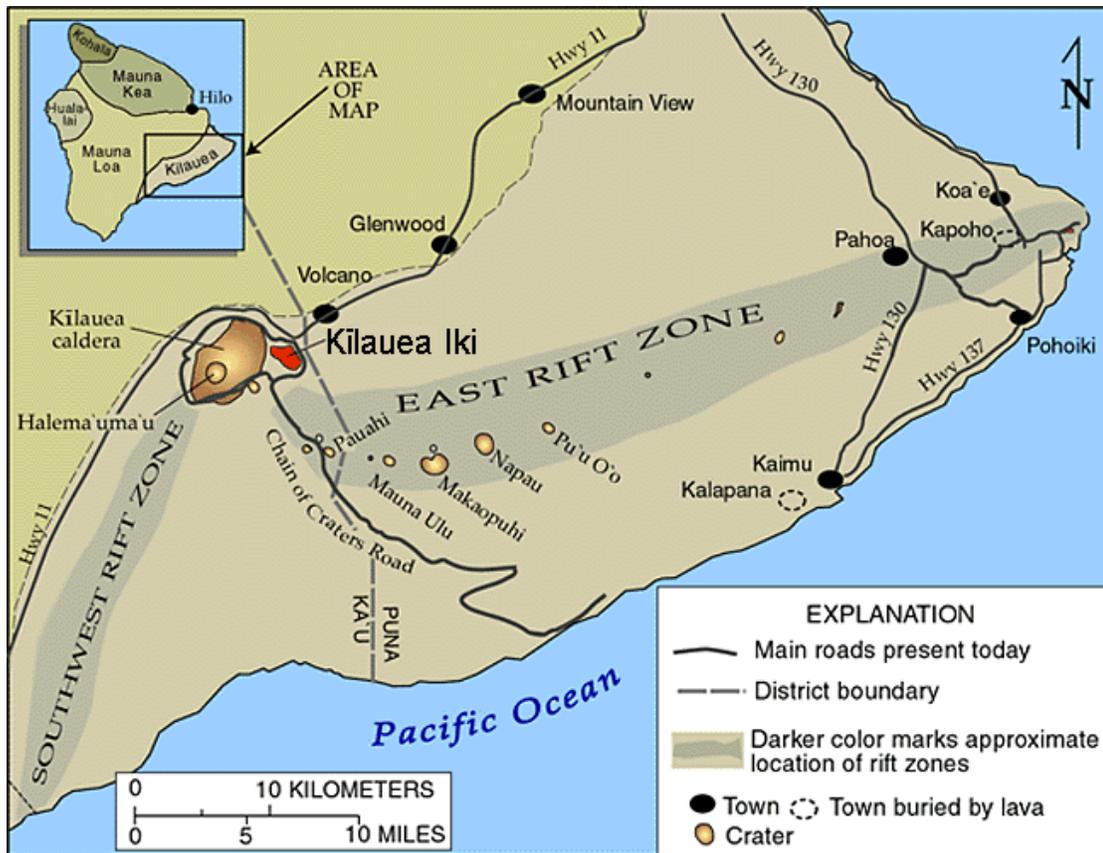
Figure 1.2 Map of Kīlauea volcano and the island of Hawaiʻi.
Map showing the summit caldera and Kīlauea Iki pit crater, southwest and east rift zones with associated craters (after Johnson 2000).

Purely effusive eruptions involve no explosivity and are defined as a quiet

outpouring of largely outgassed lava. In basaltic systems it is rare to find a solely

effusive eruption, as most are mixed, containing some form of explosive activity

(Macdonald 1972). Volcanoes exhibiting eruptions with mixed histories of both lava

effusion and violent explosions indicate that magma reaching the surface can follow a

range of different ascent histories and paths even in the course of single eruptions (Eichelberger, 1995; Eichelberger et al., 1986).

Within the conduit during basaltic eruptions, there is some degree of differential motion between gas and melt (Jaupart, 1996). Contrasting patterns of rise between gas and melt are used to distinguish end member styles of explosivity such as semi-sustained Hawaiian fountaining and discrete Strombolian explosions (e.g., Cashman and Mangan, 1994; Head and Wilson, 1987; Head and Wilson, 1989; Jaupart and Vergniolle, 1989; Parfitt and Wilson, 1995; Vergniolle and Mangan, 2000; Wilson and Head, 1981). In Hawaiian explosive eruptions melt rises rapidly through the conduit, so that the period of bubble nucleation and growth is short. Therefore, degassing is typically a late-stage process, forcing nucleation of a large population of relatively small bubbles coupled with the melt, which are preserved in the ejecta (Mangan et al., 1993).

1.3.2.2 Hawaiian fountaining
A lava lake is defined as a volume of ponded lava. Classic long-lived examples are found at Kīlauea volcano in Hawai'i, Mount Erebus in Antarctica, Erta Ale in Ethiopia, and Nyiragongo in Zaire. They are a rare volcanic occurrence and are formed in a variety of ways. An active lava lake is formed in one of two ways: (1) ponding above an active vent that erupts long enough to form its own lake containment crater or (2) within an existing crater, containing a single or series of vents, which erupts enough lava to partly fill that crater (Swanson et al., 1973). A topographically ponded lake is formed when lava pours into a pre-existing crater, spatially separated from the source vent.

Lava lakes formed above active vents exhibit a variety of dynamic eruption patterns. A primary fountain is typically located over the supply vent but short-lived secondary fountains can occur as a result of gas release associated with crustal foundering (Macdonald, 1972). The surface of the lake rises and falls depending on the flux of magma from the conduit (Tilling, 1987). Some lakes can remain active for tens to hundreds of years while maintaining a relatively stable volume (Macdonald et al., 1983; Tazieff, 1994).

Topographically ponded lakes are much less dynamic than those formed above active vents. After the flow of lava into the previously formed crater ends, the lake begins to stagnate and cool in place. The lake solidifies due to heat loss from the top, sides and bottom, and complete solidification time depends on the volume occupied by the lava (Peck 1978). The lava lake formed during the 1959 eruption of Kīlauea Iki is an interesting case study, because it originated as a topographically ponded lake, but once the lake level rose to the height of the vent it became an active lava lake.

1.3.2.3 Basaltic lava lakes
Kīlauea volcano is the type locality for Hawaiian fountaining behavior (Walker, 1973) and is considered an exemplary natural laboratory for the study of basaltic volcanology. Typical eruptions at Kīlauea are either short, single episodes of fountaining and lava effusion, prolonged periods of quiet, effusive eruptions, or cycles of explosive eruptions that accompany effusive events (Vergniolle and Jaupart, 1990).

Currently there are two models that explain the occurrence of Hawaiian fountaining. The Vergniolle-Jaupart (i.e., collapsing foam) model links the fountaining

7

to collapse of a foam layer that forms along the upper surface of a magma chamber. When the foam reaches a critical thickness it coalesces into a gas pocket and rises buoyantly through the conduit, displacing the melt phase. When this annular flow of gas plus melt reaches the free surface it bursts through the interface and erupts in relatively continuous fashion (Jaupart and Vergniolle, 1988; Jaupart and Vergniolle, 1989; Vergniolle and Jaupart, 1986; Vergniolle and Jaupart, 1990; Vergniolle and Mangan, 2000). The second, Wilson-Parfitt (i.e., rise speed dependent) model explains Hawaiian fountaining as rapid ascent of coupled gas and melt. This mixture rises through the conduit so quickly that, during the later stages of ascent, only limited gas loss can occur prior to fragmentation (Head and Wilson, 1989; Parfitt and Wilson, 1995; Wilson and Head, 1981). Recent experiments by Naminki and Manga (2008) suggest fragmentation of liquids like basaltic magma is a function of inertial forces imparted during expansion and the resultant feedback of further expansion which leads breakup of the fluid.

Throughout the historic record of long-lived Hawaiian eruptions, there has been a recurring pattern of eruptions that consist of multiple fountaining episodes separated by periods of quiescence (Heliker and Mattox, 2003; Richter et al., 1970). Scientists studying the cyclicity of episodes have developed several alternative models. Dvorak and Okamura (1987) suggest that in order to sustain lava fountaining a differential pressure threshold must be exceeded between the magma reservoir and the conduit. Vergniolle and Jaupart (1990) model a process of pulsed gas-flux-dependent collection, collapse and violent eruption of foam in the upper surface of a magma chamber. Mangan and Cashman (1995) suggest that the cessation of episodes at Puʻu ʻŌʻō is related to

8

conduit wall cooling and resultant narrowing, which is amplified by the drain back of lava ponded above the vent. Drain back of lava in latter stages of Hawaiian episodes is modeled by Wilson et al. (1995) to cause a switch from lava fountaining to discrete Strombolian explosions.

1.4 Kīlauea Iki 1959 Eruption

1.4.1 Chronology

At 8:08 p.m. on November 14, 1959 a summit eruption of Kīlauea volcano began in Kilauea Iki crater. Rising magma opened nine vents along a ~900 m fissure on the south wall of the pre-existing collapse crater. Fountains reached up to ~30 m in height before cascading down ~100 m to pond as lava at the base of the crater. By the afternoon of the 15th, the outermost vents ceased activity and the eruption was centered in a single location near the western end of the crater (Figure 1.3). The flux at this vent increased and fountain heights surged to ~350 m by the fifth day of the eruption, while the lake at the bottom of the crater rose at a rate of one meter per hour. On November 21, the lake was ~102 m deep and had reached the level of the vent; fountaining ceased and lava immediately began to drain from the lake, back down the vent.

Figure 1.3 Photograph of the opening episode of the Kīlauea Iki eruption. Kīlauea Iki fountain, height ~100 m. Lava is seen pouring from base of the fountain and streaming toward the photographer and ponding in the eastern side of the Kīlauea Iki pit crater. Photo by Don Richter housed in USGS HVO library.

The cycle of fountaining, lake filling, fountain cessation and drainback continued

for 16 more episodes. All were shorter and erupted smaller volumes than the first

episode, but fountaining was significantly higher during several of the later epsiodes.

Additionally, each of the episodes varied in style of fountaining (inclined, vertical, or

bifurcated: Figure 1.4), duration of activity (hours to days), and duration of quiescence

between episodes. In addition to lake drainback, inner parts of the cone sloughed off and

fell back into the vent during the closing phases of many episodes. Finally, on December

20 at 8:00 p.m., the last lava flowed out from the vent and covered ~10^4 m^2 of the old

lake surface. The eruption was over, and on December 23, the last period of drainback

ended. Based on frequent measurements throughout the eruption, the maximum depth of

the lake was estimated to be ~111 m. However, subsequent drilling into the lake by Helz

(1993) indicates the depth may have actually been 135 m deep.

Figure 1.4 Photograph of Kīlauea Iki eruption with bifurcated first-episode fountain.
Fountain depositing tephra to the left is forming Puʻu Puaʻi cone. Tephra falling from
the fountain back into the crater forms a lava river that terminates at the bottom of the
photograph as a lava lake.

1.4.2 Literature relating to eruption chronology
The 1959 eruption of Kilauea Iki has inspired research resulting in the publication of

many papers, creation of three films, and a cataloged collection of slide photographs

taken at the time of the eruption. A detailed history of episode characteristics has been

recorded by Macdonald (1962), Richter et al. (1970), and Eaton et al (1987). U.S.

11

Geological Survey Professional Paper 537 is a five-paper series chronicling the complete eruption narrative, as well as chemistry, fumarolic gas, petrography, and petrology of the erupted products (Murata, 1966; Murata and Richter, 1966; Richter et al., 1970; Richter and Moore, 1966; Richter and Murata, 1966). These published papers are the starting point to this dissertation research. In addition to these published works, a copy of Jerry Eaton's and Don Richter's unpublished original field notebooks plus an eruption log compiled by HVNP staff have been used in this study. These sources include extremely detailed measurements of fountain heights and lake levels, discuss features of the lava lake, and give a history of the cone growth. Two of the three films were made privately by film-makers Rackle and Wakida, and the third was made by the USGS and National Park Service. The USGS Hawaiian Volcanoes Observatory holds the catalog of slide photographs taken by Jerry Eaton and Don Richter. The slides are labeled with day, time and a brief description of what was photographed. These published and non-published materials make an excellent database of resources from which this dissertation research greatly benefited.

1.4.3 Geometry of the Kīlauea magmatic system in 1959
Prior to 1959, magma entered the summit reservoir of Kīlauea and was stored for a number of years before it mixed with newly arrived melt and was erupted at Kīlauea Iki (Wright, 1973). Many petrological and geochemical studies have been undertaken in order to understand the magmatic system associated with the Kīlauea Iki eruption (Anderson and Brown, 1993; Eaton, 1962; Eaton and Murata, 1960; Eaton et al., 1987; Helz, 1987; Helz and Thornber, 1987; Mangan, 1990; Wright, 1973; Wright and Fiske,

1971). The research suggests newly arrived magma rose from a depth of 40 to 60 km in

August 1959. By September 1959, it entered the summit reservoir at ~2-5 km depth and

in mid November magma reached the surface at Kīlauea Iki. Eaton et al. (1987)

completed a thorough study of the volumes of lava erupted and drained during each

episode and correlated those with contemporary geophysical data from the eruption. The

following account is a summary of their interpretation of the dynamics of magma

transport at Kīlauea Iki. Throughout the eruption a "lava conduit" remained open,

connecting the vent to the summit reservoir. Eaton et al. (1987) explain that magma from

the reservoir was pumped into the Kīlauea Iki vent through a process of intense

vesiculation. The removal of this lava from the reservoir system reduced the internal

pressure creating a hydraulic forcing, which increased the flow of magma from depth into

the summit reservoir. When outgassed lake lava reached a level above the mouth of the

feeder vent, it found a way back down the "lava conduit" and into the reservoir. This

altered the behavior of the rising vesiculating melt and caused fountaining to end. Post-

fountaining lava-lake drainage into the conduit acted to reinflate the reservoir. Tilt

measurements indicate magma continued to rise into the summit reservoir from depth

after the episodes 1–16 fountaining phases ended, which provided a fresh gas-rich

magma supply. The combination of 1) continued injection of gas-charged magma from

depth and 2) drainback of lake lava after fountaining ended acted to increase the reservoir

pressure sufficiently to force lava up the open conduit thus initiating subsequent episodes.

Due to this dual recharge mechanism, the reservoir in later episodes was so full that some

fraction of drainback lava and reservoir magma was injected into an adjacent dike-like

13

zone, as indicated by a period of resurgent tremor. It is probable that this zone acted as a pathway for magma to enter the east rift zone, and therefore, ended the cycle of reservoir overpressure that had been producing episodic fountaining.

1.4.4 Previous studies of fall deposit geometry

Background studies associated with 1959 tephra blanket include contemporary measurements and subsequent analyses of grain size and stratigraphy. Unpublished field notebooks from Jerry Eaton and Don Richter contain depth measurements of Kīlauea Iki tephra taken at multiple locations after episodes along a cross-wind traverse 1, 3, 11 and 16; a summary was published in Richter et al. (1970). These measurements aid in reconstruction of specific episode stratigraphy when examining present-day tephra pits. Parfitt (1998) studied the whole-deposit grain-size distribution of the Kīlauea Iki tephra by measuring total thickness in multiple locations and collecting maximum clast measurements. This study was limited, however, by examination of the deposit as a whole rather than by episode and by, commonly, only incorporating maximum-sized clasts from the upper layer of the deposit. Results from this study indicate that the fountaining eruptions produced very-coarse clast size distributions as a whole. Based on this grain-size study, Parfitt and Wilson (1999) modeled the Hawaiian fountaining eruption as a Plinian eruption column and determined that the two eruptive styles are dynamically similar, with differences in the deposit arising out of contrasting gas content and mass flux.

Bruce Houghton, Sarah Fagents, and Don Swanson conducted field studies of the tephra blanket in preparation for the macro- and microscopic examination of Kīlauea Iki

pyroclasts included in this dissertation. Their investigations, as yet unpublished, clarify isopach thickness, variations in stratigraphy at different locations throughout the tephra blanket, and deposit grain size. This work supplied the framework for sampling to evaluate sample componentry and density, and clast microtextures, including vesicle size distributions and variation in the concentration of small-scale crystals.

1.5 Dissertation Structure

Chapter 2 details a frozen record of the final crustal overturn event of Kīlauea Iki lava lake. Seven lava components associated with a crustal foundering event were identified and sampled from the lake surface. Based on field relationships and comparative laboratory density measurements, contrasts between higher-density surficial plates and lower-density overriding and underlying molten lake lava were determined to be the driving factors in crustal foundering and eventual wholesale crustal overturn. This chapter was published in Bulletin of Volcanology in 2008 (volume 71, pages 313-318, doi: 10.1007/s00445-008-0225-y).

Chapter 3 focuses on description and interpretation of features found on the north margin wall of Kīlauea Iki lava lake inferred to have formed during filling and draining cycles. Each episode of the eruption was characterized by a phase of fountaining and lake filling followed by a phase of drainage and lowering of the lava lake. Multiple layers of vertically-oriented rinds of lava veneer the wall and were emplaced during lake-filling phases. Horizontal lava shelves were then plastered or accreted on the lake-facing surfaces of vertical rinds and record periods of both rapid and staged lake lowering

during drainback phases. This work was published in *Bulletin of Volcanology* 2009 (doi: 10.1007/s00445-009-0263-0).

Chapter 4 of this dissertation uses quantitative macro- and microtextural analysis of the pyroclastic products from the first episode of the Kīlauea Iki eruption to infer vesiculation dynamics within the lava fountain and shallow conduit. Single clasts with heterogeneous vesicle populations are the key to understanding the origin of textural variability in clasts with homogeneous vesicle populations. Heterogeneity of clast textures is determined to be a function of variable degrees of post-fragmentation expansion due to the positioning, varying trajectory and therefore, the residence times in the Hawaiian-style fountains. This chapter will be submitted for publication in *Bulletin of Volcanology*.

Chapter 5 builds on the study of chapter 4 using clasts from episodes 15 and 16, the late, high-fountaining episodes of the Kīlauea Iki eruption. Among individual clasts, trends of decreasing vesicle number density correlate precisely with increasing vesicle to melt ratio implying post-fragmentation coalescence and growth of vesicle populations. This chapter will also be submitted for publication in *Bulletin of Volcanology* as a companion paper to chapter 4.

Chapter 6 summarizes the conclusions of the earlier chapters and draws upon the relationship between Hawaiian fountaining and lava drainback to formulate questions that may be addressed with future research

CHAPTER 2

A frozen record of density-driven crustal overturn in lava lakes: the example of

Kīlauea Iki 1959

2.1 Introduction

Lava lakes have been recorded at numerous basaltic volcanoes including Kīlauea (Flynn

et al., 1993; Jaggar, 1947; Richter et al., 1970; Swanson et al., 1973; Wright and

Okamura, 1977), Nyiragongo (Tazieff, 1994), and Erta Ale (Harris et al., 2005) and on

other planetary bodies, e.g., Triton (Schenk and Jackson, 1993) and Io (Rathbun et al.,

2002). Crustal overturn has been documented at all of the above mentioned terrestrial

lava lakes and can proceed as a sudden event resulting from wholesale foundering of the

lake surface that terminates a period of stable crust formation (Flynn et al. 1993) or

localized foundering of individual plates (e.g., Wright et al. 1992. p117). This occurs

alongside steady convection which involves crust formation at up-welling zones which

then moves steadily across the lake surface to be consumed at sinks in a plate-tectonic-

style motion (Duffield 1972). The focus of quantitative models for dynamic motion of

lava lakes have been based on thermally driven convection in lakes with stagnant lids

which thicken with time and do not overturn (e.g., Worster et al., (1993). Such a scenario

fits stagnant cooling lakes with time, but not those undergoing almost continuous surface

renewal (e.g. Duffield, 1972; Harris et al., 2005). At active lava lakes, i.e., those fed by a

vent directly below the lake, the overturn process proceeds to completion, leaving no

physical evidence of the foundering event and hence limiting our ability to constrain

inputs into models of the process. In addition the close of eruptive activity is generally

accompanied by magma withdrawal and lake collapse, thereby possibly destroying

surface crust features associated with overturn. In contrast, inactive lava lakes fed by

vents adjacent to the lake typically have shorter lifetimes, limited lava withdrawal, and

therefore significantly higher preservation potential for surface features associated with

crustal motion.
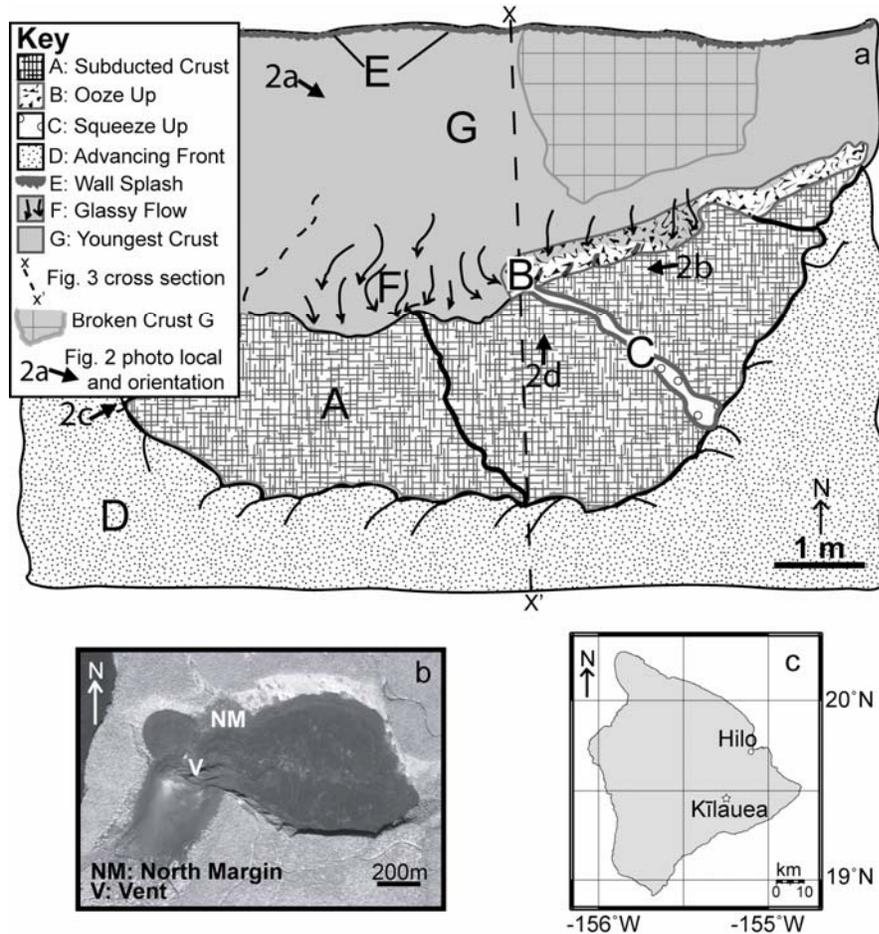
Figure 2.1 Kīlauea Iki lava lake study area, IKONOS image of lake and map of Hawaiʻi.
Kīlauea Iki lava lake study area with north margin (NM) and vent (V) locations
highlighted. (**a**) Map showing each unit. The boundary between G and F is a surficial
transition from broken and shelly to smooth, intact and glassy lava respectively (Figure
2c). Broken crust G is the region where G is fractured and dropped down. (**b**) Location on
north margin of lava lake. (**c**) Location on island of Hawaiʻi. Sequence of events that led
to assemblage along X-X' is recreated in Figure 2.3.

The Kīlauea Iki lava lake contains an easily identifiable frozen record of crustal foundering (Figure 2.1). Based on field descriptions and samples taken from the density-stratified components of the final crust that formed on the 1959 Kīlauea Iki lava lake, we present evidence showing how density contrasts between degassed surface plates and the underlying and overriding lake lava can drive overturn, the density difference causing the surface crust to founder. Such a density-driven model of lake overturn is supported by observations of Alae lava lake (Swanson et al. 1973) where "a density inversion caused by gas-rich lava collecting beneath the solid crust generated several spectacular episodes of crustal overturning…" and Makaopuhi lava lake (Shaw et al., 1971) where "foundering…is related to gravitational instability caused by accumulation of rising gas bubbles beneath the crust." Our data show a substantial density contrast between the foundering crust as well as both the overriding front of lava and bubble-rich sub-crustal lava, which promoted sinking of the older crust.

2.2 The 1959 Kīlauea Iki eruption

The 1959 eruption of Kīlauea Iki, Hawai'i, emplaced an ~46 x 10^6 m^3 lava lake in a pre-existing pit crater (Richter et al., 1970). Most of the time, the lake was simply a ponded lava below the level of the vent which formed, following the definition of Swanson et al. (1979), an inactive lava lake. Unlike active bottom-fed lava lakes, Kīlauea Iki was fed from a vent on the crater wall which interacted with the lava lake during each of 17 eruption episodes only when the rising, fountain-fed lake overtopped and flooded the vent. Crustal overturn was recorded repeatedly throughout the eruption, taking place during both filling and draining of the lake (Richter et al., 1970). The overturn process

19

was comprised of localized events that often led to "wholesale foundering of the crust" where opening of subsequent cracks "allowed brightly incandescent lake lava to well up and over-run a small area of the surface before solidifying. In this manner an entirely new surface crust was formed…" (Richter et al. 1970). Because of decreased momentum of lava movement toward the vent during the final stage of lava drainage, the lake dynamics likely slowed and began to stagnate. This caused the surface, which had previously been in constant motion, to freeze and effectively preserve the final, incomplete, overturn cycle.

2.3 Description of Units
An excellent example of this frozen overturn is evident on the northern margin of the Kīlauea Iki lava lake ~200 m from the vent (Figure 2.1). We divided the area forming the surface of the frozen overturn into 7 units (A through G, in order of time of formation, Figure 2.1).

The center of the exposure is a low-lying 13 m^2 area of flat-surfaced pāhoehoe (A, Figures 2.1, 2.2a) cut by cracks, some of which are occupied by round vesicular buds of lava extruded up into the crack base (C, Figures 2.1, 2.2a). Attached to and protruding from A, a 3.0 m-long lava block (B, Figures 2.1, 2.2a-d) forms a half-cylinder whose flat sides fit, jigsaw fashion, with a similar structure (B', Figure 2.2d) attached at a height of 1.1 m to the crater wall. To the south, A is covered by a bulbous, inflated, pāhoehoe flow front (D, Figures 2.1, 2.2a). D extends at least 50 m southward into the lake and has a surface broken by a network of polygonal cracks that, following Peck and Minakami (1968), initially formed during thermal contraction and subcrustal lava flow. The

20

northern edge of A is overlain by a zone of smooth-skinned pāhoehoe (F, Figures 2.1,

2.2a-d) with a surface fabric indicating flow directions (marked on Figure 2.1). The

surface between F and the wall (i.e., to the lake edge) is shattered into a shelly pavement

(G, Figures 2.1, 2.2c) and contains a 1 m^2 window of broken and down-dropped crust

(hatched area, Figure 2.1) exposing the interior cross section of the slab. Lava from F

laps onto B (Figure 2.2a) with a texture reminiscent of blue glassy pāhoehoe (Oze and

Winter, 2005). The lower 40 cm of the crater wall just above the lake surface is coated

with 5–20 mm of smooth lava adorned with frozen drips (E, Figures 2.1, 2.2d).
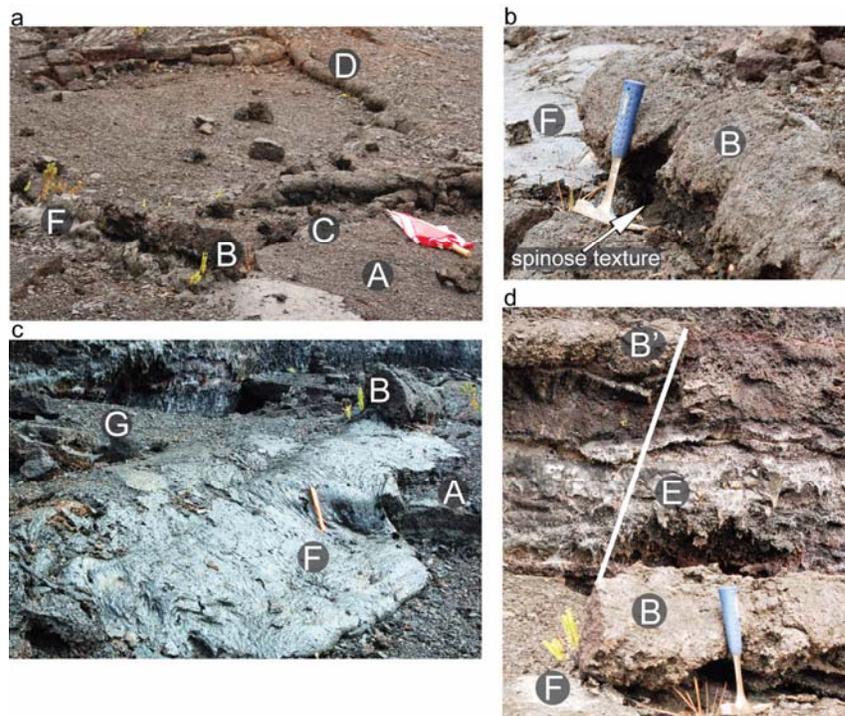
Figure 2.2 Photographs of crustal foundering study area on lava lake surface.
A through G indicate same units as in figure 2.1. Line connects matching faces of the
same unit in **d**.

2.4 Interpretation of Units

The spatial relations of these units allow us to interpret the nature and timing of the

foundering event that led to their final arrangement. The oldest unit, A, is overlain or cut

21

by all other features. This is the crustal plate that was foundering at the time of freezing. B is attached to this plate at its shore-facing edge. B has a face that matches B' perfectly, so that we infer both B and A were once attached to the wall more than 1 m higher than their current position. B is ooze-up emplaced at the former contact between the lake surface crust and the crater wall. The surface fabric of B points SW toward the vent (Figure 2.2b); the direction of drainback. Our interpretation is that the mature crust (A) formed while the lake was draining back into the vent and pulled a few centimeters or less away from the wall. This created a pathway for underlying lava to rise into the opening between the plate and the wall thereby forming a bulbous 'ooze-up' (B) on top of the lake crust. The mature crust (A) fractured, allowing molten lava under the plate to squeeze up into the cracks (C). D is the inflated flow front of a pāhoehoe sheet moving across the surface crust of A displacing the crustal plate downward, which foundered into the lake. F overlies A and runs up onto its attached block of ooze-up lava forming a 1 cm coating of smooth-skinned blue glassy pāhoehoe, suggestive of quite rapid emplacement followed by quenching of fluid, but relatively degassed, lava. Movement of A away from the wall exposed fluid lake lava (F) which washed against the existing units and splashed against the crater wall (E). The newly exposed incandescent lava cooled to form the youngest crust in the study area (G).

2.5 Sequence of Events
As lake cooling proceeded, a plate of crust formed that was loosely attached to the lake's north margin wall. The crust was slowly pulled away from the wall during drainback, allowing fluid lava under the crust to ooze up through the crack opening at the wall

22

contact (Figure 2.3a). During lake lowering, plate motion toward the vent created aligned textural features in B that point toward the vent (Figure 2.2b). Eventually the crust broke into smaller plates, and fluid lava rose through the crack openings and onto the surface of the overlying plate forming sutures such as C. Continued draining of the lake developed a void between the crust still attached to the wall and the sinking melt below, so that the crust formed a hanging roof over an empty cavern. The creation of this space initiated lake-ward tilting of the plate, so that it began to detach from the ooze-up structure (Figure 2.3b). This viscous tearing resulted in the peeling and stretching of plastically behaving lava yielding a spinose texture (Figure 2.2b) along the contact between surface crust A and the base of ooze-up structure B. A front of pāhoehoe advanced onto the surface of A and caused complete detachment of this wall-anchored slab, displacing it out into the lake and initiating subduction (Figure 2.3c). In some places the ooze-up was carried with the plate, but in others it was left behind as a relict shelf (B', Figure 2.2d). When units A and B broke away from the wall, they fell into the fluid lava. This splashed onto the wall, forming the splash features (Figure 2.3c) and causing fluid lava of unit F to wash up onto the ooze-up attached to the oldest crust. The newly-exposed, relatively degassed lava also flowed across and rapidly quenched against the down-going plate to form a lobe of blue glassy pāhoehoe. Continued advance of the pāhoehoe front over A displaced the plate further out into the lake, causing a zone underlying lava to be exposed (G). The lake froze before consumption of the foundering plate was complete, capturing the final overturn event.
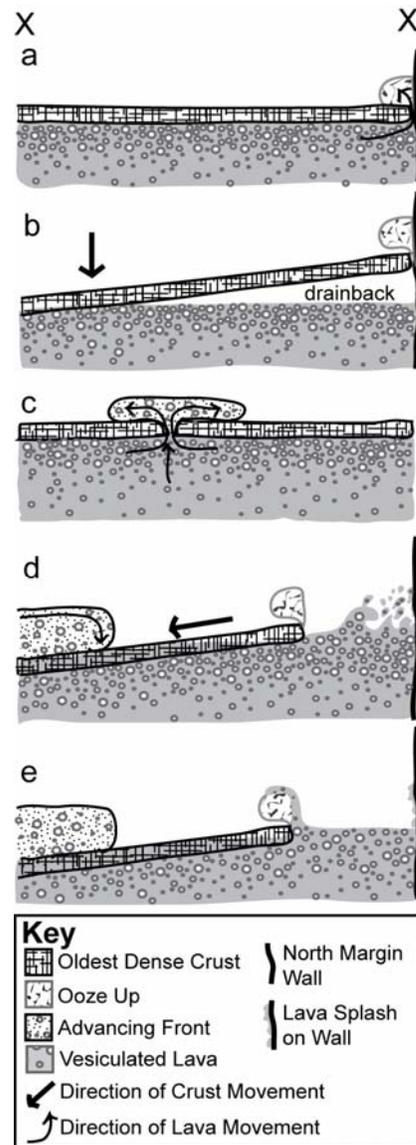
Figure 2.3 Cartoon of crustal foundering process.

Summary of processes during overturn at north margin of Kīlauea Iki lava lake. X and X' indicate cross section in Figure 2.1 (except in **c** as indicated below). Circles denote bubbles within lava and indicate vesicular nature of advancing front and accumulation of foamy layer toward top of lake. (**a**) Crust forms on surface of cooling lake, and lava oozes into opening between crust and crater wall. (**b**) Drainback of lava into vent beyond left edge of diagram results in lake-ward tilting of crustal plate. (**c**) At unknown distance from wall, underlying bubbly lava squeezes up between two crustal plates forming an advancing front that flows across lava lake surface. (**d**) Weight and force of advancing flow pulls plate and attached ooze from wall; plate falls into lava causing splashing. (**e**) Lake lava washes onto ooze attached to subducting plate, and area of open lava cools as foundering crust is pulled further into lake.

24

2.6 The Overturning Process

We envision a five-step crustal overturn process. First, the lake surface cools by

radiation and forms a crust. The crust is not stationary and stagnant but moves, driven by

convection within the lake (e.g., Duffield 1972; Harris et al. 2005) and/or, in our case, by

drainback toward the vent. Second, zigzag fractures form within the crust (Karlstrom and

Manga, 2006), creating polygonal plates (Peck and Minakami, 1968), which can also

suffer brittle failure due to stresses during motion. Both processes result in formation of

brittle, dense, surface plates. Third, the plates are pulled apart and lower density sub-

crustal lava rises through the cracks onto the plate surfaces. Fourth, some of the rising

lava forms a flow that advances across the cooler, denser crustal plate. This plate is

foundered downward into the lake by an advancing front, exposing large areas of

incandescent lava. The freshly exposed lava and advancing front form new crust, and the

process begins again. As observed by Richter et al. (1970), the whole lake experiences

overturn and crustal renewal via this process.

2.7 Mechanisms for Overturn and Crustal Foundering

Due to radiative cooling, lava lakes form surface crusts as soon as the lava is exposed to

air. Further cooling causes this crust to thicken with the square root of time (Hon et al.,

1994; Peck, 1978; Turcotte and Schubert, 2001). Crustal fracturing and plate

development then occur due to motion from convection (Duffield, 1972; Karlstrom and

Manga, 2006) and/or drainback (Richter et al., 1970). Then, density-driven foundering of

the cooled crustal plates occurs due to density contrasts. We described this process from

an interpretation of field relations but now quantify the density difference between the

foundering plate and the overriding (and underlying) lava.

25

Table 2.1. Bulk density of foundering units, Kīlauea Iki lava lake.

Figure 2.1 Label	Feature Interpretation	Number of Samples Measured	Bulk Density (kg/m³)	Standard Deviation (kg/m³)[a]
A	Subducted crust	8	1452	151
B	Ooze-up	9	1341	93
C	Squeeze-up	5	1084	76
D	Advancing front	12	1253	103
E	Wall splash[b]	9	1956	187
F	Glassy flow	11	715	442
G	Youngest crust	6	1163	71

[a]Standard deviations are near 10% except for Unit F where the samples collected are relatively heterogeneous and contain a broad size-range population of macroscopically visible vesicles.
[b]Unit E exhibits the highest density likely due to the violent ejection of lava from the lake which disrupted bubbles and permitted outgassing of the lava.

Samples of the 7 units within the study area were used to measure bulk density. We collected multiple 4 to 15 cm-diameter samples of each unit that span the range of visible macroscopic textures. Density measurements were made of each of the samples by wrapping them in wax and weighing them in water using Archimedes' principle (Houghton and Wilson, 1989). These data (Table 2.1) reveal the maximum and minimum density differences associated with units involved in density-driven overturn. The mean density of the foundering crust is 1452 kg m^{-3}. The mean density of the overriding pāhoehoe front is 1253 kg m^{-3}, yielding a density difference of 199 kg m^{-3}. The glassy flow originating from under the surface crust just prior to overturn was rapidly quenched by air; therefore, we believe its 715 kg m^{-3} mean density represents that of the underlying lava and yields a density difference of 737 kg m^{-3}. Thus, the measured density difference between units involved in crustal overturn at Kīlauea Iki is between 200 and 740 kg m^{-3}.

2.8 Conclusion

Density-driven overturn is a common process that occurs at scales from those of global tectonics to active lava lakes a few hundred square meters in area. Within lava lakes, the density difference between plates of lake crust and underlying fluid lava is thought to be responsible for initiating the process of crustal foundering and, eventually, complete surface renewal (Helz, 1993; Peck and Minakami, 1968; Swanson et al., 1973). Helz (1993), for example, suggested that overturn results from an accumulation of frothy lava at the crust-molten lava boundary which eventually leads to plate subduction. Additionally, drill cores from Kīlauea Iki indicate a repository of foundered crust in the upper 10 m of the lake (Helz, 1993) suggesting that a vertical stratification of increasing density to denser underlying lava resulted in a depth (and corresponding critical density value) at which foundering crust was neutrally buoyant and thus no longer able to sink. The lava lake gas-pistoning model of Witham and Llewellin (2006) is density driven, with low-density, bubble-rich magma pushing the lake level upward as bubbles rises through the overlying, denser, magma column. However, until now no measurements have been available for the density differences associated with lava lake overturn. Our observations are consistent with a front of lower density lava overriding a cooled, higher density crust, causing it to founder and sink into, and through, the even lower density lava below. Consistent with observations at other Kīlauea lava lakes, the overriding front originates from the subcrustal frothy layer. Our measurements show that it is not difficult to generate density differences of several hundred kg m^{-3} between sinking and overriding units, which makes overturn not just probable, but inevitable.

27

Acknowledgements

CHAPTER 3

Features of lava lake filling and draining and their implications for eruption

dynamics

3.1 Introduction

Lava lakes are a common occurrence at basaltic volcanoes and are defined as either

'active' or 'inactive' (Swanson et al., 1973). Active lava lakes are located directly over

the source vent, so that lava enters and circulates within the lake. Active lava lake

convection may proceed for years-to-decades before supply ceases and lava drains. Such

activity has been observed at Kīlauea in U.S.A. (Puʻu ʻŌʻō: Heliker and Wright, 1991;

Halemaumau: Jaggar, 1947), Erta Ale in Ethopia (Harris et al., 2005), Nyiragongo in The

Democratic Republic of the Congo (Tazieff, 1984), and Villarrica in Chile (Witter et al.,

2004). Inactive lava lakes are located adjacent to, or down flow from, the source vent

and typically form as a result of lava flowing into a previously formed depression. These

have been observed in various pit craters on Kīlauea, such as ʻAlae (Swanson et al.,

1979) and Makaopuhi (Wright and Kinoshita, 1968), as well as on Masaya, Nicaragua

(Harris, 2008). In inactive lava lakes, most of the crater-trapped lava does not drain back

down the feeder vent when supply ceases, but remains within the confining pit to stagnate

and cool in place (Peck et al., 1966; Wright and Okamura, 1977).

Throughout the life time of a lava lake, processes of lava movement within the

lake vary in time and space. Convection and influxes of new magma circulate the lava

and transfer heat (Harris et al., 2005); consequent surface motion results in formation,

growth, and destruction of crustal plates (Duffield, 1972). In active lava lakes, the final

period of lava drainage largely destroys any record of the earlier history of the lake. Since the lava has nowhere to drain in inactive lakes, freezing preserves some of the features associated with lake processes. In this paper, we examine the preserved features of a lava lake that was sometimes active and sometimes inactive.

The 37-day-long lava fountaining eruption in 1959 at Kīlauea Iki, Kīlauea, Hawaiʻi (Figure 3.1) resulted in the formation, repeated filling, and partial drainage of a lava lake within an existing pit crater adjacent to the principal vent. Throughout the eruption, the lake level rose and fell during waxing and waning of fountaining at the vent, nearly half way up the ~200-m-high wall of the crater. While lake level was below the vent, the lake was inactive. Lava fountains from the vent ponded lava in the crater, causing lake level to rise. In each fountaining episode, lake level reached the height of the vent, and the geometry became that of a classic active lava lake. Lake level often rose above the level of the vent, and fountaining burst through the lake. When fountaining ended, lava drained from the lake back into the vent, which acted much like the overflow drain on a bath tub, until lake level reached the vent level, when drainage ceased and the lake was once again technically inactive.

At Kīlauea Iki, we found preserved features associated with lake filling, drainage, and stagnation and link them to the lake dynamics that constructed them. In particular, we are able to interpret the timing of processes in the last episodes of the eruption that contribute to a greater understanding of generic lava lake processes.
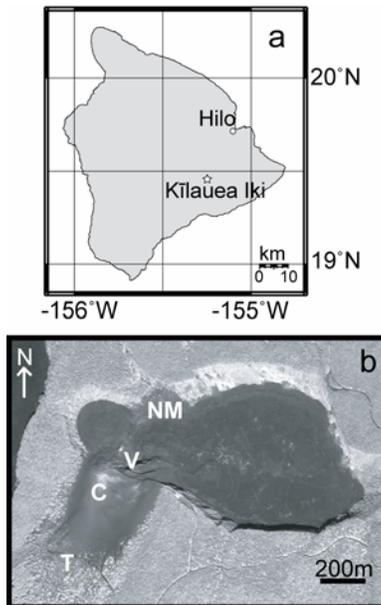
Figure 3.1 Location map of the island of Hawai'i and Kīlauea Iki lava lake.
(**a**) Island of Hawai'i with star marking location of Kīlauea Iki and (**b**) IKONOS image of Kīlauea Iki lava lake with north margin (NM), vent (V), cone (C) and tephra (T) highlighted.

3.2 Kīlauea Iki 1959

During the November – December 1959 eruption of Kīlauea, a ~ 46 x 10^6 m^3 lava lake

(Figure 3.1) was formed in the Kīlauea Iki pit crater (Richter et al., 1970). The eruption

comprised 17 episodes over 37 days and produced the highest recorded lava fountaining

events in Hawai'i (Richter et al., 1970). The vent was 110 m above southwestern floor of

the crater, and some of the ejecta from the fountains entered the crater, forming the 110-

m-deep lava lake, which eventually overtopped and interacted with the vent (Richter et

al., 1970). Each episode can be divided into two stages: an early stage of fountaining and

lake filling (Figure 3.2a) and a late stage of drainage and lake lowering (Figure 3.2b).

After fountaining stopped, excess lava drained from the lake into the vent. Only the

upper portion of the lake (that which overtopped the vent) could drain; the residual lava

remained trapped, cooling *in situ*, until the onset of the next episode. This two-fold cycle

31

of fountaining and lake filling, then draining and lake lowering, repeated through the 17

episodes of the eruption (Figure 3.3a). When the eruption ceased, the remaining lava

cooled as a stagnant body, preserving intact surface features of the lake.
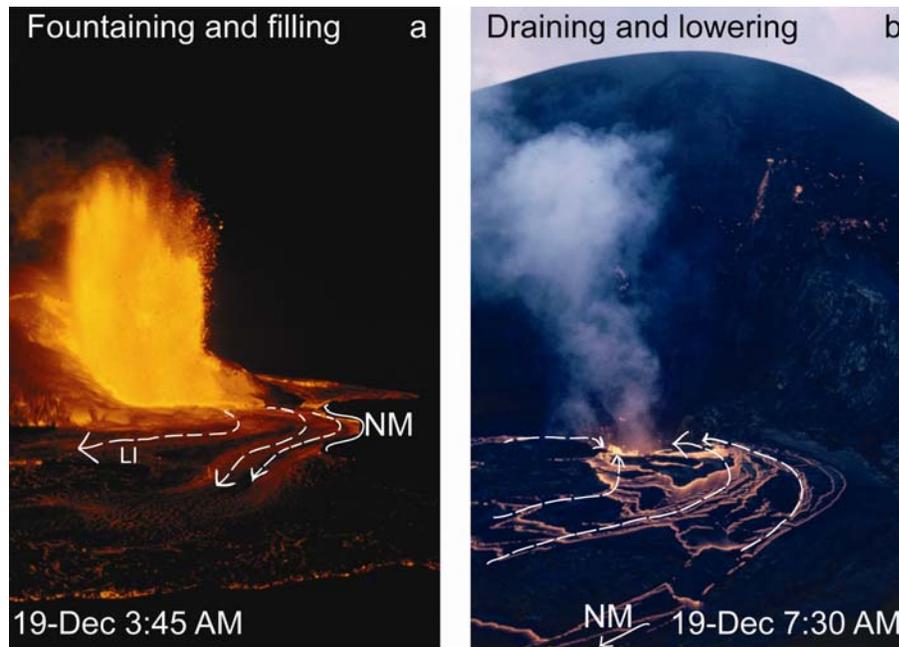
Figure 3.2 Photographs of lava lake fountaining/filling and draining.
Photographs taken by Jerry Eaton during Kīlauea Iki eruption with dashed arrows
indicating direction of lava flow in lake. (**a**): Episode 16 fountaining and lake filling
stage, showing clear flow pathway along north margin (NM, solid white line along trace
of wall). LI indicates location of partially-submerged lava island; note flow pathways
diverted around island. (**b**): Episode 16 draining stage approximately 1 hour after end of
fountaining, when 60-m-wide channel within lake fed backflow down vent. NM with
arrow points toward north margin, slightly out of view in photograph around edge of
channel flow. Photographs courtesy of Hawaiian Volcano Observatory (HVO) library.

The final Kīlauea Iki lava lake is approximately 1.5 × 0.8 km in diameter and

contains features formed through the life of the lava lake. Some key features and their

inferred mechanism of formation were described by Richter et al. (1970). These are

summarized in Table 3.1 and are used throughout this paper.

Table 3.1. Summary of Kīlauea Iki lava lake features.

Feature or Term	Definition from Richter et al. (1970)
Pāhoehoe ooze up	Lava that filled the gap (oozed up into the crack opening) between the surface crust and the crater wall as floating lake crust pulled away from the walls.
Lava islands (Figure 3.2)	Portions of intact cone material that slid into the lake, forming islands. These were sometimes overtopped during fountaining and lake filling, then re-exposed as the lake drained.
Surface waves	Agitation of lake at the fountain base created surface disturbances (waves) on the lake that traveled radially outward and lapped onto the north margin shore.
Crustal foundering	Crustal plates sank into the lake in response to surface flow of new lava breakouts thereby reworking the entire surface every few hours (Stovall et al., 2008).
Backflow/drainback	Draining of the lake into the vent sometimes occurred during the late stages of fountaining, and always after fountaining ceased; a clockwise whirlpool sometimes formed above the draining vent.
Subcrustal draining	Lake drainage that occurred without disturbing newly formed surface crust and resulted in lowered lake level without visible streams of lava pouring into the vent.

3.2.1 Episodes 16 and 17

The features preserved on the surface of the Kīlauea Iki lava lake are remnants of the

final two episodes (16 and 17) of the 1959 eruption. Episode 16 started 35 hours after the

cessation of fountaining during episode 15 (Figure 3.3a). Episode 16's fountaining stage

lasted 3 hours 36 minutes and, although shorter in duration and producing fountains

lower than those of episode 15, it fed a lake that reached a level 2 m higher (123 m deep,

Figure 3.3a). This was likely due to an increased flux during episode 16 fountaining.

After the fountain died, drainback of lava into the vent began immediately, and an hour

later the backflow channel stretched 60 m across the lake surface as a lava river (Figure

33

3.2b). Richter et al. (1970) noted that the river was "…carrying great blocks of darkened crust that were torn apart as they approached and plunged into the open vent." Throughout the drainage, wholesale renewal of the lake surface occurred via crustal foundering, which sometimes produced secondary lava fountains due to the release of trapped gases within the sinking, cooled crust (Richter et al. 1970).

There is some uncertainty as to when episode 17 began, or indeed if it was truly a separate episode. Noticeable fountaining resumed 14 hours and 29 minutes after the end of episode 16 fountaining (Richter et al., 1970). By then, the lava lake had drained approximately 6 m from the high stand of episode 16 and was 116 m deep (Figure 3.3a); later work by Helz (1993) and Barth et al. (1994) indicate the final lake depth may have been closer to 135m. Episode 17 fountaining never reached more than ~30 m in height and lasted for ~11 hours and 15 minutes. During this time backflow continued but at a markedly reduced rate, resulting in relatively slow lake lowering (Figure 3.3). Toward the end of this final fountaining, lava flowed from the vent and covered a ~4000 m^2 area of the lake surface (Richter et al., 1970). The features we describe are those of episodes 16 and 17 except where erosion of the surface allows observation of products from earlier episodes.
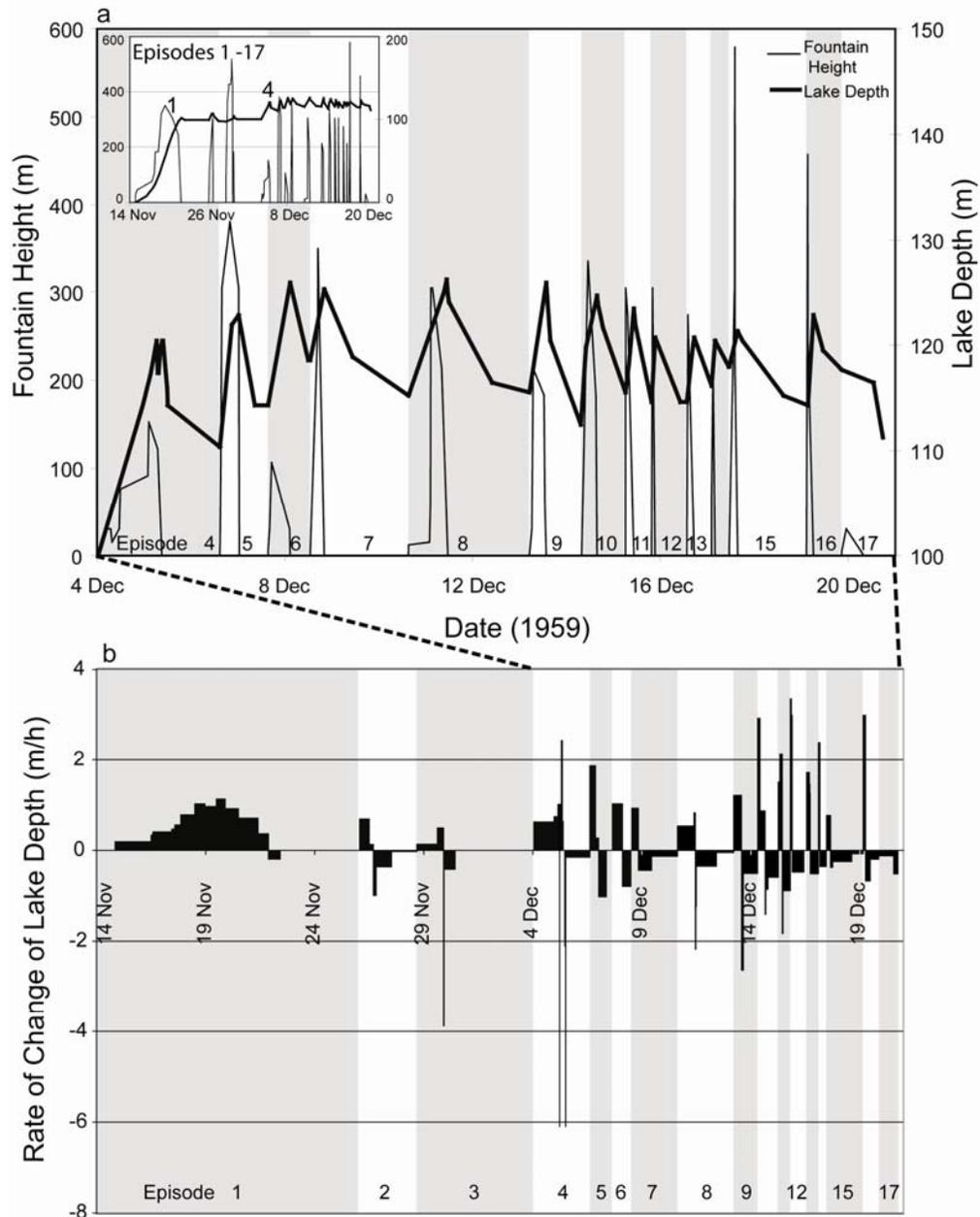
Figure 3.3 Kīlauea Iki fountain height and lava lake record by episode.

Kīlauea Iki eruption record; shading stripes alternate for each episode. (**a**): Lake depth versus fountain height with episodes 4 – 17 highlighted. Inset for episodes 1-17 indicates ~20-m-deeper lake first reached in episode 4 due to upward migration of vent. (**b**): Rates of filling and lake deepening (positive numbers) and draining and lake lowering (negative numbers) for all 17 episodes of eruption. Where graph portrays multiple tiered drainage, rates are always fastest immediately following end of fountaining and filling stage. Data from Richter et al. (1970) and contemporary field notebooks (HVO library).

35

3.2.2 Rates of Filling and Drainage

Rates of filling and drainage varied for each eruptive episode (Figure 3.3b). Rates of filling were lowest during the earlier, longer fountaining stages and highest during the very high, but shorter, fountaining stages, such as episodes 15 and 16, which occurred toward the end of the eruption. For example, the maximum discharge during the first episode of the eruption was ~ 3.8 x 10^5 m^3/h, but during high fountaining of episode 16 the discharge reached ~ 1.2 x 10^6 m^3/h (Richter et al., 1970). During episode 3, a dramatic change in the rate of drainback was noticed. Immediately following fountaining, flow back into the vent occurred at a rapid rate but then slowed "when the seemingly bottomless conduit filled" (Richter et al., 1970). Lava continued to drain but "at a much reduced rate and without the turbulence that accompanied the plunging lava fall into the open conduit" (Richter et al., 1970). Similar to filling, drainage rates were lower following the longer, early fountaining stages, except for short-lived rapid drainage just after fountaining in episodes 3 and 4. Rapid drainage during the more closely spaced, later eruptive episodes continued for a longer time than during the earlier episodes (Figure 3.3b).

Episode 4 was the second longest (behind the week-long episode 1) and most anomalous in terms of filling and draining history. Fountaining continued for 32.5 hours and produced voluminous lava outpouring that filled the lake to a new high stand (Figure 3.3a) due to upward vent migration (Richter et al., 1970). During the fountaining stage of this episode, there was rapid concurrent drainage of the lake at a rate ~ 4 x 10^6 m^3/h (~ 1100 m^3/s). After fountaining ended, the lake remained level, and backflow did not

36

begin for ~20 minutes; it then quickly reached the same rapid rate achieved during the previous fountaining (Figure 3.3b).

3.3 Lake Features

The north margin wall (Figure 3.4) and western faces of the lava islands (Figure 3.2) provide a record of the filling and draining events by virtue of features frozen *in situ* (Figure 3.4). Two main sets of features are observed, vertical rinds and lava shelves, which form a repeated theme at these localities. Vertical rinds are layers of solidified lava plastered on the walls of the north margin and islands. At some locations, three such observable vertical rinds are superimposed (Figure 3.5a). A set of horizontal lava shelves is attached to the lake-facing side of each vertical rind (Figure 3.4). Study sites for the vertical rinds were chosen based on the best exposures where the rind cross-sections are visible because of erosion and removal of the lakeward layers. Rinds are exposed at six locations along the north margin, two of which are labeled as VR in figure 3.4. Three study sites for lava shelves were selected at ~30-m intervals along the ~100-m-wide, east-west trace of the north margin wall (Strat. 1, 2, and 3, Figure 3.4).

3.3.1 Vertical Rinds

Vertical rinds of lava form onion-skin-like layers against vertical faces of the islands and on the north margin wall tens of centimeters thick (Figure 3.5). Cross sections of multiple rinds are exposed where the outer layers have broken and toppled onto the lake surface forming talus piles (Figure 3.5a). Three distinct vertical rind layers (A, B, and C) are preserved along the north margin wall; we correlate them with episodes 14, 15 and 16 (Figure 3.5a). Only two rinds are apparent on the islands. Thickness measurements were

37

made of each exposed rind at the six study sites along the north margin wall. In general, the vertical profile of each rind thickens downward to a maximum, below which it thins sharply (Figure 3.5b).
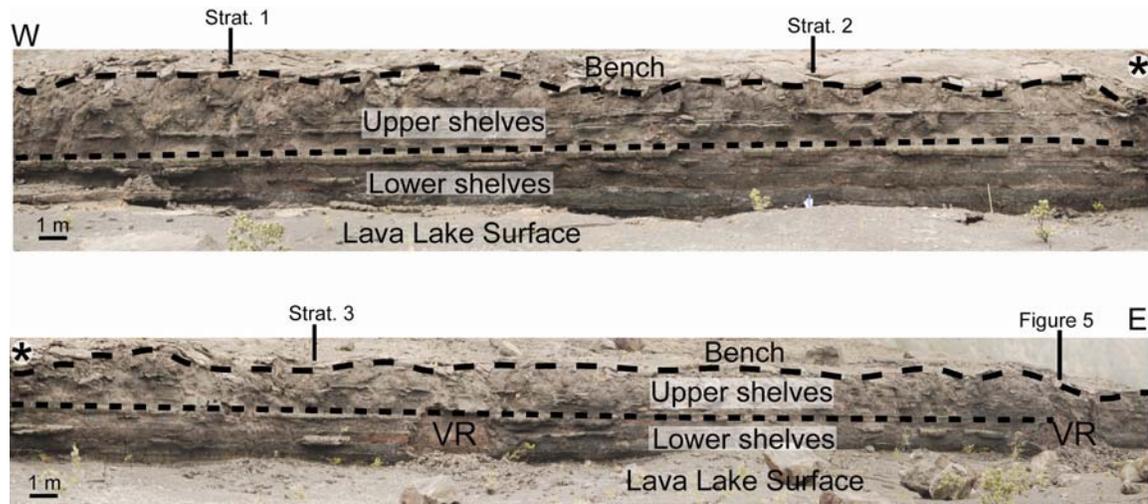
Figure 3.4 Panoramic photographs of the north margin wall.

North margin wall of Kīlauea Iki lava lake from west to east; asterisks connect right side of the upper photograph with left side of the lower photograph. Upper long-dashed line demarcates upper bench from top of vertical wall, and lower short-dashed line indicates transition along the wall from upper to lower shelves. Study locations are highlighted as: 'VR', locations where wall has fallen away, exposing vertical rinds; 'Strat. 1', 'Strat. 2', and 'Strat. 3', depicted in Figure 3.8; and 'Figure 3.5', the location for Figure 3.5 along the north margin.

Each vertical rind has several texturally distinct sub-layers. The youngest rind C, closest to the lake, is the best exposed and is referred to as the "wall" of the north margin and islands (Figure 3.5a). The typical lake-facing surface of C has millimeters to centimeters of relief; due to the presence of angular spines, rounded lava blebs, and linear glassy ledges (Figure 3.6). The blebs point upward (Figure 3.6b) and resemble 'shark's tooth projections' defined by Nichols (1939) as points or ridges of lava that project out at high angles from the wall rock. Blebs are commonly rotated and can be matched back to a broken, oxidized underlying surface (isolated shark's tooth projection, Figure 3.6c).

38

Locally, the lake-facing surface of the wall is marked by grooved lava (Nichols 1938) and (or) coated with lava drips.
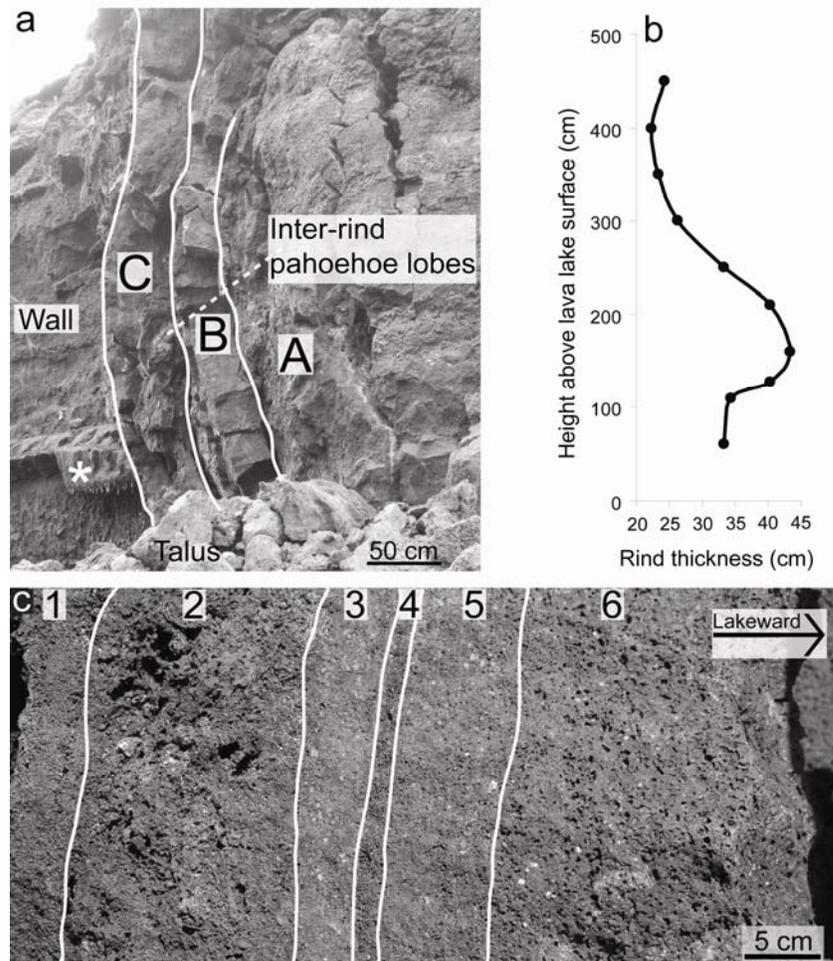
Figure 3.5 Vertical rind photographs and thickness measurements.

Vertical rinds exposed along north margin wall at location denoted in figure 3.4. (**a**): Rinds B and C have partly peeled away from wall, exposing surface of rind A. Lakeside surface of rind C is labeled as 'wall'. Asterisk highlights lower zoned shelf (Figure 3.10). Dashed line points to inter-rind pāhoehoe lobes. (**b**): Rind C thickness increases from top toward the bottom of wall until a height of approximately 150 cm above the lake surface is reached; below that, the rind thins. (**c**): Cross section of vertical rind C with 6 textural zones highlighted; zone 6 is the youngest, and zone 1 the oldest.
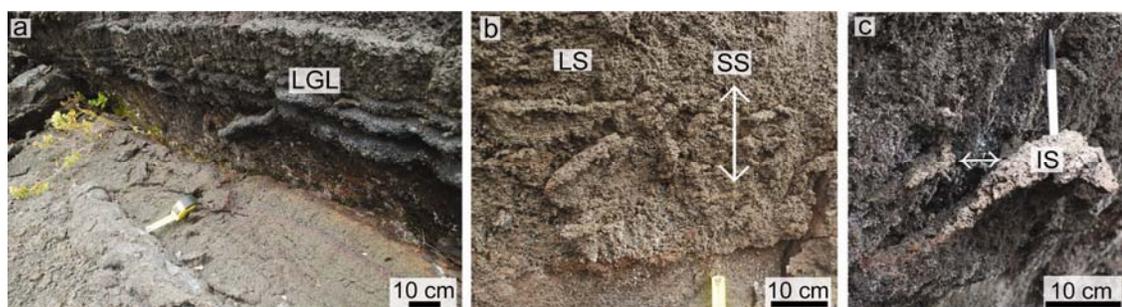
Figure 3.6 Photographs of peel-away textures on the north margin wall.

Peel-away textures found at different heights along the north-margin wall. Lower wall section (**a**) has linear, sub-horizontal glassy ledges (LGL). Mid-wall section with (**b**) linear (LS), stacked (SS), and (**c**) isolated (IS) shark's-tooth projections. Arrows indicate vertical region of SS in **b** and match-up between wall and IS in **c**.

In cross-section, each rind has a distinct zonation defined by differing vesiculation textures. Rind C contains 6 zones (1–6, Figure 3.5c) with gradational contacts and are described in detail in Table 3.2.

Table 3.2. The 6 zones of vertical rind C.

Zone	Thickness	Vesicularity[a]	Vesicle shape	Vesicle Diameter	Thickness Between Bubbles
1[b]	3.0 cm	High to very high	Round and coalesced	mm to cm	<1 mm
2[c]	7.5 cm	Moderate to high	Highly coalesced	mm to cm	≤1 mm
3	3.0 cm	Low	Round	1-3 mm	5-7 mm
4	1.5 cm	Very high	Round	1-3 mm	<1 mm
5	7.5 cm	Moderate	Round	1-4 mm	1-4 mm
6	11.0 cm	High	Small = round Large = coalesced	mm to cm	~5 mm

[a]Vesicularity is qualitative and based on field observations of relative abundance of vesicles to lava within each zone.
[b]At the contact with zone 2, zone 1 contains a 1-cm-thick coalesced bubble layer. Inward, a highly & finely vesicular section with mm-scale rounded bubbles coalesces inward. Toward the contact with rind B, the bubbles flatten into a 1-cm section that passes into a thin glassy crust (quenched rind) with stretched, vertically oriented blebs on the surface.
[c]A region of gas pockets near the center of zone 2 is defined by trains of bubble coalescence up to 8 cm long. The interior of the gas-pocket regions has a smooth quenched surface, and individual elongate blebs of lava can be defined.

The contacts between each vertical rind are marked locally by the presence of 5–20-cm-long lobes and toes of solidified lava with highly oxidized surfaces. These fill void spaces between vertical rinds and represent pāhoehoe-like extrusion and inflation of lava into the spaces.

Some vertical rinds also enclose shelves of lava attached to the lake-facing surface of the next-older rind. Rind B was plastered onto a shelf on the face of rind A, causing the wall-side contact of B to curve around the underlying protrusion (Figure 3.7). However, the lakeward margin of rind B shows no expression of the underlying shelf.
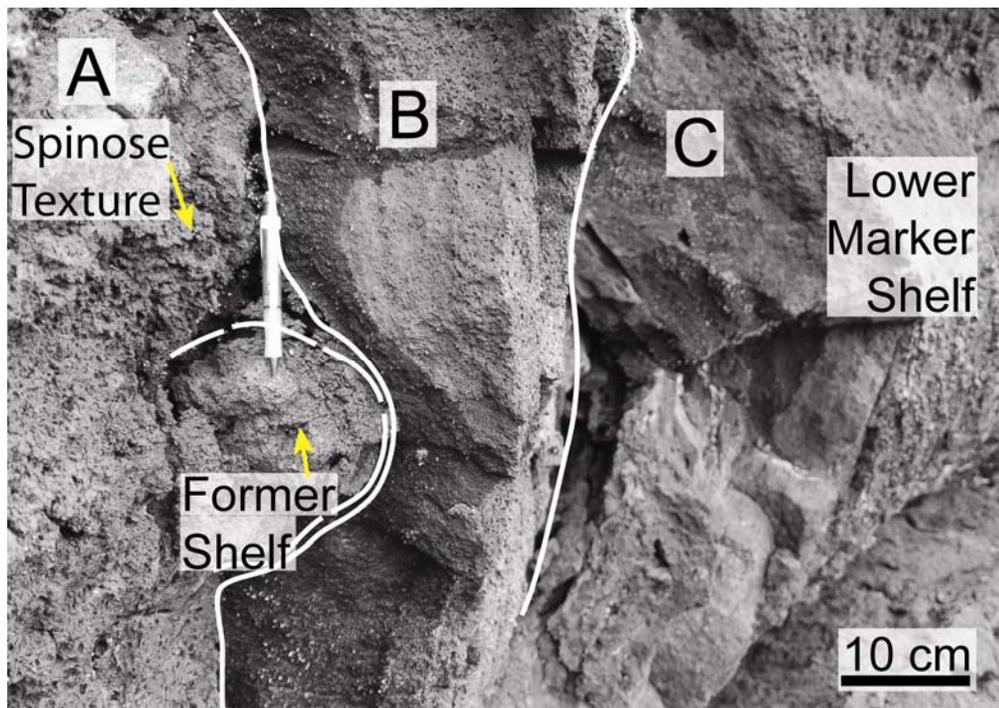
Figure 3.7 Photographs of three sequential vertical rind layers.
Vertical rinds A, B, and C exposed by collapse of north margin wall. Lakeward face of rind A has spinose texture and former shelf (dashed outline) that were both covered, but not remelted, during development of rind B. Rind B does not bulge in region of former shelf. Lower marker shelf is present on lakeward face of rind C. Arrows point to spinose texture and former shelf.

3.3.2 Lava Shelves

Lava shelves are attached to the lake-facing side of the vertical rinds (Figure 3.8). They occur on the walls of the islands and the north margin and can be grouped into two categories. The shelves on the top half of the wall are typically thinner, more closely spaced and laterally discontinuous compared to those on the lower half. The north margin wall exposes the most complete set of shelves found within the lava lake (Figure 3.4); the description below is based on the set of shelves attached to rind C.

3.3.2.1 Upper shelves

The shelves attached to the upper half of the wall have similar textures and lack any characteristics to distinguish one from the other (Figure 3.8a). They are 4-10 cm thick and range in lateral extent up to several meters. This lack of lateral continuity within individual shelves, with no evidence of longer, once-continuous traces, is a primary characteristic. The upper surface of each shelf is typically glassy and has stretched bubble lineations. Below the upper 4-mm-thick glassy surface, the shelves have a high vesicularity (~80%) with large rounded bubbles ranging in diameter from 2 mm to 1 cm. Bubble walls are <1 mm thick, except where 2–5-mm olivine crystals are present, resulting in greater separation between bubbles. A band of oxidation is found within the middle portion of a few shelves. The bottom surface has up to 2-cm-wide amoeboid-shaped bubbles and a 'spinose' texture of mm- to cm-scale spike-like protrusions that stand with relief from the surface.

42
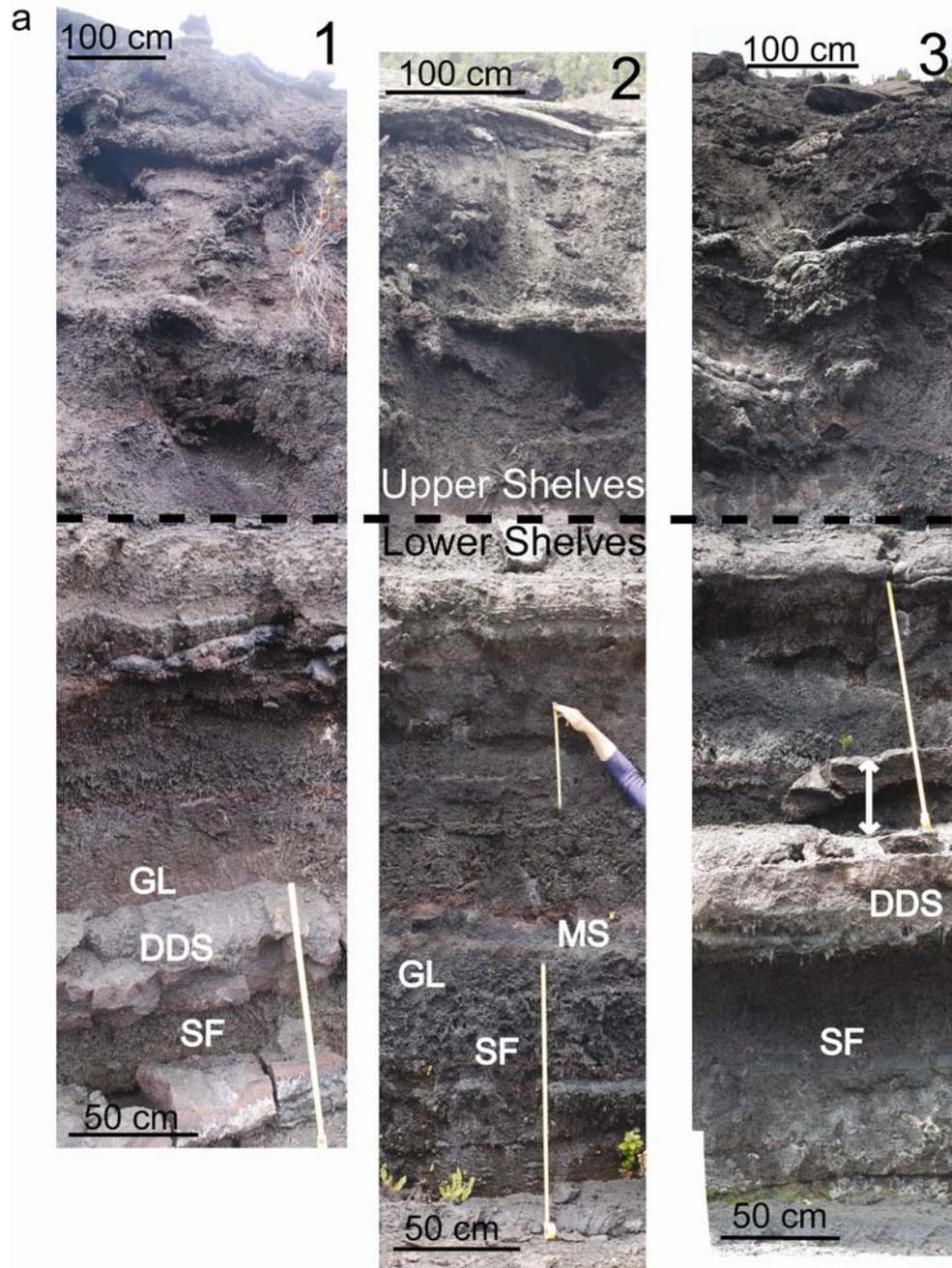
Figure 3.8 Photographs and cartoons of three north margin wall stratigraphic sections.
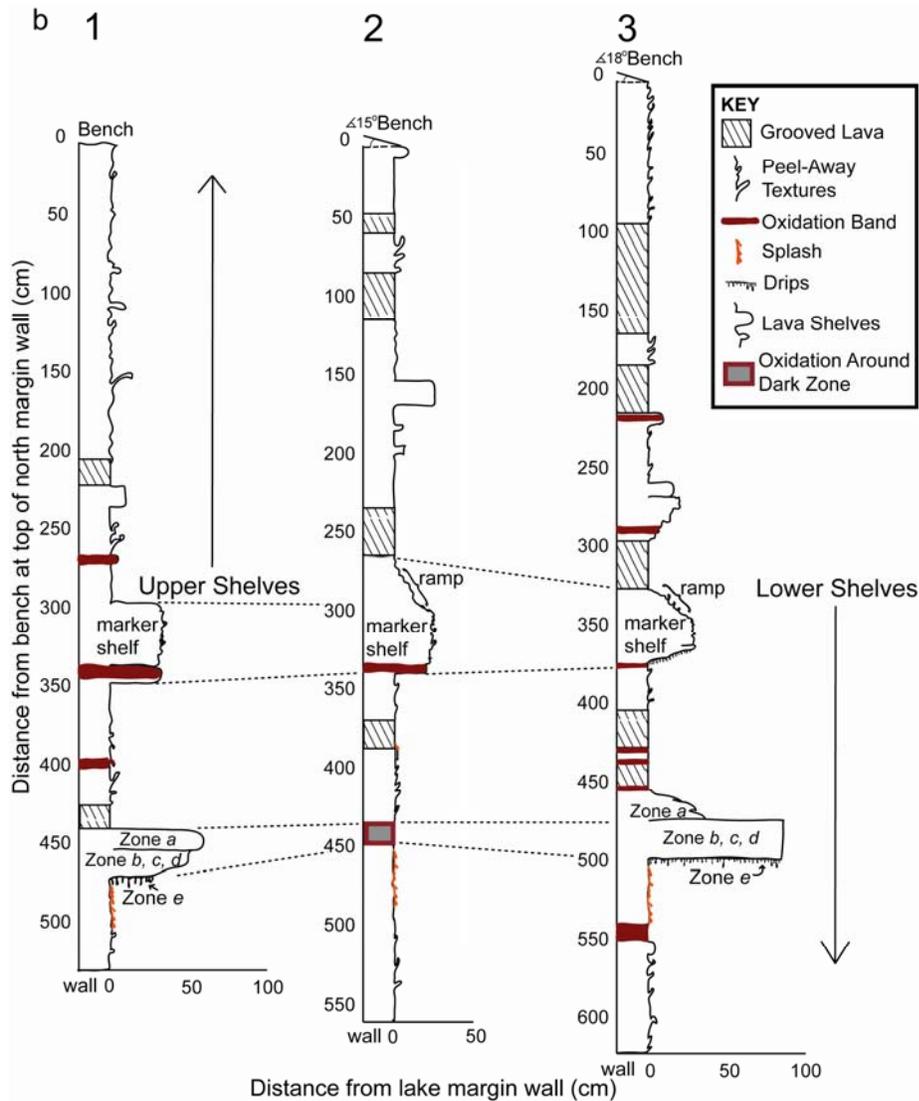
Figure 3.8 Photographs and cartoons of three north margin wall stratigraphic sections.

Stratigraphic sections from three locations along north margin wall (Figure 3.4). (**a**): Stitched photographs of each stratigraphic section taken from surface of lake. Angling and stitching of images creates a foreshortened effect, so that top and bottom of each section have different approximate scales. Upper and lower shelves (separated by dashed line) are defined by change in shelf morphology from scattered, discontinuous, non-uniform appearance at top of wall to continuous, well developed appearance at bottom. 'Marker shelf' lies directly under dashed line. Grooved lava (GL), two down-dropped shelves (DDS, with arrow connecting matching pieces in Strat. 3), location of missing shelf (MS in Strat. 2), and splash features (SF) are indicated. (**b**): Illustration of each section; 'marker shelf' defines break between upper and lower shelves. 'Ramp', angling to leading edge of 'marker shelf', is apparent in sections 2 and 3, and the two features are typically coupled along the trace of north margin wall. The angle of the bench in relation to horizontal is denoted in sections 2 and 3.

44

3.3.2.2 Lower shelves

There are two distinct, laterally continuous shelves attached to the lower half of the north margin wall with markedly different surficial and internal textures. We refer to the upper of these two shelves as the 'marker shelf' (Figures 3.7, 3.8b, 3.9) because of its prominence; it is a reference for assessing changes in lake dynamics over an extended area. An angled 'ramp' of spinose and blebby solidified lava slopes out from the wall down to the surface of the marker shelf at most locations along the north margin wall (Figures 3.8b, 3.9). The marker shelf is bulbous in cross section, 40–45 cm thick, and laterally continuous over the ~100-m length of the northern margin wall (Figure 3.4). In cross section, it is moderately vesicular, with ~50% bubbles. On a cut surface, walls between bubbles are 1–4 mm thick, except where olivine crystals increase the spacing distance. The upper 30–35 cm of the upper lake-facing surface are highly spinose and contain 1–4 mm-wide amoeboid bubbles with an aspect ratio of 3:1. The irregular, spiny texture is defined by lava, between bubbles, that was pulled or stretched to form the spines. A striking surface feature of the marker shelf is a laterally continuous, 5-cm-thick zone in the middle of the shelf, consisting of three layers of 3-mm-thick flattened bubble lineations. Another striking surface feature is the presence of 3 – 8 cm-long blebs of lava that protrude from the shelf with a slight rotational fabric (Figure 3.9). These rotated blebs are similar to those on the walls of the north margin and islands. The bottom part of the marker shelf is a 7-cm-thick, less spinose zone with a smoother surface and no flattened bubble lineations, though it does contain a few rotated blebs (Figure 3.9).
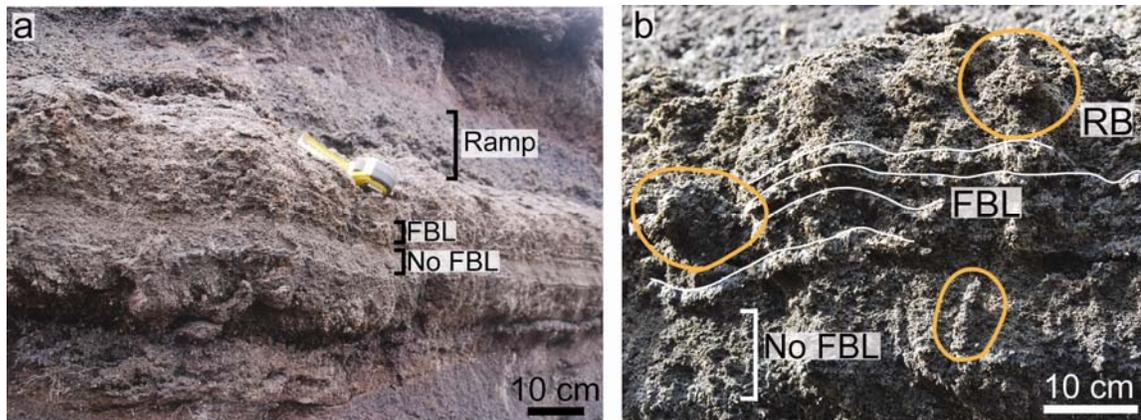
Figure 3.9 Photographs of marker shelves along north margin wall.

Two views of north margin wall 'marker shelf'. In (**a**), ramp angles lakeward from wall (Figure 3.8b) flattened bubble lineations (FBL) are in central portion of shelf, with zone below lacking lineations (No FBL). In closer view (**b**), rotated blebs (RB) are circled, FBL are traced with white line, and zone of no FBL is bracketed.

  The lower shelf (below the marker shelf) is not as laterally continuous. Where it is missing from the wall, an oxidized broken surface marks its former location on the wall (Figure 3.8b). The texture of this shelf can be observed in cross section in two planes: (1) a face parallel to the lake margin and (2) broken faces at a 90-degree angle from (1) and perpendicular to the wall. The broken face has similar textures throughout. It is moderately to highly vesicular (~60 %), with isolated 3–4-mm-diameter bubbles ranging from complex amoeboid shapes to ellipsoids with 1–2 % of larger coalesced bubbles, 2–3 cm in diameter. Vesicularity changes very little vertically except in the lower 5–6 cm, where it is slightly less than above. Bubbles in the upper 3–4 cm are a little smaller and somewhat elongate, with 2:1 or 3:1 aspect ratios.
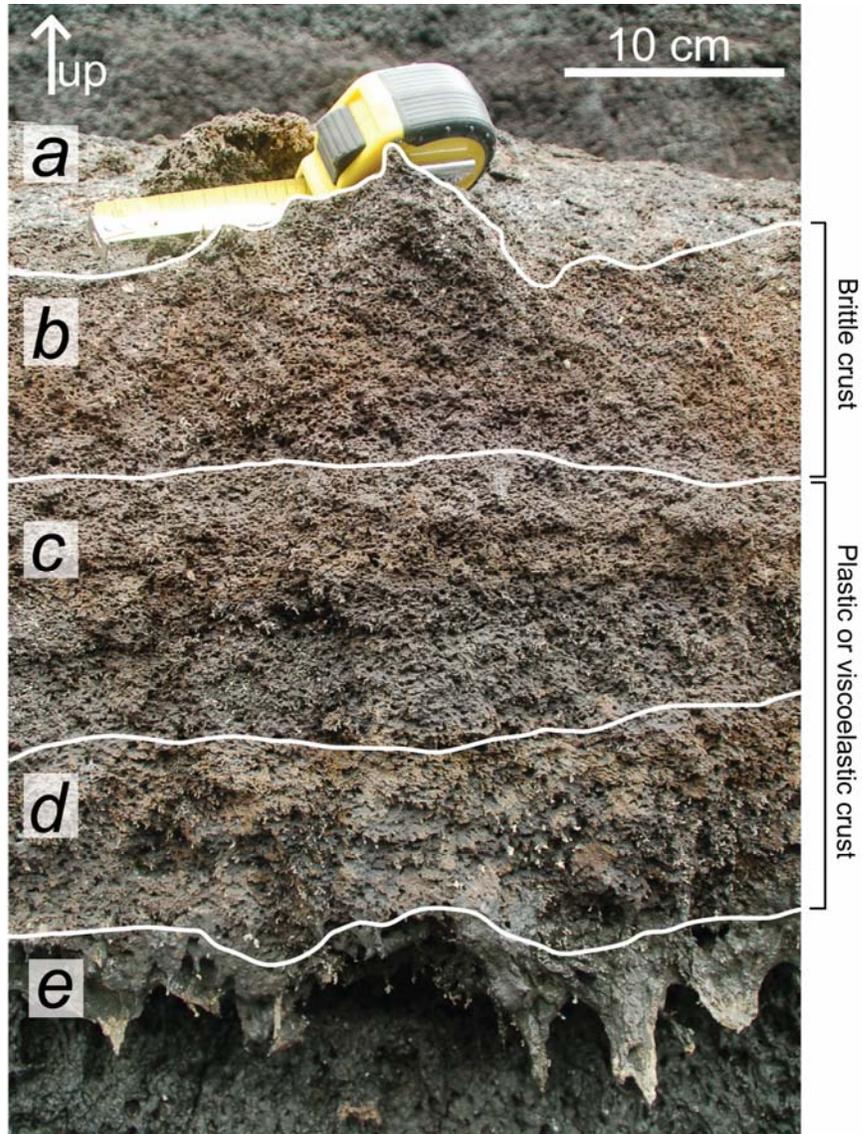
Figure 3.10 Photograph of lower shelf and zones.

Lower shelf with five defined, vertically-stacked zones. Zone *a* is superimposed on top of zones *b* – *d* and is poorly depicted here. Texture of zone *b* is typical of brittle crust failure, and textures of zones *c* and d are typical of viscoelastic crust failure. Zone *e* consists of stalactite-type drops on the bottom side of the shelf.

The lake-facing surface of the lower shelf has 5 distinct vertically stacked zones

(*a* – *e*, Figures 3.8b, 3.10) that exhibit varying textures. They are described from the

vertical lake-side face (Figure 3.10).

1. The uppermost zone is ~20 cm thick and projects 30 - 60 cm from the wall toward the lake (zone *a*, Figures 3.8b, 3.10). It is attached to the upper surface of zones *b*–*d*. Its surface is glassy and contains stretched bubbles forming a distinct arcuate fabric on the surface.

2. Zone *b* is ~9 cm thick and has mm-scale amoeboid bubbles with a 2:1 aspect ratio. It lacks spinose surface texture, and its face is smooth relative to the two zones below.

3. Zone *c* is ~11 cm thick, with an irregular (bumpy) spinose surface texture. The bubbles are mm-scale and multiple; distinct clusters of bubbles and surrounding rock combine to form spines ranging from a few millimeters to 1 cm in length.

4. Zone *d* is ~8 cm thick. Its bubbles are slightly larger than those of zone 3 but still <1 cm. The bubble-wall texture is stretched into spike-like filaments oriented downward creating scattered cylinder-shaped or tube-like bubbles.

5. Zone *e* is made of stalactite or drip-like features 2–8 cm long. The outer surface of these features is glassy and lacks distinct bubbles.

3.4 Interpretation

Each set of rinds and shelves correlates with a filling-draining event linked to a specific eruption episode. Each rind probably formed during cooling and accumulation of lava accompanying steady lake filling during each fountaining episode. Each shelf formed on the lakeward surface of a rind probably during a period of non-steady drainage following the close of fountaining. Lava entered and drained the lake via the vent, directly opposite the north margin wall (Figures 3.1, 3.2). Inspection of contemporary photos shows that, as lake level rose and fell, lava flowed along this wall; the north margin acted as a bank

much like the levees of a lava channel. Additionally, waves on the lake surface,

originating from surges of activity in the vent, often broke onto and splashed against the

north margin (Richter et al., 1970). Other lava splashes occurred when shelves failed and

fell into the lake (Stovall et al., 2008). The rinds and shelves record a pattern of changing

dynamics within the lava lake during fountaining commencement, waxing, waning and

absence.

3.4.1 Vertical Rinds
We associate vertical rinds with episodes of lake filling. Rinds began forming early in

every episode during a period of low fountaining (Richter et al., 1970), which poured

lava into the crater. As the lake deepened, the near-vertical faces of the north margin and

islands, which had been exposed to air during draining following the previous

fountaining stage, were progressively submerged beneath the rising lake (Figure 3.2a).

Due to the temperature difference between the hot lake lava and cooler walls, a cooling

front, originating at the wall, progressed outward into the lake. This resulted in

quenching and accumulation of partly solidified lake lava against the faces. As lake level

rose, progressively higher portions of the wall were submerged. Therefore, as soon as the

lake reached a given level on the wall, cooling and rind accumulation commenced,

continuing until this level was re-exposed during lake drainage. Upon, or immediately

before, cessation of fountaining, lava drained from the lake into the vent (Figure 3.2b),

thereby lowering lake level and progressively re-exposing the walls. As lake level

dropped, a layer of solidified lava remained as a wall-coating rind.

The 1065° C isotherm marked the crust-melt boundary within Kīlauea Iki lava lake during initial drillings in 1960, 1961, and 1962 (Ault et al., 1962; Richter and Moore, 1966), when the crust was relatively thin (Helz and Thornber, 1987). This isotherm therefore indicates the boundary temperature between fluid lava capable of draining from an exposed wall and viscous-to-solid lava that would adhere to the lake wall. During draining and exposure of the vertical rinds, a viscous boundary layer was exposed and behaved plastically, with drainage plucking away viscous blebs, thereby forming a spinose texture with shark's-tooth-like projections (Nichols, 1939) on the lake-side face of the vertical rind. The previously submerged walls, exposed to air, then cooled more rapidly by radiation and convection until the onset of the next fountaining and lake-filling episode.

The vertical rind bordering the lake (C) corresponds to the final episode(s), 16 and possibly 17. By extension, rind B corresponds to episode 15 and A to 14. The thickness of each rind reflects the amount of time that lake level remained at a certain height. The rate of rind growth and thickening due to cooling of lake lava would have correlated with the square root of time (Rupke and Matthias, 2004). Simultaneously, heating of the wall rock would have decreased the thermal gradient between the lake lava and wall rock, similar to the conduction of heat from a dike into its host rock (Lovering, 1935; Turcotte and Schubert, 2001). Eventually, both the lake and the wall would have become increasingly stable thermally, when cooling and growth occurred at reduced rates. Therefore, thickening would have slowed with time as the thermal gradient developed.

However, the typical length scale of a chilled layer forming at the lake margin can be calculated following, for example, Turcotte and Schubert (2001).

Above the marker shelf (Figures 3.7, 3.8b, 3.9) rind C is ~20 cm thick, and would have grown during the period that the episode 16 lake was at or higher than this level. This time would have been no longer than the time difference between the onset of episode 16 filling and the end of episode 16 drainback (onset of episode 17 fountaining). This gives a maximum formation time of 18 hours. Thus, the rind attained its 20 cm thickness in somewhere less than 18 hours. This is consistent with simple scaling of the thermal diffusion length scale and timescale, where the rind thickness (L) should scale to time (t) and thermal diffusivity (k) in $t = L^2/k$. Thermal diffusivity is obtained from lava thermal conductivity (κ), specific heat capacity (c_p) and density (ρ) in $k = \kappa / c_p \rho$. To solve this we first use the typical thermal conductivity obtained for vesicular Kīlauea Iki lava by Robertson and Peck (1974) of 1.4 W/m K. We next follow Keszthelyi (1994) to calculate a specific heat capacity, for lava at a boundary temperature of 530 °C, equaling 1072 J/kg K. Using these values with the mean bulk density for Kīlauea Iki's lake crust (1450 kg/m^3, Stovall et al., 2008), we obtain a thermal diffusivity of 9.46 x 10^{-7} m^2/s. This compares with that obtained, using a typical vesicularity of 49 %, in the method of Keszthelyi (1994), i.e., 1.01 x 10^{-6} m^2/s. For L of 20 cm (0.2 m), these diffusivity values give a time scale of 11-12 hours for rind formation. Theoretically, the thickness of a solidification layer (y), forming on or around a lava lake, will increase with $2\lambda\sqrt{kt}$, with λ being a dimensionless scaling value calculated, by Turcotte and Schubert (2001) for Kīlauea Iki's lava lake, to be 0.421. This predicts (for k of 9.46×10^{-7} and 1.01×10^{-6}

m^2/s) a 0.2 m thick rind forming in 16-17 hours. Thus, theoretical formation of the 20 cm thick rind is entirely possible during the 18 hours formation time available.

The increased submergence time within the lake led to the lower part of the wall developing thicker rinds than the upper part. However, the lowermost part of the rind thins downward toward the present surface of the lava lake (Figure 3.5b). This occurred because heat supplied, from the portion of the lava lake remaining in place after drainback, conducted into the wall and created a thermal gradient within the wall characterized by decreasing temperature upward and away from the lake surface. This process would have been effective even during low stands at the end of lake drainback. The newly formed rinds were also exposed to an ambient temperature profile that would have declined with height above the hot lake surface. Thus the rinds, cooling radiatively to the atmosphere, would have cooled more slowly across the lower faces where (1) the ambient temperature would have been high due to heating of air by the lake surface, and (2) the wall itself would have remained warm due to radiative heating from the adjacent, undrained, lake lava. Cooling of material, and hence rind growth, at lower levels would therefore have been depressed.

New vertical rinds did not remelt, or adhere firmly to, the previously formed rind. The lake-facing surfaces of layers A and B preserve delicate features with no evidence of remelting of underlying layers. Grooved lava, splash regions, former shelves, and spinose textures of underlying layers (Figure 3.7) are intact even though these features were submerged within the lava lake during formation of later rinds. The underlying colder layers extracted heat from the already-crystallizing submerging lava, therefore

52

hastening its crystallization. Although heat was conducted from the lava lake into the wall it was insufficient to raise the temperature of the underlying rind to the melting point. Where shelves protrude from older rinds, the covering rind does not bulge outward around the former shelf (Figure 3.7). The older shelf is more vesicular and has lower bulk thermal heat capacity, so heats up faster and, therefore, imparts less cooling on the rind than surrounding parts of the wall. Conductive heat loss is reduced near the shelf, and both the cooling rate and rind thickening are reduced.

The six zones of rind C (Figure 3.5c) reflect progressive cooling and degassing of the lava lake. Solidification began with zone 1 at the wall contact and progressed lakeward to zone 6. Zone 1 quenched rapidly in contact with the relatively cool, previously formed rind as the rising lake contacted the wall. The irregular vesicularity and texture of zone 2 reflects accretion during lateral flow of lava along the wall, shown by the vertically stretched blebs we identified within the gas-pocketing region. These blebs, oriented in the direction of upward flow, were plastered against the wall as the lake level rose. Therefore this layer must have been accreted during flow along the wall during rapid filling of the lake. Zones 3 through 6 represent a typical cooling sequence resulting from outward growth of the rind into a relatively stable lake. These zones could have formed only when lake level was high enough to allow static cooling, without waves and splashing during filling.

The pāhoehoe textures between vertical rind layers may have formed during lake drainage as spaces opened between rinds. During lake draining, removal of lake-side support would have caused the newly formed rind to relax and perhaps slightly separate

from the upright layer, opening voids between rinds. Such voids could become pathways for pockets of viscous, still molten, lava exposed during void opening to remobilize and feed small pāhoehoe lobes into the cracks.

3.4.2 Lava Shelves

The lava shelves mark stable, though brief and temporary, lake stands during the drainback stage of each episode. During drainback, the lava level dropped at varying rates (Figure 3.3b) that sometimes resulted in pauses in subsidence of the lake surface. During these pauses, shelves formed either by (1) attachment of stable surface crust to the lake margin, which subsequently broke from the wall once drainage resumed, (2) accretion by flow or sloshing of lava along the lake margin during a brief pause or slowing of drainage or (3) by both processes. Shelves could either cool to greater thicknesses or accrete as thicker and wider benches when the rate of drainback slowed appreciably and lake level remained stable for an extended period.

All of the shelves visible on the outer surface of the north margin wall formed during episodes 16 and 17. Episode 17 was superimposed on the drainback stage of episode 16 and had only low-level fountaining (Figure 3.3a) that did not increase the depth of the lake (Richter et al. 1970). The upper half of the wall was exposed for the final time during the initial stage of drainback in episode 16 (Figure 3.2b), when lava poured rapidly down the vent as a 60-m-wide river (Richter et al., 1970). The markedly higher apparent vesicularity of the upper shelves as compared with those on the lower half of the wall reflects their early formation. They were formed by fresh, still vesiculating lava rather than by lava with a longer residence time in the lake that would

54

have lost more gas. Shelves on the lower half of the wall are thicker, less vesicular and laterally continuous, and formed during a slower and more staggered drainage period.

3.4.2.1 Upper Shelf Formation
The northern margin is only 200 m away from, and directly opposite, the vent; thus it was in an area of vigorous activity during drainage. Less than an hour into the drainage stage of episode 16, slabs of cooled crust were being pulled apart and flexed as they plunged into the vent (Richter et al., 1970). These individual slabs queued up to be pulled down the vent, sometimes lingering in contact with the wall. During early, rapid drainback, crust along the northern margin had the opportunity to cool against the wall for only a short time before the movement of material being drawn toward the vent tore the crust away. This resulted in thickening of only a few centimeters before most of the crust broke from the wall. Within this dynamic environment, crust remained attached in some places and broke away in others owing to lateral contrasts in relative rates of cooling, crust formation, and solidification against the wall. The unevenly distributed remnant shelves of the upper wall (upper shelves, Figure 3.8) are essentially the traces of crustal plates that lingered long enough along the north margin to attach securely to the wall.

3.4.2.2 Lower Shelf Formation
The shelves on the lower half of the wall (lower shelves, Figure 3.8) are thicker than the upper shelves and extend for ~100 m along the north margin (Figure 3.4). The marker shelf (Figures 3.7, 3.8b, 3.9) signals a change in the dynamic regime of lava behavior along the north margin. The spinose, blebby surface and lake-projecting structure of the marker shelf (Figure 3.9) indicate accretion at the lake edge during a stable stand.

Along the upper bench of the north margin (Figure 3.4), the high stand mark of episode 16 is easily identifiable as an onlap of pāhoehoe over tephra. At stratigraphic sections 2 and 3 (Figure 3.4), we measured (1) the distance along the bench from the onlap feature to the bench edge and (2) the slope angle of the bench (Figure 3.8b). These data were used to calculate the vertical distance from the high stand of episode 16 to the edge of the bench (top of the wall). We then added this vertical distance to the height of the wall to determine the total drop in lake depth from the high stand of episode 16 to the shelf in stratigraphic sections 2 and 3 (Figure 3.8b); this procedure yielded depth decreases of 6 m and 6.5 m respectively. This level is consistent with the lake depth observed at the onset of episode 17 (Figure 3.3a and Richter et al., 1970).

No significant volume of lava was added to or removed from the lake during episode 17, but low level fountaining took place for just over 11 hours (Richter et al., 1970). Photographic evidence and written accounts (Richter et al., 1970) indicate that the north margin experienced turbulent activity as episode 17 fountaining disrupted lake lava overlying the vent. Formation of a stable lake crust would have been inhibited by this surface movement, and the north margin would have been an active zone, with lava surging back and forth along the edge of the semi-stable lake margin, rolling and accreting blebs of pasty lava to the wall. The blebs would be elongate and oriented down flow in a channel, but blebs on the marker shelf point in varying directions, which we infer to indicate lava movement one way and then another during wash and back-wash of waves. The marker shelf formed in this way as lava accreted during episode 17.

The angled ramp (Figure 3.8b) on top of the marker shelf accreted first and

signals the slowing of drainback during the start of episode 17 fountaining (Figure 3.3).

As lake level stabilized, accretion and thickening of the marker shelf (Figures 3.7, 3.8b,

3.9) progressed. The flattened bubble lineations (Figure 3.9) exhibit quenched surfaces

and reflect rapid cooling of lava during staggered lowering of the lake.

Approximately 1 m below the marker shelf is another prominent shelf (Figure

3.8), but it is a relict of thickened lake crust rather than accretion. Zones *a–e* (Figures

3.8b, 3.10) reflect varying methods of formation and cooling histories. A crack opened

between the crust and wall as the surface of the lava lake cooled, allowing underlying

lava to ooze onto the surface (Richter et al., 1970; Stovall et al., 2008). Rapid quenching

of this lava formed the upper glassy texture of zone *a* (Figure 3.10) with stretched bubble

lineations and acted to re-cement the cooling and thickening crust to the wall (Stovall et

al., 2008). Eventually, the lake drained from beneath the crust, creating a small void

beneath the surface of the lava lake. The semi-molten crust dripped into the void (zone *e*,

Figure 3.10) as lava drained. Eventually, lake level dropped low enough that the crust

could no longer support its own weight above the growing void. The crust broke and fell

into the lava, sending a wave that splashed against the north margin wall (Stovall et al.

2008).

The broken face (Figure 3.10) reflects both brittle and viscoelastic behavior,

because of the progressive cooling history of the crust from top to bottom. The solidified

lava surrounding bubbles in zone *b* (Figure 3.10) is smooth and lacks the spinose texture

of the zones below, indicating brittle failure as the crust gave way. Progressing

57

downward through zone *c* (Figure 3.10), the lava is more stretched and spinose until

reaching zone *d* (Figure 3.10), where it is stretched so thinly that the remnant texture is

spiky and fibrous on a submillimeter scale. Therefore, zone *b* represents brittle crust and

zones *c – d* represent increasingly fluid lava of the viscoelastic zone exposed during

brittle-ductile fracturing (Hon et al., 1994) of the crust. The crust that fell into the lake

was covered by the underlying lava, and the remnant attached to the wall was left as a

shelf. This sequence of events and its relevance to crustal foundering is detailed in

Stovall et al. (2008).

The crust was once attached across the span of the north margin at ~450 cm

below the upper bench (Figure 3.8). This is evident as either a remnant shelf or an

oxidized zone which likely formed when the cooling, but still hot, shelf cracked away

from the wall exposing a hot surface to the atmosphere. As crust forms on a lava lake,

cracks in the surface begin to define polygonal crustal plates (Peck and Minakami, 1968).

Remnant shelves were probably left attached to the wall where such fractures formed.

The shelf is missing in some places along the wall, but pieces of it can be found on the

present lake surface. Therefore, brittle failure of these sections of the remnant shelf

occurred after final lava withdrawal and cessation of lake activity.

3.4.3 Other Features

Grooved lava (Figure 3.8), splash features (Figure 3.8), and peel-away textures (Figures

3.6, 3.8b) occur on the lake-facing surface of the rinds and indicate specific responses to

drainback.

3.4.3.1 Grooved Lava

Grooved lava (Nichols, 1938) comprises aligned marks oriented in multiple directions found on the walls. The marks cut across the spinose wall texture and must have formed by dragging of brittle surface plates across the wall before the wall-coating lava had completely solidified. The orientations of lava grooves range from vertical to nearly horizontal. Vertical grooves formed by directly downward movement of crust scraping the wall. Grooves at an angle other than vertical typically point toward the direction of the vent indicating downward and ventward movement of surface-crustal plates.

As lake level dropped during drainback, loosely attached crust or ephemeral shelves slid down the wall and scraped the still mushy outer surface of the newly exposed rind (e.g. Stearns, 1926). This can be observed in Figure 3.8a (Strat 3), where the tracks in grooved lava immediately above a broken shelf lead to the final location of the down-dropped shelf. A 19-cm-wide section of zone *a* is attached to the wall but broken and separated from an underlying 12-cm-part of the same shelf, which has been dropped 20 cm lower on the wall. Vertically oriented grooves line the wall between the upper, anchored zone 1 and the down-dropped portion of the shelf.

3.4.3.2 Splash features

These features are formed by splashing of molten lava onto the walls. Extensive swaths of splash occur along the north margin wall, especially below the lowermost shelf. When crust broke away from the north wall it must have fallen some distance into the lake, causing a splash which coated the north margin wall with drips and spray (e.g. Stovall et al., 2008).

59

3.4.3.4 Peel-away textures

Peel-away textures take the form of centimeter-scale linear glassy ledges (Figure 3.6a)

and shark's-tooth projections (Figure 3.6b, c) similar in appearance to those described by

Nichols (1939). The linear glassy ledges are on the lower 50–70 cm of the north margin

wall, where they form features (Figure 3.6a) extending several meters. These ledges

were the last structures to form along the vertical margins of the lake. Hon et al. (1994)

describe the formation of these features at the bottom of downward-propagating cracks in

pāhoehoe flows, where the apex of the crack exposes viscous, partially molten lava that

squeezes up and quenches to form a glassy protrusion. With further crack opening, these

become becomes attached to the side wall resulting in a glassy ledge. A similar process

occurred during final lowering at the margin of the Kīlauea Iki lava lake, where the

stagnant, solidifying lake cracked and peeled downward along the north margin wall,

repeatedly exposing viscous lava. Opening, and peeling along the wall and lake surface

must have occurred progressively to form the stacked glassy ledges. These features on

the wall can be matched with linear textures found on the adjacent lake surface.

This gives insight to the formation of 'shark's tooth projections' higher on the

wall, where the wall failed along a boundary of viscoelastic and plastic behavior. Nichols

(1939) describes such features as forming in viscous lava during continuous crack

propagation in lava flows. By analogy, similar structures formed along the north margin

wall during peeling of viscous lava as lake level dropped at a relatively uniform rate.

Failure resulted in a range of morphology for these peel structures from small linear

projections and stacked projections (Figure 3.6b) to larger isolated shark's tooth

projections (Figure 3.6c).

3.5 Conclusions

Kīlauea Iki lava lake houses a record of preserved features associated with late stage cycles of filling and draining. Elsewhere these features are typically either inaccessible due to dangerous conditions or are erased in active lava lakes when lake activity ceases and lava drains completely down a source vent. Kīlauea Iki offers an opportunity to study remnant features of an active lava lake, because they are preserved due to partial drainage and are easily accessible.

Two sets of features along the north margin of the lake (Figures 3.1, 3.4), vertical rinds and lava shelves, reflect steady infilling and staggered draining of lava respectively. In each episode, fountaining filled the lake progressively and led to continuous accumulation of an accreted sheet of lava in vertical rinds against the steep faces of the walls and lava islands within the lake. Lava cooled against the vertical faces until fountaining ceased, initiating drainage and lake lowering. The pattern of shelves from top to bottom reflects a change in drainage style from rapid and dynamic to slow and staggered. Immediately following fountaining, initial drainage of the lake occurred at a fast rate with vigorous flow, especially near the vent, resulting in formation of a set of thin discontinuous lava shelves attached at many levels to the previously formed vertical rind along the shore of the lake. These shelves are remnant slabs of cooled lake crust that solidified against the wall before the crust broke away and was pulled ventward during drainage. Later, slower drainage is reflected in two types of thicker, laterally continuous shelves lower on the shore walls. The dynamic lake environment, with no continuous crust and flow along the shoreline walls, led to formation of an 'accumulation shelf' marking the semi-stable lake level. In contrast, a lake with minimal activity and a surface

61

crust that solidified against the shore-line wall during a stable stand developed remnant shelves as more mature versions of the upper crustal shelves, reflecting the cooling history of the crust prior to failure. Semi-stable lake levels in the later stages of back flow were staged with slow but constant drainage; shelves formed during the stable-level periods but not while slow, steady drainage occurred.

These types of activity probably occur at all active lava lakes. Lake filling will result in the formation of a rind of lava coating the surfaces with which it came in contact. In a typical lake environment, draining of lava will form concentric shelves along the shore that may be either remnants of surficial crust or accretions of lava at a semi-stable, somewhat-active lake level, both of which may be emplaced during a pause, or slow down, in the drainage rate.

CHAPTER 4

Eruption dynamics of Hawaiian-style lava fountains:

the case study of episode 1 of the Kīlauea Iki 1959 eruption

4.1 Introduction

4.1.1 Hawaiian-style eruptions and models
Hawaiian eruptions are characterized by fountains of gas and ejecta (Figure 4.1),

sustained for hours to days, that reach 10s to 100s of meters in height. Kīlauea volcano

(Figure 4.2) is the type locality for this eruptive style (e.g., Heliker and Mattox, 2003;

Richter et al., 1970; Swanson et al., 1979). However, Hawaiian fountains have also been

observed at other basaltic volcanoes such as Etna (Bertagnini et al., 1990) and Tolbachik

(Fedotov et al., 1980). There are two conceptual models that address the mechanisms of

Hawaiian eruptions. Parfitt (2004) refers to these as the rise speed dependent (RSD)

model (Head and Wilson, 1987; Parfitt and Wilson, 1999; Parfitt et al., 1995; Slezin,

2003; Wilson, 1980; Wilson and Head, 1981) and the collapsing foam (CF) model

(Jaupart and Vergniolle, 1988; Jaupart and Vergniolle, 1989; Vergniolle, 1996;

Vergniolle and Jaupart, 1986; Vergniolle and Jaupart, 1990). The RSD model suggests

that, at high magma ascent rates, the gas phase remains coupled with the melt as a large

population of bubbles, during rise through the conduit. The key to this model is that

magma and gas are linked as a homogeneous two-phase bubbly flow that accelerates as

the gas decompresses and expands during ascent (Wilson and Head, 1981).

Fragmentation occurs when the bubble volume fraction reaches a level high enough to

cause instability and disruption of the melt (Wilson and Head, 1981). The CF model

argues that Hawaiian eruptions are the result of decoupled annular two-phase conduit flow (Vergniolle and Jaupart, 1986). In this model, degassing in a magma storage zone results in bubble rise and accumulation as a foam layer along the roof of the storage zone (Jaupart and Vergniolle, 1989). The foam collapses when it reaches a critical thickness and streams in annular fashion up the conduit as a continuous pocket of gas surrounded by an annulus of magma (Jaupart and Vergniolle, 1989). Here we provide additional model parameters to assess processes occurring between the shallow conduit and fountain during the first episode of the 1959 Kīlauea Iki eruption.
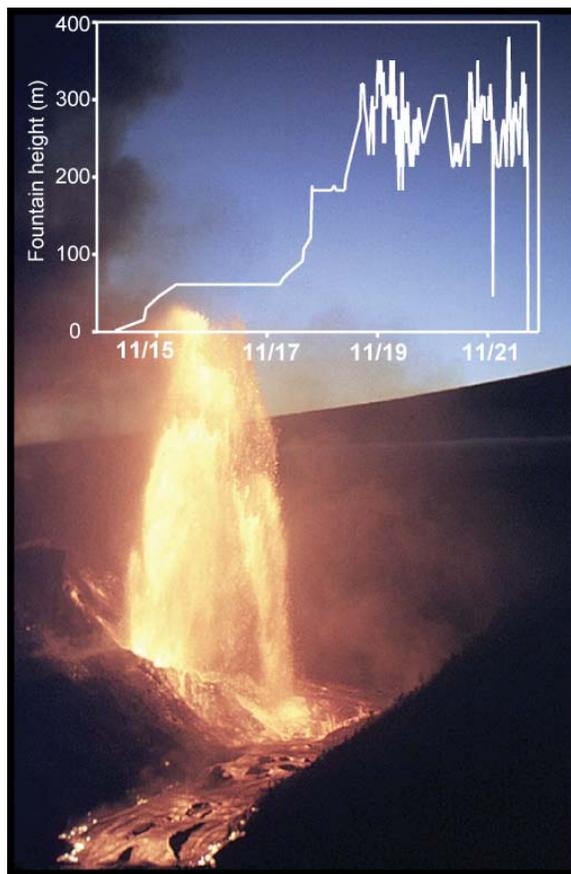
Figure 4.1 Photograph of Kīlauea Iki episode 1 fountain with inset fountain height. Taken November 18, 1959 by J. Eaton. Fountain height data collated from Richter et al. 1970 and unpublished archives (D. Richter and J. Eaton notebooks and photographs).

64
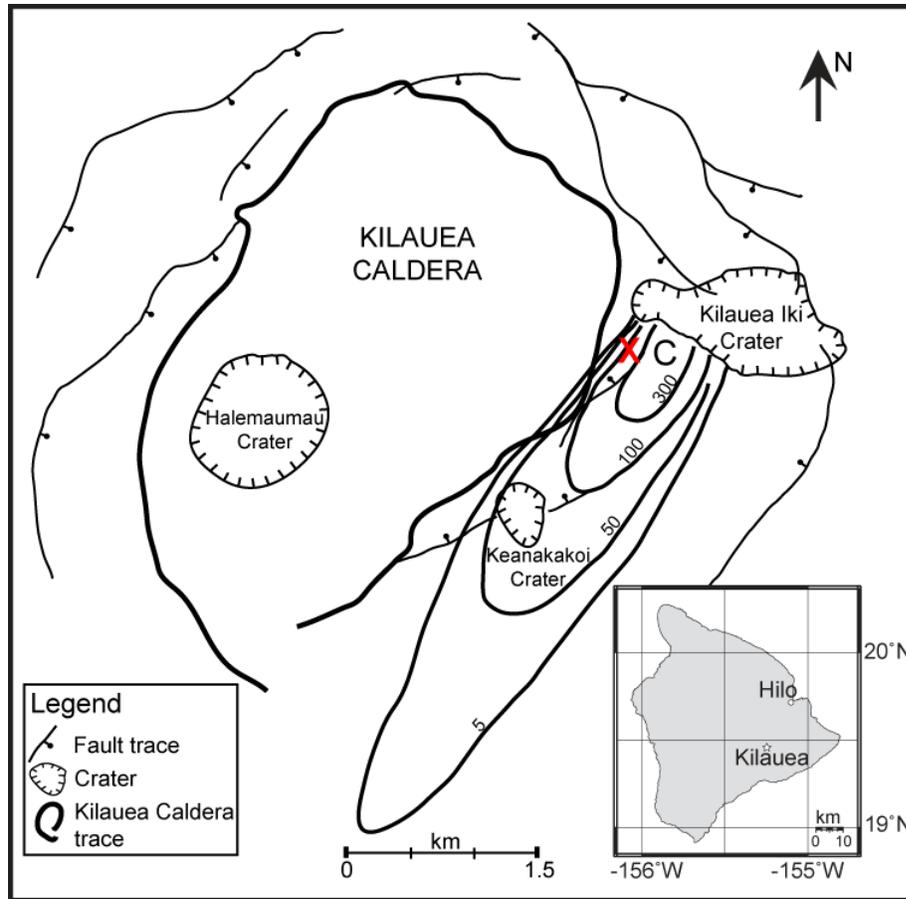
Figure 4.2 Location map of Kīlauea caldera and episode 1 study site.
(**a**) Kīlauea Caldera and Kīlauea Iki crater with tephra isopachs (thickness in cm, Houghton, unpublished data, 2008), Puʻu Puaʻi cone summit (C), and tephra pit study site (X). (**b**) Island of Hawaiʻi with star marking location of Kīlauea.

The eruption began along a fissure on the wall of the existing Kīlauea Iki pit crater on November 14, 1959. The ~1480 m by 710 m pit crater formed due to coalescence of two collapse features located within the concentric fault system of the Kīlauea caldera (Figure 4.2). Prior to 1959 the base of the east pit was 85 m below that of the west pit (Richter et al., 1970). The main vent for the Kīlauea Iki eruption was located 20 m above the floor of the west pit. Seventeen episodes lasted 36 days, producing a tephra blanket extending ~15 km downwind, a ~64-m-high cone, and a 3.7×10^7 m^3 lava lake within the pit crater. With the exception of episodes 1 and 17, each

65

episode consisted of two phases. The first phase consisted of fountaining activity (Figure

4.1) and coincident filling of the adjacent lava lake which eventually overtopped the vent.

The second phase commenced when fountaining ceased and lava drained from the lake,

back down the vent, lowering the lake. The fountaining phases of each episode varied in

length and intensity, lasting from 9 hours to 7 days (for episode 1) with peak fountain

heights between ~30 m and ~580 m (Figure 4.2).

4.1.3 Purpose
The purpose of this paper is to supply a quantitative analysis of processes occurring

during Hawaiian volcanism using the initial episode of the Kīlauea Iki eruption as a case

study. We use (1) existing observational data from Kīlauea volcano (especially Kīlauea

Iki), (2) microtextural analyses of pyroclasts from the first episode of the eruption, (3)

computational models for decompression, nucleation, and growth of bubbles and (4)

existing conceptual models for Hawaiian eruptions. We develop greater insight into post-

fragmentation processes within the lava fountain and expand the study of Cashman and

Mangan (1994) by using microtextural analysis of multiple single clasts collected over

narrow stratigraphic intervals coupled with comparisons across the diversity of textures

in Kīlauea Iki tephra.

4.2 Background and previous work

4.2.1 Previous vesicularity studies of Hawaiian ejecta
Cashman and Mangan (1994) and Mangan and Cashman (1996) conducted the first

microtextural analysis of basaltic ejecta to determine constraints on degassing in

Hawaiian fountaining eruptions. Pyroclasts from 1984–1986 Puʻu ʻŌʻō lava-fountaining

episodes were collected for their studies. Quantitative measurements were made on

planar surfaces in two dimensions which were converted to three dimensions in order to

characterize volumetric distributions of vesicles within the tephra. Vesicle diameter

measurements were made using photomicrographs but were constrained by the 0.01 cm

resolution of the digitizing tablet used for measurement.

Classification into two clast types was made based on texture and vesicularity

(Mangan and Cashman 1996). Scoria (or tephra) consists of closed-cell spherical foam

containing a broad distribution of ≤85% relatively round, undeformed vesicles. Vesicle

size data for scoria show some signs of coalescence and result in calculated number

densities between 1.8×10^5 and 1.9×10^4 cm^{-3}, nucleation rates near 2×10^4 events cm^{-3}

s^{-1}, and a growth rate of 9×10^4 cm s^{-1}. Reticulite has >95% vesicularity and is an open-

cell polyhedral foam with ~1 μm thick vesicle walls. Vesicle size data for reticulite result

in a range of calculated number densities between 1.8×10^3 and 1.1×10^2 cm^{-3} and show

an inferred signature of Ostwald ripening whereby larger bubbles grow at the expense of

smaller bubbles. Mangan and Cashman (1996) infer that the textural variation between

the two types relates to post-fragmentation expansion of clasts within the fountain.

Scoria is the more rapidly quenched end member which they believe preserves textures

equivalent to conditions upon fragmentation. If, instead of quenching upon ejection,

clasts remain in the thermally-insulated core of the lava fountain, continued vesiculation

and clast expansion would result in reticulite. The evolution from scoria to reticulite

texture incorporates a decrease in bubble-number density by two orders of magnitude

coupled with a 20% increase in vesicularity implicating a combination of bubble expansion, coalescence and ripening.

Calculated nucleation and growth rates for the Puʻu ʻŌʻō ejecta are not compatible with either the RSD or CF model for Hawaiian fountaining eruptions. Mangan and Cashman (1996) suggest the magma rise speed from the storage region to the characteristic depth of nucleation (~120 m) is rapid and exceeds the rate at which equilibrium (i.e., solubility determined) volatile exsolution occurs. This is a key in achieving a supersaturation level high enough to result in the measured vesicle size data. They presume the high degree of supersaturation within the magma results in "runaway" bubble nucleation and an accompanying vesiculation burst that coincides with fragmentation of closed-cell magmatic foam (scoria). Further vesiculation in the fountain results in expansion and maturation of textures into open-celled foam (reticulite).

4.2.2 Contemporary Unpublished Data
The U.S. Geological Survey's Hawaiian Volcano Observatory and Hawaiʻi Volcanoes National Park house multiple archives of contemporary observations from the 1959 Kīlauea Iki eruption. Field notebooks from Don Richter and Jerry Eaton record tephra accumulation rates and fine-scale height fluctuations and behaviors of the lava fountain. Photograph archives from the same scientists are stamped with time and date, and include descriptive comments relating to photograph location and fountain height. The Hawaiʻi Volcanoes National Park eruption notebook contains press releases and further detail in regard to fountaining behavior. To enhance our study, we have used these reference materials as complements to the data available in the published literature.

68

4.2.3 Review and significance of episode 1

Richter et al. (1970) give a thorough account of the events of the 1959 eruption which is

the basis for the following summary of episode 1. The eruption began at 16:08 on

November 14 when magma opened ten fissure segments along ~900 m of the south wall

of the Kīlauea Iki crater. Initial fountains reached up to 30 m in height and showered

onto the ground cascading down 100 m to pond at the base of the east pit. By the

afternoon of the 15th, the outermost vents had died and the eruption was centered at a

single location at the west end of the crater. As the flux increased, the single fountain

pushed to greater heights, raining ejecta down wind to form the Puʻu Puaʻi (gushing hill)

tephra cone (Figure 4.2). Fountains during the last five days of the first episode

fluctuated between 200 and 300 meters in height (Figure 4.1) and sometimes adopted a

wide V-shaped form thought to be due to blockages of slumped cone material in the vent

(USGS unpublished data, D. Richter and J. Eaton field notebooks and photographs). By

November 19, the cone had developed a very steep slope and the inner wall collapsed.

This removed the top portion of the cone, but it was rebuilt quickly due to high

fountaining from the vent. On November 20th, Richter et al. (1970) noted that

"…occasionally hot gas, without liquid lava, burst out with almost explosive violence

between the cone and fountain." This indicates that even during the fountaining phase of

the first episode there was explosive outgassing unaccompanied by a flux of magma

(Richter et al., 1970). The gas component was responsible for the dilute convective

thermal plume often seen above the fountain carrying small quantities of fine and light-

weight, easily-transported particles downwind. On the morning of November 21st, the

lava lake reached the vent level, but fountaining continued through the surface of the

lake. Throughout the day, spatter ramparts extending from the cone into the lake built higher, acting to stabilize the vent. However, lake lava was still encroaching into the vent and at 19:25, within 40 seconds, the fountain fell from ~210 m to zero height. Drainback of the lava lake into the source fissure was first noticed on the 22nd and continued through November 23rd.

This first and longest fountaining phase of the Kīlauea Iki eruption lasted for 7 days, reached a peak fountain height of 380 meters (Figure 4.1), and produced the greatest volume of material (nearly 31×10^6 m^3 in the lava lake). Subsequent fountaining phases lasted only between 2 and 32 hours and had variable fountain peaks between 30 and 580 meters (Figure 4.1), the latter being the highest lava fountain recorded in Hawaiʻi. Because the lava lake drained back down the vent after each filling phase, the initial fountains from episodes 2 – 17 had to clear the conduit and vent of residual, relatively-degassed lava. In contrast to these episodes, episode 1 did not have an influence of drained-back lake lava overprinted on the discharge of the newly supplied magma.

This eruptive episode resembled other high Hawaiian fountaining eruptions such as Mauna Ulu in 1969 (Swanson et al., 1979) and Puʻu ʻŌʻō between 1983 and 1986 (Heliker and Mattox, 2003). All such eruptions started as fissures which evolved into a single locus of vent activity that progressed from low to high fountaining. Typically, activity ended rapidly with surges in height before fountaining abruptly ceased (Swanson et al., 1979). Although the duration of Kīlauea Iki's first phase was longer than the typical Hawaiian episode, the initial fountaining phases of both Mauna Ulu and Puʻu

70

'Ō'ō were one or more days longer than subsequent high fountaining episodes. For this

reason, and because of the lack of an influence of drainback lava during episode 1, it is

the most relevant episode from the 1959 eruption to use as a case study for Hawaiian

fountaining behavior.

4.2.4 Deposit Characteristics

4.2.4.1 Stratigraphy
The stratigraphy of the 1959 eruption has been studied in a series of tephra pits extending

from 300 m from vent to approximately 5 km down wind of Pu'u Pua'i. These data were

compared to data collected by HVO scientists during the eruption, who probed the depth

of the tephra along a cross-wind traverse after episodes 1, 3, 11 and the close of the

eruption. Episode 1 is the easiest to identify because it is at the base of the tephra and lies

on top of older tephra or lava flows. Additionally the clast morphology is distinctive,

with a significant component of Pele's hair and an ashy parting separating it from tephra

deposited during episodes 2 and 3. Figure 4.3 includes the stratigraphy, grain size data

and samples with selected density distributions for tephra from the episode 1 study site,

KI-07-07 (the 7th pit dug in 2007; Figure 4.2). This location was chosen based on

proximity to the vent (~350 m radially), proximity to the inferred dispersal direction, and

thickness of tephra (180 cm). Because this location is ~50 m above vent level, the

fountain height had to reach at least this height before deposition commenced in this area.

Contemporary unpublished data from USGS scientists (J. Eaton photographs) correlates

the onset of tephra accumulation on the crater rim with the late morning of November

17th when the fountain height reached ~75 m (Figure 4.1). Therefore, we infer tephra accumulation at the study site to encompass the last four to five days of fountaining.

In outcrop, the episode 1 clasts are golden to black, commonly with a shiny, glassy rind (Figure 4.4). The clast population is dominantly lapilli-sized achnelith (Walker and Croasdale, 1972). Pele's tears and hair occur throughout the lower portion of the deposit (Figure 4.3) with a relatively abundant basal subpopulation of pumice.

4.2.4.2 Grainsize
The median grain size (Figure 4.3b) of samples for the episode 1 stratigraphy has a narrow range, between -2.4 and -3.4 ϕ (5–11 mm) with the coarsest deposits in the lower portion of the sequence. The five largest clasts were measured from each sample, then averaged to yield the mean maximum clast size (Figure 4.3b). The largest clasts are located 135 to 150 cm from the top of the section, and the maximum is 54 mm diameter.

4.3 Techniques

4.3.1 Sampling
Samples of juvenile lapilli were taken from the walls of the tephra pit at our study site (Figure 4.2) and used to quantify changes in the bulk density and vesicularity of the clast population throughout the course of episode 1 deposition. Nineteen 5-cm high samples were collected at approximately 10-cm intervals (Figure 4.3a). Sample locations were chosen to record significant relative changes in clast size and abundance of ash matrix or Pele's hair, sometimes resulting in more closely spaced tephra collections. Each sample was sieved in the field to separate clasts 16 – 32 mm diameter to be used for density measurements. The final size for each sample was between 120 and 150 clasts.
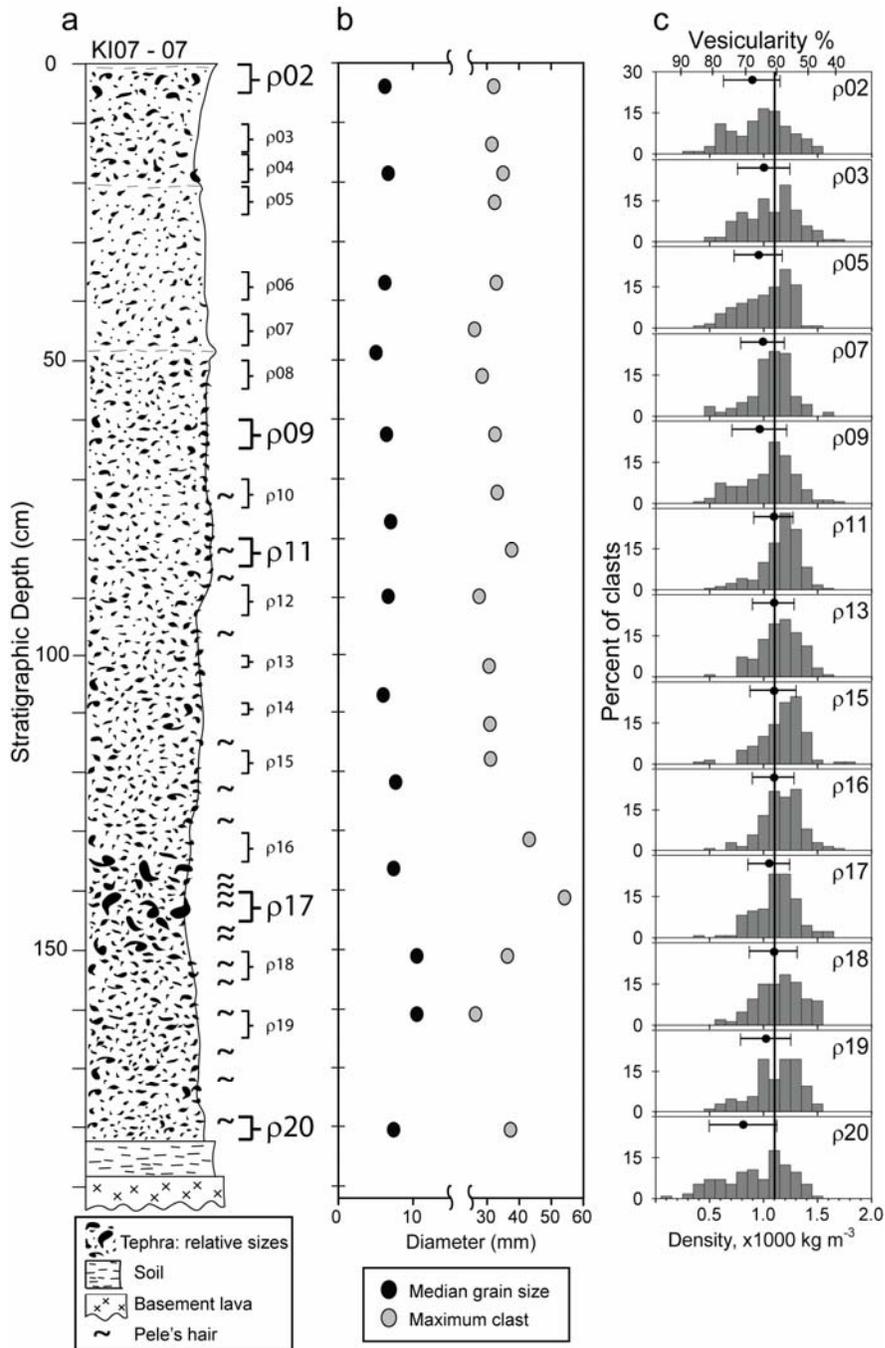
Figure 4.3 Kīlauea Iki episode 1 stratigraphy, grain size, and bulk density.
(**a**) Stratigraphy with sample locations and (**b**) median grain size and maximum clast diameter. (**c**) Density distributions for samples taken from locations labeled in stratigraphy, vertical line drawn through 1100 kg/m^3 to assist comparison, dots above histograms indicate mean density, bars equal 1 standard deviation. Maximum clast diameters are calculated from the average of three axes for each of 5 clasts. Clasts from samples labeled with larger font are used in this study for microtextural analysis.
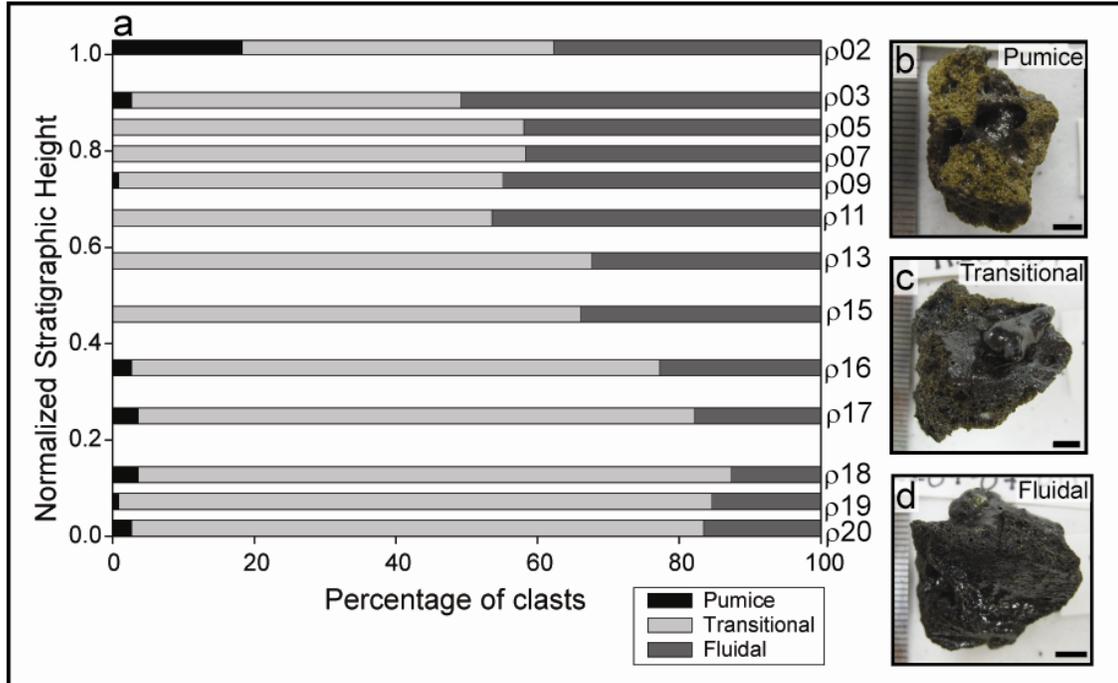
Figure 4.4 Componentry and clast photographs for episode 1 samples.
(**a**) Componentry for Kīlauea Iki episode 1 with associated samples labeled and clast-types with 5 mm bar for scale: (**b**) pumice, (**c**) transitional, and (**d**) fluidal. Componentry data are derived from processing samples of at least 100 clasts of diameter 16-32 mm.

4.3.2 Description of clast morphologies

Separation of clasts into categories for each sample from the episode 1 study side (Figure

4.1) was made in the laboratory by observing variations in clast morphology after

samples were dried in an oven at 110ºC for 24 hours to remove excess water. Two

textural extremes and one intermediate category were identified to classify the purely-

juvenile clast populations of the Kīlauea Iki tephra (Figure 4.4). 'Fluidal' clasts (Figure

4.4d) are fluidal in form, are dark brown to black with thick glass walls between

millimeter- to centimeter-sized bubbles, and have dark, shiny glassy outer surfaces.

Centimeter-scale bubbles are present within clasts or as partial imprints on the exterior

surface (e.g., semi-circular shapes on clast edges, Figure 4.5). 'Pumice' clasts (Figure

4.4b) are ragged, fragile, and golden to light brown, with thin bubble walls and abundant millimeter- to micron-sized bubbles. Some of these clasts have shiny outer surfaces but are less dense and lighter in color (dark golden brown) than the fluidal clasts (Figure 4.4d). A third, volumetrically dominant category "transitional" (Figure 4.4c) spans a range of textures between fluidal clasts and pumice. This includes clasts with textures intermediate between dark, vesicle-poor glass and golden, microvesicular glass. In hand specimen, the classification of this group is driven by either 1) the presence of ragged, brown to golden, micro-vesicular material in an otherwise dark-colored clast containing thick glass between measurable vesicles or 2) some portion of darker brown glass that is not dominantly microvesicular within otherwise golden, micro-vesicular material. Transitional clasts commonly have shiny outer surfaces. In each category, this dark-brown to black surface reflects light, looks and feels smooth, and is only found on unbroken surfaces.
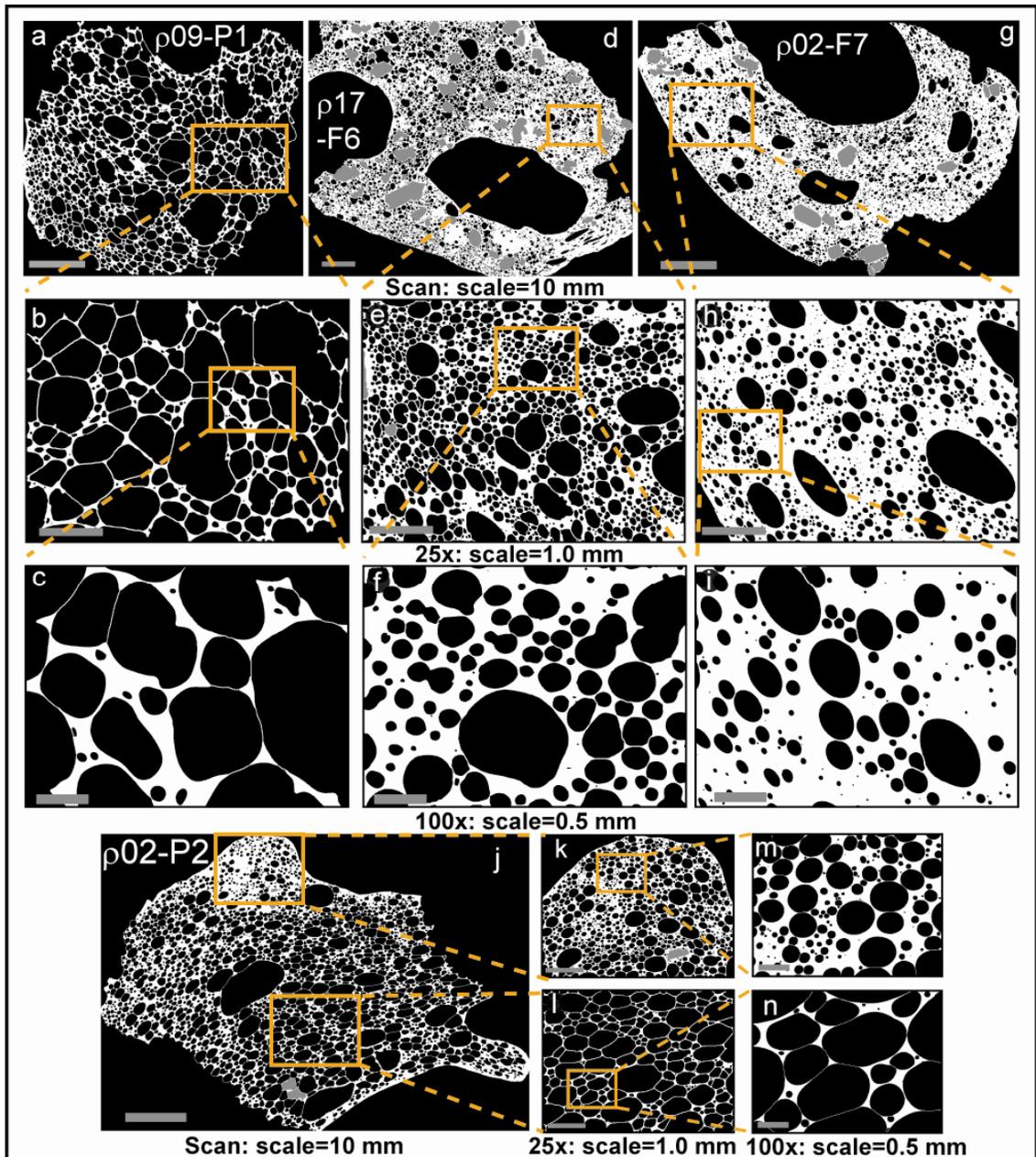
Figure 4.5 Grayscale image nests for episode 1 pumice and fluidal clasts.
(**a** through **i**) Selected clasts displaying typical pumice and fluidal vesicle textures. Thin section scans in the top row, SEM 25× magnification in second row, SEM 100× magnification in third row. (**j** through **n**) Contrasting nests of images for rind and interior of a pumice clast. Vesicles are black, glass is white and crystals are gray.

4.3.3 Density and Bulk Vesicularity

A selection of 13 density samples (Figure 4.3c) was chosen based on stratigraphic

position and to bracket abrupt shifts in grain size. All of the samples from the basal 60

cm, (ρ15 to ρ20) where the most variability in grain size occurs, were included. Above

that level every second sample was chosen together with the very top sample (KI07-07-

ρ02, ρ03, ρ05, ρ07, ρ09, ρ11, ρ13). The 13 density samples contain a total of 1822

pyroclasts from the episode 1 deposit. Density measurements were made on clasts using

the method of Houghton and Wilson (1989). The bulk vesicularity of each clast was

calculated based on a dense rock equivalent (DRE) value of 2800 kg/m^3. This DRE value

was determined using the method of Bottinga and Weill (1970) with chemical

composition of the glass from tephra sample S-5 collected on November 18, 1959 at 5:00

p.m. (Murata and Richter, 1966). These vesicularity values are not truly representative of

the matrix vesicularity because thin sections reveal relatively high and variable

phenocryst contents. Correction based on phenocryst percentages within clasts results in

vesicularities higher than these calculated (Table 4.1).

Table 4.1. Episode 1 quantitative vesicle data.

Sample (KI07-07)	Density × 1000 (kg m^{-3})	Vesicularity[a] (%)	Phenocryst Corrected Vesicularity[b] (%)	N$_{Atot}$[c] (cm^{-2})	N$_{Vtot}$[d] (cm^{-3})	N$^m_{Vtot}$[e] (cm^{-3})
ρ09-P1	0.34	87.9	87.9	2.6E+03	6.6E+05	5.4E+06
ρ17-P1	0.40	85.7	85.7	2.9E+03	7.8E+05	5.4E+06
ρ09-T6	0.52	81.4	84.5	4.2E+03	5.6E+05	4.1E+06
ρ11-T13	0.54	80.7	80.7	8.3E+03	1.7E+06	8.9E+06
ρ02-T40	0.59	78.9	78.9	9.1E+03	2.4E+06	1.1E+07
ρ02-T37	0.91	67.5	68.0	7.6E+03	2.1E+06	6.6E+06
ρ09-T29	1.09	61.1	65.1	1.0E+04	4.2E+06	1.2E+07
ρ09-T82	1.31	53.2	58.2	8.3E+03	4.6E+06	1.1E+07
ρ17-F6	1.12	60.0	67.5	5.7E+03	9.4E+05	3.8E+06
ρ20-F9	1.40	50.0	64.2	1.1E+04	2.4E+06	6.6E+06
ρ11-F12	1.50	46.4	57.6	1.2E+04	6.8E+06	1.6E+07
ρ02-F7	1.40	50.0	53.8	8.6E+03	3.9E+06	8.4E+06
ρ02-P2 rind		55.1[f]		9.4E+03	4.4E+06	9.9E+06
ρ02-P2 interior		79.6[f]		1.1E+03	1.9E+05	9.2E+05
ρ20-P5 rind		59.5[f]		8.8E+03	4.3E+06	1.1E+07
ρ20-P5 interior		73.3[f]		1.2E+03	5.8E+05	2.2E+06
ρ11-T19 rind		42.8[f]		1.2E+04	5.8E+06	1.0E+07
ρ11-T19 interior		74.9[f]		3.5E+03	8.4E+05	3.3E+06

[a]Vesicularity calculated from density and DRE of 2800 kg m^{-3} computed using formula of (Bottinga and Weill, 1970) based on composition of episode 1 Kīlauea Iki lava (Richter et al., 1970).
[b]Vesicularity calculated from density of clast minus percent density of olivine. Percent of olivine was determined by area of clast containing olivine in thin section.
[c]N$_{Atot}$ is the number of vesicles per unit area of clast matrix with phenocrysts subtracted. Values are the sum of bins from 0.005 to 40 mm.
[d]N$_{Vtot}$ is the number of vesicles per unit volume of clast matrix with phenocrysts subtracted.
[e]N$^m_{Vtot}$ is referenced to melt only, calculation based on phenocryst corrected (e) or N$_{Vtot}$-derived (f) vesicularity.
[f]N$_{Vtot}$-derived vesicularity.
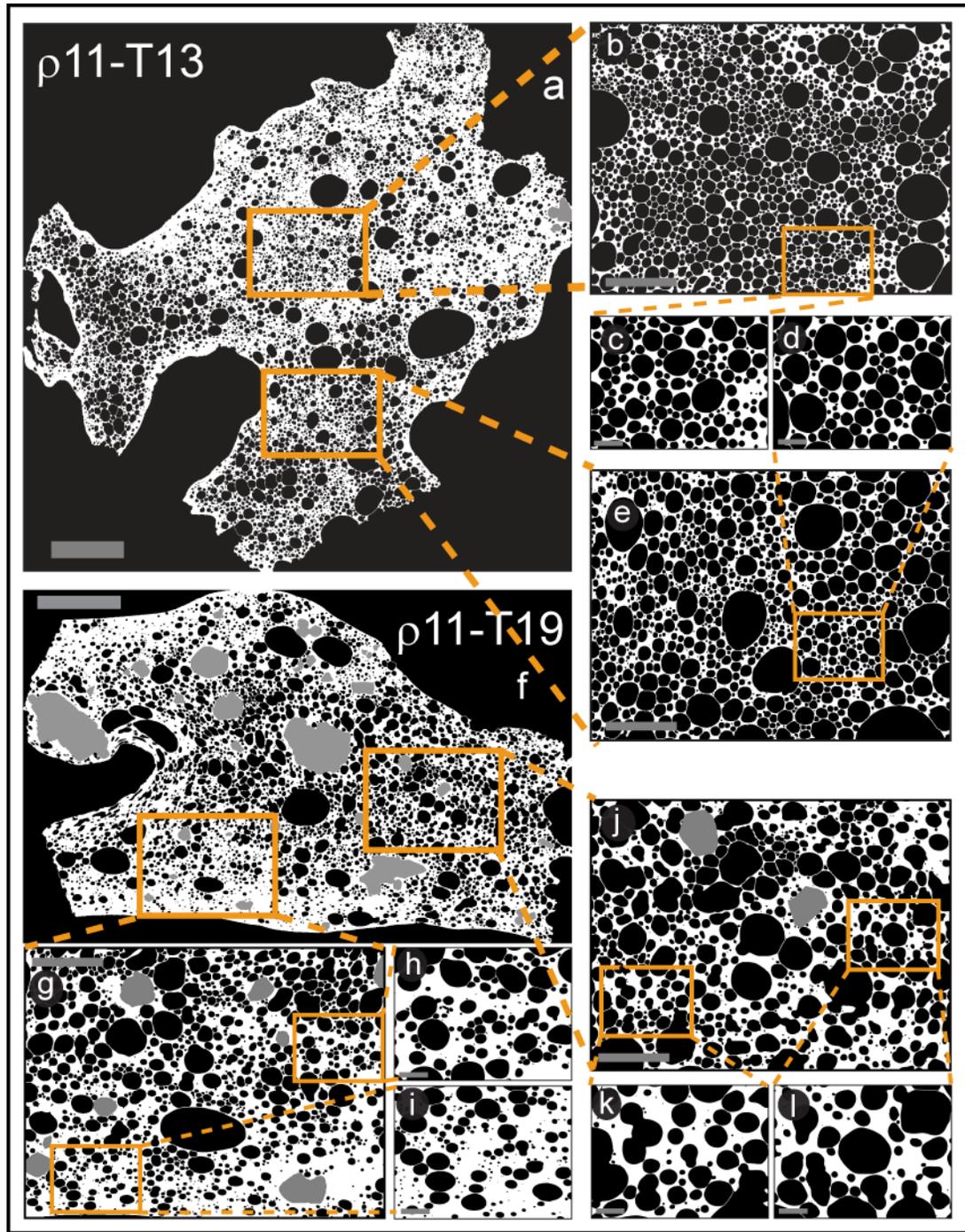
Figure 4.6 Binary image nests for homogeneous and heterogeneous transitional clasts.

Image nests of a homogeneous-transitional (**a-e**) and a heterogeneous-transitional (**f-l**) clast. Scale on binary thin section scans (**a**, **f**) is 10 mm, scale on SEM 25× magnification (**b**, **e**, **g**, **j**) is 1.0 mm, and scale on SEM 100× magnification (**c**, **d**, **h**, **i**, **k**, **l**) is 0.5 mm.

4.3.4 Textural analysis

Samples for thin section preparation were chosen based on their density distribution

relative to the entire suite (Figure 4.3c). We included the top and bottom sample (ρ02

and ρ20) to ensure capture of the ramp-up and end of fountaining. We selected samples

in the center of the deposit, making sure to include the region of maximum clast size

(ρ17), the strongest unimodal density peak (ρ11), and a bi-modal distribution (KI07-07-

ρ09). Textural analysis was conducted on two clasts from the modal-density peak(s) as

well as one high and one low-density clast from each selected sample for a total of 19

thin sections (as per Gurioli et al., 2005). Nested image sets were made using three

magnifications (Scan, 25× and 100×; e.g., Figures 4.5, 4.6). The scanned images were

captured at 1200 dpi using transmitted light on an HP flatbed scanner, and the higher

magnifications were collected using a JEOL-5900LV SEM operating at 15 kV

accelerating voltage and 1 nA beam current in backscatter mode (BSEI). Images were

converted to binary and processed for clarity in Adobe Photoshop. Quantitative vesicle

analyses were conducted with FOAMS, a Matlab GUI developed by T. Shea (pers.

comm. 2008) which incorporates the methods of Adams et al. (2006) and the

stereological volume conversion of Sahagian and Proussevitch (1998) to yield bubble

size distributions (BSD) and vesicle volume distributions (VVD) for each clast. Of the

19 clasts analyzed, 12 (clasts listed in Figure 4.7) have homogeneous textures. Regions

within three of the heterogeneous clasts (listed in Figure 4.8) were separated into distinct

textural zones that can be compared with each other and with homogeneous clasts.
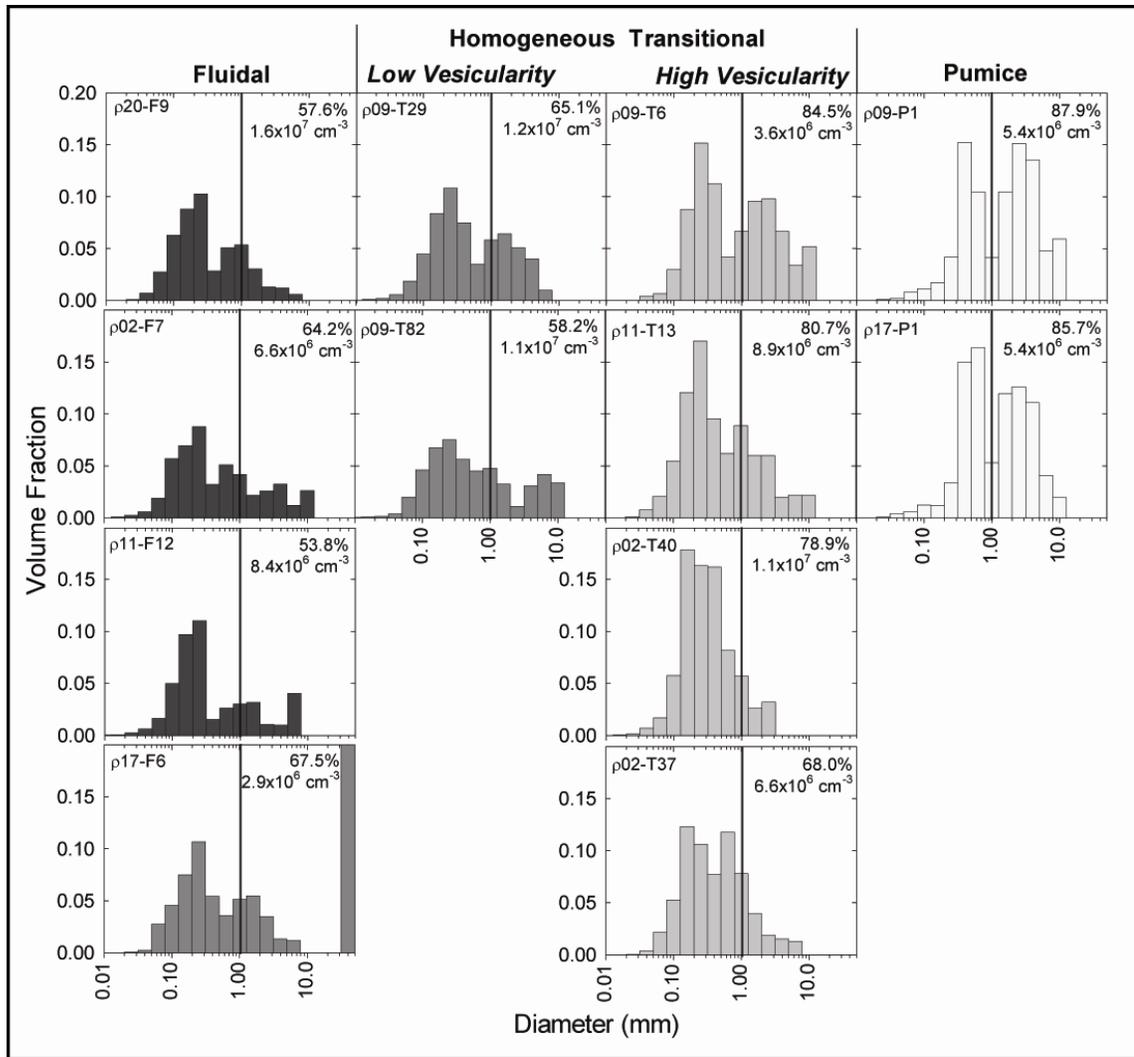
Figure 4.7 Vesicle volume distributions for homogeneous episode 1 clasts.

Distributions of volume fraction of vesicles within a specific size range (VVD) arranged according to vesicularity and vesicle number density. Sample number, vesicularity, and vesicle number density per cubic centimeter included with each histogram (also found in Table 1). Dark- to light-gray shading corresponds with vesicularity grouping. Vertical lines are drawn at 1.0 mm vesicle diameter to assist comparison.

81
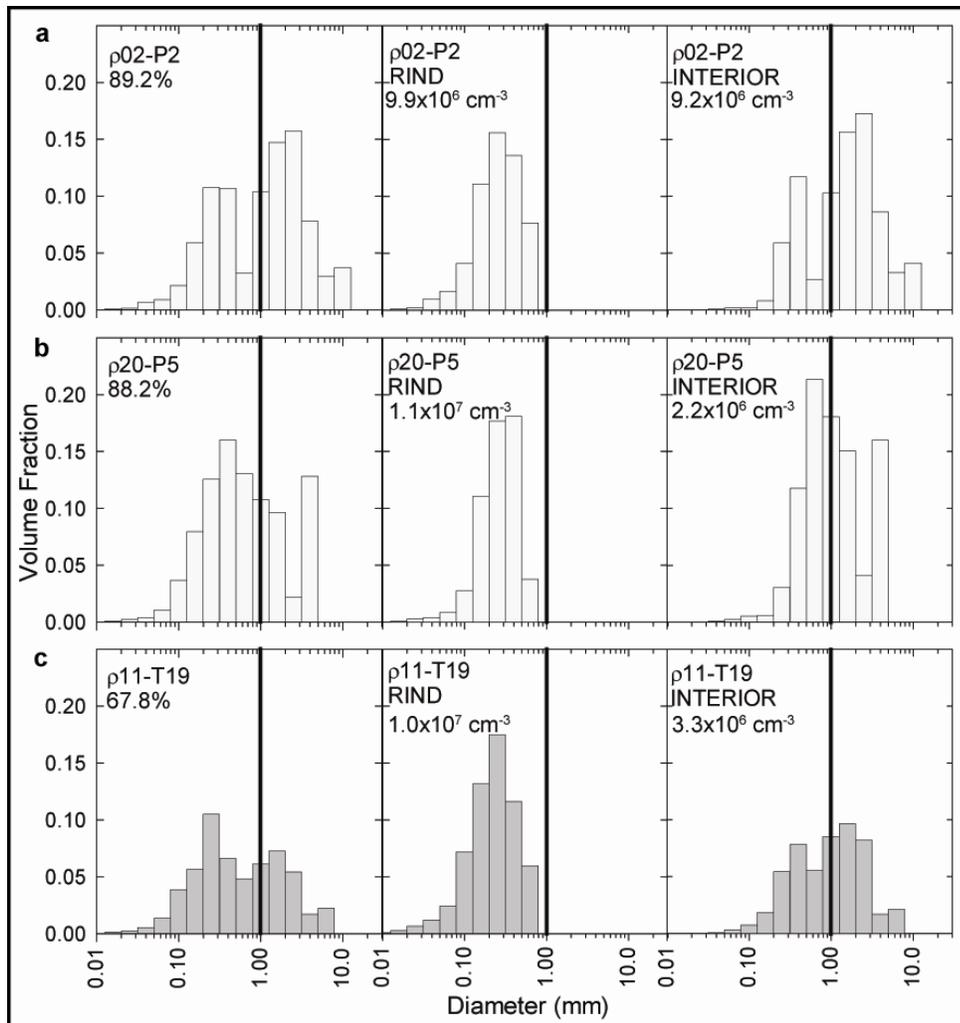
Figure 4.8 Vesicle volume distributions for rinds and interiors of heterogeneous clasts.
Volume fraction of vesicles within specific size ranges for heterogeneous clasts exhibiting textural differences between the rind and interior of clasts. VVD distributions in this case are used for qualitative comparison only. Whole clast vesicularity and VVD included in left column. Separate rind and interior vesicle volume distributions include quantitatively comparable number of vesicles per square centimeter (also found in Table 4.1).

4.4 Results

4.4.1 Density and vesicularity
The most diverse episode 1 samples in terms of bulk density and vesicularity are at the

top and bottom of the deposit (Figure 4.3c). Clast populations from sample $\rho20$

encompass the widest density range (50–1400 kg/m^3) and include the greatest percentage

of high vesicularity (low density) clasts. Sample ρ02 has a similarly broad yet bimodal

density distribution (290–1450 kg/m^3). All other samples, have primarily unimodal

density distributions and mean values between 950–1090 kg/m^3. The highest-vesicularity

clasts are pumice; the fluidal clasts are typically the least vesicular. Transitional clasts

span a range of vesicularity and contain vesicle concentrations from ~50% to 90% with a

mean near 60%.

4.4.2 Qualitative microtextural observations
The Kīlauea Iki episode 1 clasts are dominated by round vesicles, ranging in diameter

from 5 microns to a few centimeters (e.g., Figures 4.5, 4.6, 4.9). Textures vary between

clasts, from those with relatively-homogeneous concentrations of many vesicle sizes

(Figure 4.5a, d, g) to others with preferential clusters of smaller and larger vesicles

(Figures 4.5j, 4.6f). A significant number of clasts possess texturally distinct rims

(Figures 4.5j, k, 4.6f-i), characterized by populations of small vesicles (<0.01 – 0.1 mm)

which enclose zones containing larger vesicles (1 – >4 mm) in the clast interiors (e.g.,

Figures 4.5j, l, 4.6f, j-l). Local elongation of vesicles occurs in some clasts and mimics

the shape of the clast exterior (Figures 4.5d, g, 4.6f, 4.9a). Coalescence textures are

visible in thin section as outsized, typically amoeboid, vesicles (Figures 4.5a, 4.6f, 4.9b),

sometimes with irregular bubble walls (Figure 4.5b). Pumice clasts lack abundant small

vesicles and contain dominant moderate-sized vesicles with very thin (one-micron-wide)

bubble walls (Figure 4.5g, l). In the extreme case these bubbles take on polygonal

shapes. Fluidal clasts contain a rather uniformly spaced distribution of many vesicle

sizes (Figure 4.5d, g). In general, the contrast between pumice and fluidal clasts is marked by smaller vesicle sizes and greater glass wall thicknesses (Figure 4.5).

Transitional clasts span, in the broadest sense, a range of textures intermediate between fluidal clasts and pumice. Figure 4.6 illustrates the two extremes of texture seen. In one case (Figures 4.6a, 4.9a, d) the clasts contain a very narrow rim on unbroken surfaces characterized by an absence of intermediate- to large-sized vesicles enclosing a broad homogeneous core with markedly larger vesicles and thinner bubble walls. In clast ρ11-T13, the homogeneous bubble size distribution in the interior of the clasts is clearly visible in the similarities between the two 25× images in Figure 4.6 (b, e) and between the two 100× images (Figure 4.6c, d). In such individual 'homogeneous' transitional clasts (Figure 4.9) the range of vesicle textures spans amoeboid vesicles with thinner glass walls (Figure 4.9a-c) to round vesicles with thicker walls (Figure 4.9d-f). In the other extreme, two different textures are seen, forming regions with gradational boundaries (Figure 4.6f); we call these 'heterogeneous' transitional clasts. One type of region, often extending inward from the margins of the clasts, consists of a population of relatively uniformly-sized and relatively small vesicles that are widely spaced in microlite-free glass (Figure 4.6f). The other, often in the interior of the clast, contains populations of much more widely spaced and typically slightly larger vesicles (Figure 4.6f). These contrasts extend to all bubble sizes which can be seen in the comparison between the two nests of 25× and 100× images (Figure 4.6g-l).
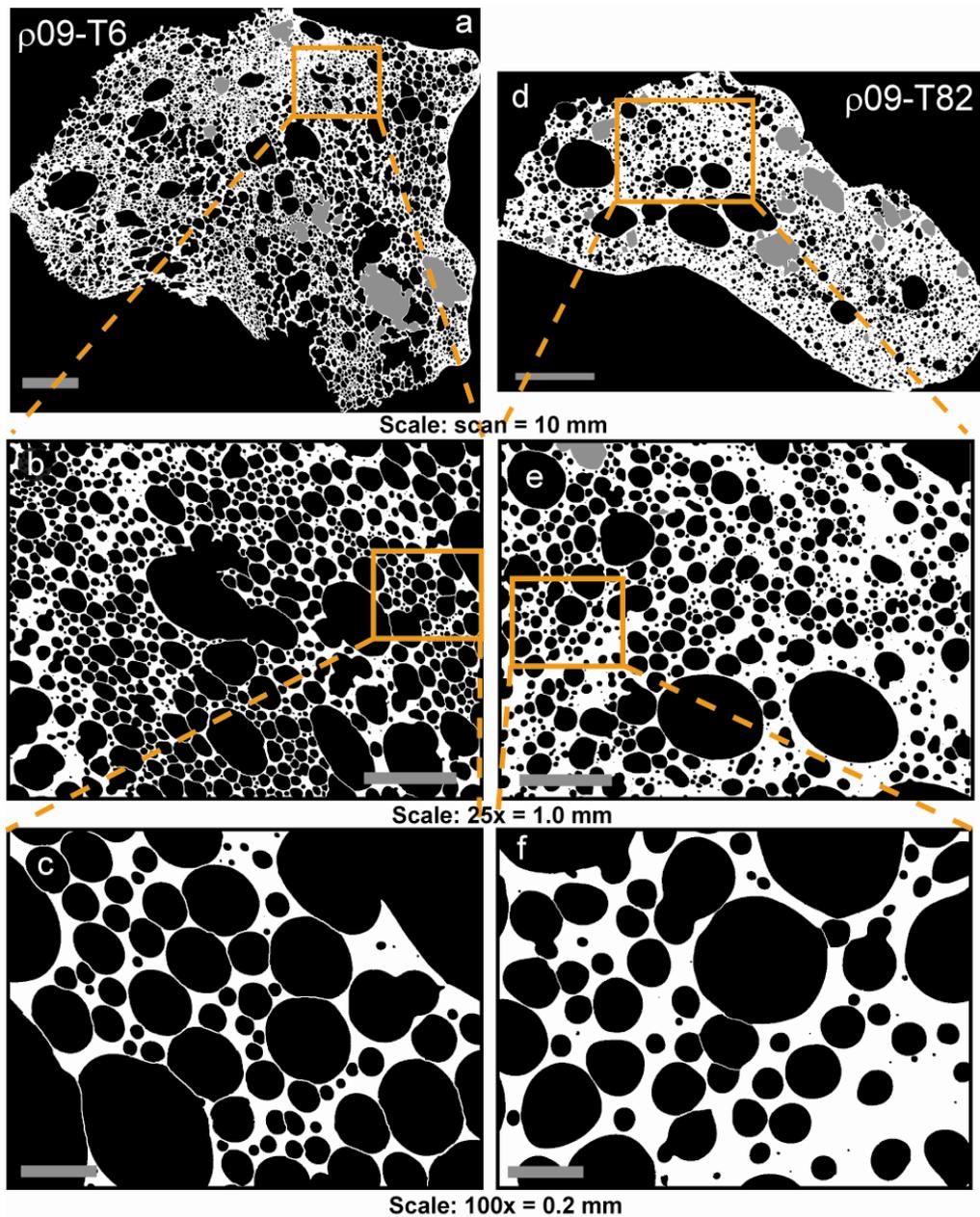
Figure 4.9 Grayscale image nests for end-member vesicularity of episode 1 homogeneous transitional clasts.

Thin-section scans in top row, SEM 25× magnification in middle row, and SEM 100 × magnification in bottom row.

Olivine phenocrysts and oxide microphenocrysts are common in all except the

most vesicular clasts and do not affect vesicle distribution (Figures 4.5b-c, 4.6).

Microlites are rare and, when present, do not influence bubble shape.

4.4.3 Quantitative microscopic vesicle data

Image analysis of clasts from the first episode of the Kīlauea Iki eruption has produced a large volume of vesicle data which enhances that previously available for Hawaiian eruptions (Table 4.1 and Figure 4.7). Analysis of the vesicularity data is used to determine the roles of bubble nucleation, growth and coalescence from the time of eruption until quenching of the clasts. Vesicle volume distributions (VVD) for homogeneous clasts are included in Figure 4.7 and represent the volume fraction of vesicles in a certain geometric size range (bin) for the 12 analyzed clasts. In 9 of 10 clasts with <81% vesicularity (Figure 4.7), there are significant numbers of vesicles in bins between 5 and 10 μm that account for a low volume percentage and thus do not appear on the VVD plots. Therefore, the x-axis has been truncated to include only those bins where the data are clearly visible on the histograms. The 5 – 10 μm vesicles dominate the number density, i.e., the number of vesicles per unit volume (N_{Vtot} and N^m_{Vtot}) for the clasts in which they appear.

VVDs for homogeneous clasts in Figure 4.7 are organized by textural type and vesicularity. Volume distributions are primarily bi- to tri-modal, and the strongest correlation across the majority of clasts is the peak at 0.25 mm diameter, present in 8 of 12 clasts analyzed. The coarsest vesicle modes are consistently in high-vesicularity pumice clasts (right column, Figure 4.7), which are bimodal with concentrations in two size ranges, 0.40–0.63 mm and 2.50–4.00 mm diameter. Fluidal clasts contain a sharp vesicle peak at 0.25 mm diameter with few vesicles >1.00 mm diameter. Volume distributions for homogeneous transitional clasts span the range between pumice and

86

fluidal. There is a rough trend in the homogeneous-transitional clasts with vesicularity. In the 'high vesicularity' column, vesicle volumes for bubbles <1.00 mm diameter increase as vesicularity increases until the vesicle population coarsens at the expense of smaller diameter classes. The concentration of vesicles >1.0 mm diameter in the highest-vesicularity transitional clast (ρ09-T6, Figure 4.7) is greater than that in any other transitional clast but less than in pumice clasts.

Vesicle number densities (VND) are included in Table 4.1, which were measured as vesicles per unit area (N_{Atot}, number per square centimeter) and converted to vesicles per unit volume (N_{Vtot}, number per cubic centimeter). Melt-corrected vesicle number densities (N^m_{Vtot}, Table 1) are calculated to remove the effect of vesicles and referenced to only melt (following Klug et al., 2002) rather than to bulk rock (i.e., N_{Vtot}). N_{Vtot} values for the opening episode of the Kīlauea Iki eruption range from 5.6×10^5 cm^{-3} to 6.8×10^6 cm^{-3} (Table 4.1, $N^m_{Vtot} = 3.8 \times 10^6$ cm^{-3} to 1.6×10^7 cm^{-3}). In comparison to other dry basaltic eruptions, our bulk number densities are markedly higher than both lava flows from Kīlauea ($\sim10^3$ cm^{-3}; (Mangan et al., 1993) and previous studies of Hawaiian reticulite and scoria (1.1×10^2 cm^{-3} to 1.8×10^5 cm^{-3}; (Mangan and Cashman, 1996) and moderately higher than lapilli from Stromboli volcano ($N_{Vtot} = 9.3 \times 10^4$ to 1.3×10^6 cm^{-3}; $N^m_{Vtot} = 1.9 \times 10^5$ to 3.4×10^6 cm^{-3}; (Lautze and Houghton, 2007). However, our number density values partially overlap products from Villarrica volcano on the low end ($N_{Vtot} = 6.4 \times 10^4$ to 2.1×10^6 cm^{-3}; $N^m_{Vtot} = 7.4 \times 10^5$ to 1.4×10^7 cm^{-3}; (Gurioli et al., 2008), and from the 122 BC Etna basaltic-Plinian eruption on the high end ($N_{Vtot} = 2.6 \times 10^6$ to 6.1×10^7 cm^{-3}; (Sable et al., 2006). The span of episode 1 number densities

87

falls within the range of products from the explosive Keanākakoʻi eruption at Kīlauea

(9.5×10^4 to 1.0×10^7 cm^{-3}; (Mastin et al., 2004).

4.5 Interpretation

4.5.1 Interpretation of macroscopic data

Variation in clast morphology and componentry within the otherwise strikingly uniform

episode 1 tephra (Figure 4.3a) are first order parameters necessary for interpreting the

dynamics of this eruption. Morphological differences between clasts reflect macroscopic

abundance and spacing of vesicles. This influences bulk clast density; pumice clasts

typically have the lowest density (highest vesicularity) and fluidal clasts have the highest

density (lowest vesicularity) with transitional clasts falling in between and typically

defining the density/vesicularity mode for each sample. The deposit is dominated by

transitional clasts (Figure 4.4). Both the vesicle population enclosed within single clasts,

and the imprinted larger centimeter-scale vesicles on the exterior of clasts, indicate that

the gas fraction in the form of bubbles spanned a large size range, at least 3 orders of

magnitude, in the moments just prior to fragmentation. The shiny outer surfaces of clasts

are the late-stage product of fusion by hot gasses streaming through the fountain

(Thordarson et al., 1996).

The slight fluctuations in density and bulk vesicularity in the episode 1 sample

suite can be linked to minor changes in eruption and fountain behavior once the Kīlauea

Iki vent was well established. Because fountaining proceeded for approximately two and

a half days prior to major tephra accumulation at the study site, it is probable that the high

abundance (18% of sample ρ20) of easily-transportable pumice (82–98% vesicularity) at

88

the base of the stratigraphy reflects relatively light clasts that were partitioned into the

dilute convective plume (e.g., Manua Ulu, Swanson et al., 1979) above the low fountain

during the first days of the eruption (Richter et al., 1970). The transitional to fluidal

clasts within sample $\rho 20$ (Figure 4.4) define an overall peak density of 1100 kg/m^3

(~60% vesicularity) which is slightly lower than the peak from overlying samples.

Fountain height and mass discharge ramped up during deposition of this sample, and the

majority of clasts landing in the study site during this time probably came from the upper

fountain, which was also dominated by lower-density clasts, that were more easily

transported to greater heights (Parfitt and Wilson, 1999). Therefore, the first several

centimeters of relatively low-density transitional to fluidal tephra represent sedimentation

from the top of the growing fountain.

Samples from the majority of the deposit have uniform clast densities and

corresponding modal vesicularity of 66% to 61% (Figure 4.4b), which is predictable due

to the sustained nature of the fountain during this period of deposition. The sharply

unimodal density distributions (e.g., $\rho 15$ and $\rho 11$) indicate that the conduit was occupied

by relatively uniform magma that then underwent similar post-fragmentation processes.

Samples from the top of the deposit have similar density distributions to those of

the lowermost samples (Figure 4.3), but the fountain behaved differently at the close of

the episode. During the last 10 hours, the lake level overtopped the vent level and the jet

had to push through the overlying lava. This overburden of lava added complexity to the

previously steady fountaining. The fountain base widened (USGS unpublished data, D.

Richter and J. Eaton photograph archives), and although reaching instantaneous heights

of up to ~240 m during the last 10 hours, fountaining was not sustained and heights pulsated between that maximum and ~100 m until the abrupt end of the episode (Figure 4.1). Again, the modes in sample $\rho02$ (from the top of the sequence) are shifted toward lower densities compared to the bulk of the deposit, suggesting an increased amount of sedimentation from the upper, low-density regions of relatively low fountains during fluctuating heights. Sample $\rho03$ lies just below $\rho02$ and is trimodal, which deviates from the strongly unimodal density distributions below this stratigraphic level. Assuming an even sedimentation rate over ~4.5 days, ~1.7 cm of tephra was deposited every hour at the study site. The lava lake reached vent level ~ 8 hours before the eruption ceased, which corresponds to the uppermost ~13 cm of tephra accumulation, equivalent to samples $\rho03$ and $\rho02$ (Figure 4.3a). Therefore, lake-influenced fountain fluctuations are likely responsible for the polymodal density distribution of clasts from sample $\rho03$ (Figure 4.3c).

Grain size does not vary widely throughout the deposit (Figure 4.3b), and maximum clast data have no strong correlation with the median grain size. Based on fountain height (Figure 4.2) and inferred deposition rates above, we correlate the level of the largest episode 1 clasts (Figure 4.3b) with November 18th, when the fountain height surged to reach 320 m for the first time. Median grain size data are typically relied upon to serve as a proxy for eruption intensity (e.g., Sable et al., 2006). The lack of variation exhibited in the episode 1 deposit is consistent with the discharge remaining relatively constant with a slight increase around November 18th, resulting in the deposition of the maximum clast sizes at that time.

4.5.2 Interpretation of quantitative vesicle data

In Hawaiian eruptions, large clasts remain sufficiently hot and plastic to permit considerable post-fragmentation deformation. Therefore, vesicle analysis data will not only include clues to conditions at the moment of fragmentation, but also will indicate processes that occur after fragmentation. There are features common to all pyroclasts as well as differences among clasts both among and within samples.

4.5.2.1 Features common to all pyroclasts

The 1959 clasts have a predominance of simple ellipsoidal to spherical bubble shapes across all size ranges. In this regard they contrast drastically with the vesicle population in basaltic Plinian pyroclasts (Sable et al., 2006). This suggests that characteristic relaxation times for bubbles (i.e., the time for coalesced bubbles to return to spherical) are generally achieved in the Kīlauea Iki fountains, unlike the basaltic Plinian eruptions. In addition, the principal size mode for vesicles in all the pyroclasts is typically 150-350 μm, irrespective of clast vesicularity. We interpret these features to reflect the common early history of episode 1 pyroclasts. Where variabilities in vesicle size, shape, and distribution are apparent between clasts, they reflect a later divergence in degassing and bubble growth during conduit ascent and fountaining. The studied clasts have a wide range in morphology and vesicle size distribution but have very similar vesicle number densities (N^m_{Vtot}, Table 1) between 3.8×10^6 cm^{-3} to 1.6×10^7 cm^{-3}. This observation alone suggests that the 1959 melt had a relatively uniform history of bubble nucleation and that textural diversity arose principally in the interval between the cessation of bubble nucleation and quenching. In the sections below we explore the nature of this diversity.

91

4.5.2.2 Textural variability within clasts: rinds and interiors

Vesiculation processes impart a characteristic signature (Figure 4.10) on a plot of vesicle-to-melt ratio (V_G/V_L after Gardner et al., 1996) and VND (Figure 4.10). Addition of newly nucleated bubbles leads to increased VND and only a slight increase in V_G/V_L. Bubble growth by some degree of combined diffusion and decompression leads to increased V_G/V_L at constant VND. VND decreases while V_G/V_L increases during bubble coalescence, whereas loss of bubbles via collapse or buoyant rise leads to a reduction in both parameters. Intermediate trends on the diagram reflect combinations of more than one of these processes.

We use an analysis of the pumice clast ρ02-P2 as a case study to explore the nature of the rims present on many pyroclasts. In this clast, a rind characterized by a large number of small vesicles with mm-thick walls (Figure 4.5j, k, m) grades sharply inward into a population of much larger vesicles with micron-thick walls clustered in the center of the clast (Figure 4.5j, l, n). Whole-clast volume conversions for heterogeneous clasts (e.g., those with rinds and interiors) are not possible due to the presence of zones of vesicles with variable sizes. However, vesicle volume data for single nests of images within separated zones are accurate. Individual VVD histograms for the rind and core of this and similar clasts (Figure 4.8) combine to give a bimodal distribution of high volumes of vesicles in two size classes (Figure 4.8a, 0.40 mm and 2.50 mm) for the clast as a whole. N_{Vtot} values for the rind and clast interior are 4.4×10^6 cm^{-3} and 1.8×10^5 cm^{-3} respectively (Table 4.1). Melt correction of VND was calculated for each zone based on the N_{Vtot}-derived vesicularity, because density-derived vesicularity for individual zones could not be calculated. Based on comparisons of density-derived vesicularity and

N_{Vtot}-derived vesicularity for whole clasts, this approximation may result in a ~5% error in the vesicularity calculation. N^m_{Vtot} for the rind and clast interior are 9.9×10^6 cm^{-3} and 9.2×10^5 cm^{-3} respectively (Table 4.1).
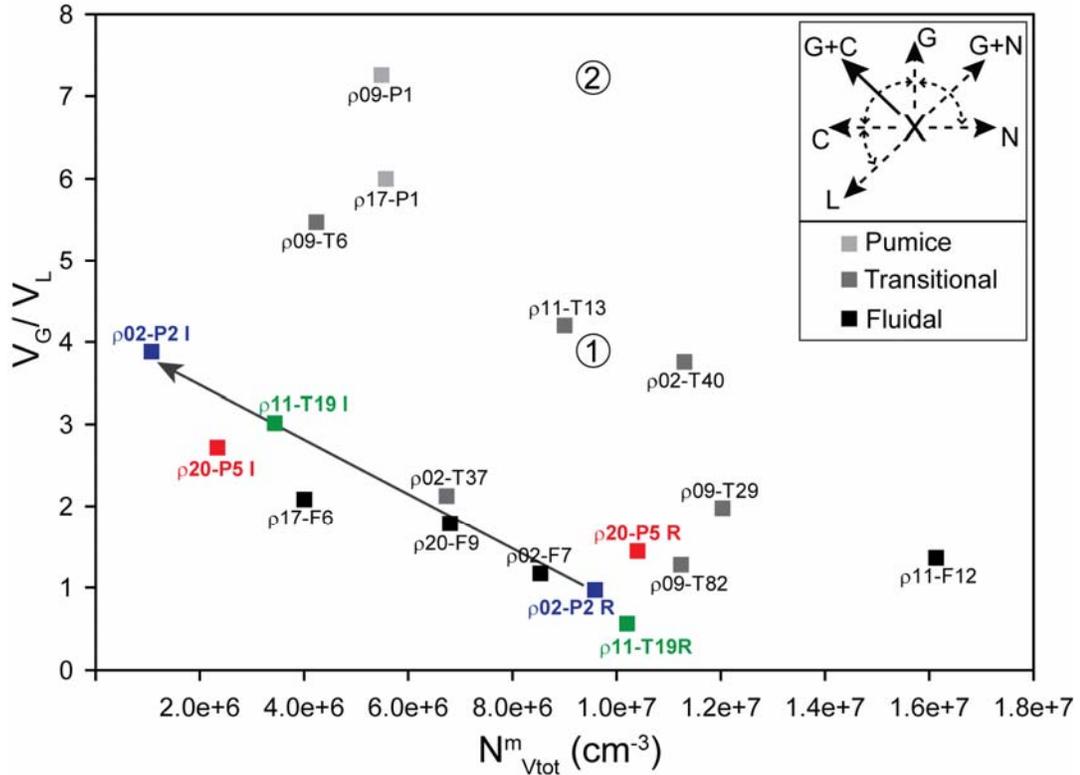
Figure 4.10 Volumetric ratio of vesicles to melt (V_G/V_L) versus vesicle number density (N^m_{Vtot}) for episode 1 clasts.

Data points are labels of clast name; R (rind) and I (interior) following same clast name indicate data from specific zones. Inset graph depicts vesiculation trends originating at X proceeding via decompressive plus diffusive growth only (G), growth plus nucleation (G+N), nucleation only (N), growth plus coalescence (G+C), coalescence only (C), and bubble loss (L). Our study indicates low V_G/V_L and high N^m_{Vtot} clasts most closely resemble melt at the time of fragmentation with further vesiculation processes proceeding from that point. Circled numbers are points used in calculating relative growth and coalescence for melt originating with parameters equal to ρ02-P2R and expanding to ρ02-P2I (1) and ρ09-P1 (2) as discussed in the text. The arrow indicates the pathway necessary to achieve the interior texture originating at the rind texture for clast ρ02-P2.

In this section we interpret the difference in vesicle texture between rind and interior for sample ρ02-P2, assuming that the interior had the same vesicle characteristics as the rind upon exit from the vent but was subsequently modified during transport in the fountain (e.g., Mangan and Cashman, 1996) by some combination of bubble nucleation, growth and coalescence. The interior has approximately a 3-fold increase in vesicle volume relative to the rind. This has to be a product of exsolution of water and bubble decompressive expansion during transport. Furthermore, the 10-fold decrease in N^m_{Vtot} between rind (9.9×10^6 cm^{-3}) and interior (9.2×10^5 cm^{-3}) indicates significant bubble coalescence occurred during transport.

Figure 4.11 includes vesicle volume comparisons at individual size ranges with the VND per cubic mm of melt (Figure 4.11a, c) as well as the for the total volume distribution of vesicles (Figure 4.11b, d). The difference in smallest vesicle volume between rind and interior is a factor of ~3 and is likely to be the consequence of bubble growth due to decompression and exsolution plus diffusion of volatiles into the bubble. It also suggests that continued bubble nucleation was probably negligible. The decrease in N^m_{Vtot} for the interior relative to rind across all vesicle sizes (Figure 4.11a, c) is strong evidence that bubble coalescence affected all bubbles. In fact, a decrease in N^m_{Vtot} from rind to interior of approximately 90% is observed for all vesicle sizes (Figure 4.11a, c). This can only be a consequence of coalescence and accounts for the stretching of the distribution by about 3 orders of magnitude toward larger sizes. The bimodality in vesicle volume fraction of the interior relative to the rind (Figure 4.11b, d) is most likely an artifact of the attenuation of N^m_{Vtot}.
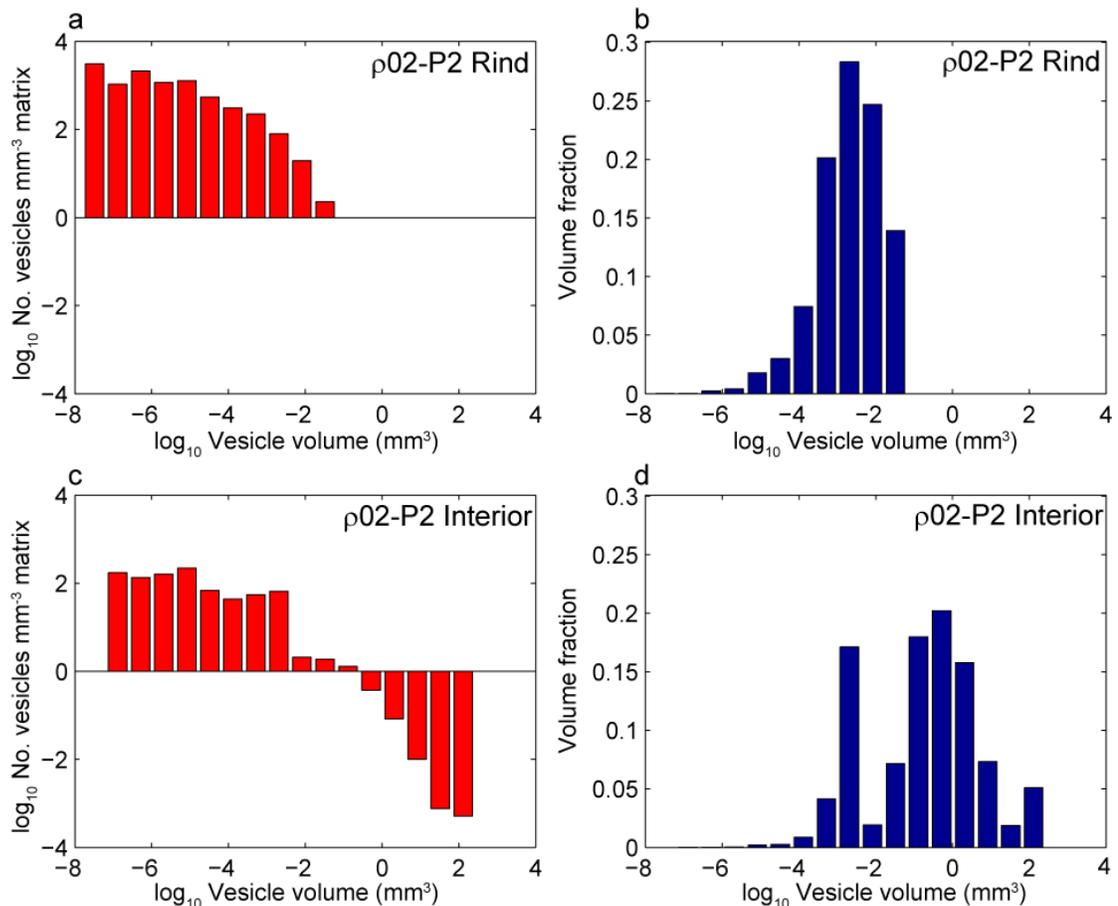
Figure 4.11 Vesicle number density and volume fraction of individual vesicle-size classes for clast ρ02-P2 rind and interior.

The horizontal axis represents vesicle volume in mm^3. Bins form a geometric progression in 6/10 log$_{10}$ volume increments. Thus successive bins increase in volume by approximately a factor of 4. (**a**) Vesicle number density per mm^3 of matrix as a function of vesicle volume for the rind of sample ρ02-P2. (**b**) Vesicle volume fraction as a function of vesicle volume for the rind of sample ρ02-P2. (**c**) Vesicle number density per mm^3 of matrix as a function of vesicle volume for the interior of sample ρ02-P2. (**d**) Vesicle volume fraction as a function of vesicle volume for the interior of sample ρ02-P2.

Pumice clast ρ20-P5, and transitional clast ρ11-T19 (Figure 4.6f), also contain

contrasting rind and interior textures and exhibit a similar decrease in VND (N$^m_{Vtot}$

Figure 4.10). These clasts (Table 1) follow the same trend of reduced number densities

accompanied by thinning of glass walls and increase in vesicle size from the rind to the

interior (Figure 4.8). Like clast ρ02-P2, in order to accommodate the increase in vesicle

size from rind to interior and the corresponding decrease in VND, the clast interiors must

have continued to expand, via a combination of bubble growth and bubble coalescence

(Figure 4.10), at the expense of the population of smaller bubbles that characterizes the

rind textures. Bubbles coalesce as walls thin (Klug and Cashman, 1996), so bubbles must

have grown to a point where melt-film rupture proceeded as a result of Van der Waals

forces (Herd and Pinkerton, 1997). To account for the presence of the rind on this and

other similar clasts, the exterior must have quenched after fragmentation while interior

growth and coalescence occurred during transportation in the lava fountain (e.g., Mangan

and Cashman, 1996). After magma leaves the vent and moves upward in the fountain,

processes of vesiculation continue, because pyroclasts remain hot during transport until

they quench to lock in the textures. Observation of video footage from the 1959 eruption

indicates that the time for a pulse of magma to travel from the vent through the fountain-

height peak to deposition is ~8 seconds for a ~250 m fountain. Therefore, clast

expansion occurred over a time interval of probably no more than 8 seconds.

4.5.2.3 Vesicularity contrasts between pumice and fluidal clasts
The distinguishing characteristics of the pumiceous clasts quantified in this study are very

high vesicularities and a vesicle size mode at 3 to 10 mm diameter which is reduced or

absent in all other juvenile clasts. Pumice clasts (Figure 4.7) have a coarser vesicularity

mode than the contemporaneous transitional and fluidal clasts. Additionally, walls

between the vesicles in the pumice are very thin, typically one to two microns thick

(Figure 4.5a-c, j, l, n). In order to achieve these vesicle sizes and wall thicknesses, these

pumice clasts must have gone through expansion histories similar to the core of $\rho02$-P2 and $\rho20$-P5, which is described above. Based on the observations related to $\rho02$-P2, we feel that all clasts within the pumice component of the 1959 ejecta have undergone significant post-fragmentation expansion in the thermally insulated core of the fountain (e.g., Mangan and Cashman, 1996), but quenched rims are only preserved on a small subset of the pumices.

Fluidal clasts show a wide vesicularity range with greater volumes of vesicles in small bins and reduced vesicle volumes in bins >1.0 mm with respect to the pumice (Figure 4.7). A size mode at 150–350 μm dominates in all the fluidal clasts which is smaller than the size modes in pumice (300 – 500 μm and 3 – 10 mm). Fluidal clasts are both lower in vesicularity than pumice clasts and (barring $\rho17$-F6) have slightly high, N^m_{Vtot} (Table 4.1). Fluidal clasts with the highest N^m_{Vtot} ($\rho20$-F9, $\rho11$-F12, and $\rho02$-F7, Table 1) contain numerous vesicles in the smallest bin sizes (5–10 μm) increasing the N^m_{Vtot} relative to pumice clasts, which contain no vesicles in the smallest size fractions.

Using textural observations and vesicle data, inferences can be made by comparing rinds (e.g., $\rho02$-P2 and $\rho20$-P5) with the lowest-vesicularity fluidal clasts (e.g., $\rho11$-F12 and $\rho02$-F7). The above interpretation suggests rinds of clasts reflect a primitive history of vesiculation relative to pumice-approximating interiors. Location of rinds with other low-vesicularity clasts in the high-end VND and low- V_G/V_L region of Figure 4.10 strongly suggests that vesicle populations in these clasts have similar histories unaffected by significant post-fragmentation expansion. Qualitative observations of combined vesicle shape and spacing for fluidal and rind textures (Figure

4.5i, m) reveal further similarities. Therefore, it is reasonable to assume the bubble

populations of rinds closely approximate those of fluidal clasts. This comparison,

combined with the presence of peak vesicle size populations of fluidal clasts smaller than

those of fountain-expanded pumice clasts (Figure 4.7), further suggests that the fluidal

bubble populations represent an earlier stage in the vesiculation history of the 1959 melt

than those of the pumices (Figure 4.10). We therefore interpret the fluidal population as

reflecting earlier quenching of melt.

4.5.2.4 The nature of transitional clasts
Most clasts sampled in this study have transitional textures with either homogeneous

(Figure 4.6a) or heterogeneous (Figure 4.6f) vesicle populations. Only homogeneous

clasts will yield whole-clast VNDs and size distributions that can be interpreted

quantitatively in terms of vesiculation processes. We ignore the clasts characterized by

heterogeneous populations in terms of whole-clast volumetric quantitative data, but still

use the qualitative observations and area measurements to deduce mechanisms for their

formation.

Transitional clasts with homogeneous vesicle populations (Figures 4.6a, 4.9)

capture a process of transformation between textures typical of the fluidal clasts (e.g.,

Figure 4.5g) and those seen in the pumice (e.g., Figure 4.5a, j). Low-vesicularity

transitional clasts (Figure 4.7) ρ09-T29 and ρ09-T82 (Figure 4.9d) have high $N^m_{V\,tot}$

(Table 1, Figure 4.7) and evenly distributed populations of rounded and coalesced

vesicles (e.g., Figure 4.9e, f). VVD for these clasts closely resemble those for fluidal

clasts (Figure 4.7) with volumetric peaks at 0.25-mm diameter and relatively sparse

coarse vesicle populations. These transitional clasts, however, show a slight increase in the vesicle subpopulations near 0.7-mm diameter. Vesicles in these low-vesicularity transitional clasts (e.g., ρ09-T29, Figure 4.9d-f) are slightly larger, more irregular and more closely spaced than in the lowest vesicularity fluidal clasts (e.g., ρ02-F7, Figure 4.5g-i), but are similar to higher-vesicularity fluidal clasts (e.g., ρ17-F6, Figure 4.5d-f).

Based on VVD and textural similarities between low-vesicularity transitional and fluidal clasts, the increase in vesicularity corresponds to a similar maturation of vesicle textures. High-vesicularity transitional clasts (Figure 4.7) ρ11-T13 (Figure 4.6a), ρ02-T40, and ρ02-T37 have a ~1 mm thick quenched glassy rim surrounding an evenly distributed population of mostly round, multiple-sized vesicles. This set of clasts has relatively similarly shaped VVDs (Figure 4.7) lacking significant vesicles >1mm and having vesicularities (68% - 81%, Table 1) that lie between fluidal (64% - 68%, Table 1) and pumice (86% - 90%, Table 1). As stated above, the highest-vesicularity transitional clast, ρ09-T6 (Figure 4.9a) has a texture and VVD (Figure 4.7) intermediate between other high-vesicularity transitional (e.g., ρ11-T13, Figure 4.6a) and pumice (e.g., ρ09-P1, Figure 4.5a) clasts. Using the texture of clast ρ09-T6 as a bridge between transitional and pumice morphologies, a proportion of the smaller vesicles expand to form larger vesicles, resulting in VVD skewed toward coarser populations. In Figure 4.10, the general trend from transitional clasts to pumice is seen as an increase in vesicularity accompanied by decrease in N^m_{Vtot} (Table 4.1). The latter implies that expansion must have accommodated some degree of vesicle coalescence. The interior of the thinly rimmed clast, ρ09-T6 (Figure 4.9a) is, in every sense, a less mature (i.e., lower-

vesicularity) form of that seen in the expanded golden pumice. Based on the comparison of pumiceous and fluidal textures above, we believe that homogeneous transitional clasts preserve varying stages of quenched textures intermediate between those two end members.

Heterogeneous transitional clasts (Figure 4.6f) capture in situ but patchy vesiculation processes on the path from fluidal to pumiceous texture. These clasts contain regions characterized by larger vesicles with coalescence shapes that are typically concentrated toward the clast center (Figure 4.6f, j-l). The more glassy regions contain smaller vesicles and are often located along quenched rims or near the edges of clasts (Figure 4.6f-i), but these glassy rim regions are much wider and more irregular than in homogeneous transitional (Figures 4.6a, 4.9) or pumiceous (Figure 4.5j) clasts. In order to form larger regions of small, widely-spaced vesicles, portions of the transitional clasts with wide rims (Figure 4.6f) must have quenched inward more rapidly than the thinly-rimmed homogeneous transitional (Figure 4.6a) and pumice clasts. Coalescence was underway when the center of the clast ρ11-T19 quenched (Figure 4.6j-l), and based on the grading from smaller to larger vesicles from exterior to interior, must have taken place after further vesiculation of the more glassy regions (Figure 4.6g-i) in the clast was arrested.

4.5.2.5 Textural variability among clasts within samples
Given our estimated duration for accumulation at the study site, each sample represents sedimentation of approximately 2.5 to 3 hours. The diversity of pyroclasts in each

100

sample therefore reflects the heterogeneity of the melt phase in the shallow conduit as well as textural maturation in the fountain on these time scales.

In every sample, similar variations exist in the VVD and textural range of erupted material. Figure 4.9 depicts the textural variability in clasts from one sample (ρ09). These are the lowest and highest vesicularity transitional clasts in the study and are clasts most similar to fluidal and pumiceous textures respectively. If melt approximating ρ09-T82 (Figure 4.9d) continued to vesiculate, it is conceivable that the small (5-30 μm) vesicles (e.g., Figure 4.9f) grow, larger vesicles with thin film boundaries would coalesce, early-coalesced vesicles would relax, and then additional coalescence would occur to yield a texture comparable to that of ρ09-T6 (e.g., Figure 4.9c). A decrease in N^m_{Vtot} (1.1×10^7 cm^{-3} to 4.1×10^6 cm^{-3}, Table 1), and VVD comparison for these two clasts (Figure 4.7), confirm this as a possible trend, with complete loss of the vesicle population below 30 μm and increase in proportions of vesicles >1 mm. A similar trend can be seen by comparing N^m_{Vtot} and VVD for clasts ρ11-F12 with ρ11-T13 (Figure 4.7). Textural evidence of varying degrees of post-fragmentation vesiculation implies different cooling histories for fluidal and pumiceous clasts. Additionally, contrasts in cooling rate are evident within individual clasts containing regions of differing vesicularity, e.g., clasts with dense glassy rinds and more-vesicular interiors.

Within a single sample, the simple post-fragmentation vesiculation trend discussed above, from fluidal to transitional to pumice, does not always hold. For example, although there is a trend between end-member vesicularity transitional clasts in sample ρ09, the pumice clast from that sample (ρ09-P1, Figure 4.7) contains a very

101

slightly (~×2) larger N^m_{Vtot} than the high-vesicularity transitional clast, ρ09-T6.

Additionally, the last sample erupted, ρ02, contains two transitional clasts; one N^m_{Vtot} is

~1.5 × lower (ρ02-T37, Figure 4.7) than the co-erupted fluidal clast (ρ02-F7), and the

other is ~1.5 × higher (ρ02-T40, Figure 4.7). Minute differences such as these are

explained by variable nucleation rates associated with a gradient in conduit, ascent rate

imparted by a velocity profile across the conduit with melt ascending more quickly along

the axis than along the conduit walls (Adams et al., 2006; Sable et al., 2006; Taddeucci et

al., 2004). This imparts textural diversity to the melt prior to fragmentation which, in the

case of Kīlauea Iki, is then overprinted by variable amounts of post-fragmentation

expansion.

4.5.2.6 Textural variability within clast types and among samples
The variability among sample suites and similar types of clasts in each sample lends

information associated with changes on a longer time scale of four to five days, during

episode 1 eruption and deposition.

      The lowest vesicle number density is from sample ρ17 (Table 1) which also

contains the maximum sized clasts (Figure 4.4b). The fluidal clast, ρ17-F6 (Figure 4.5d),

is unlike others in its clast category, containing coalescence textures (Figure 4.5e, f), an

outsized vesicle (~4-cm diameter), and lacking vesicles smaller than 20-μm diameter.

Based on comparisons with other samples, this specific fluidal clast does not represent

the high degree of nucleation achieved during the first episode of the Kīlauea Iki

eruption. Additionally, this clast has a slightly lower N^m_{Vtot} than contemporaneously

erupted pumice (ρ17-P1, Table 1). Because the eruption initiated as a dike, the deep

conduit maintained this geometry throughout eruption of episode 1. It is possible that slightly more mature and degassed ($\sim 2 \times$ lower N^m_{Vtot} than other fluidal clasts) magma was entrained from regions in the conduit surrounding the main eruptive pathway. This incorporated magma was not in residence long enough to outgas fully, as evident by the still relatively high N^m_{Vtot}, and was probably entrained as a result of increasing eruption intensity, resulting in a momentary peak in fountain height (~ 320 m) coinciding with deposition of the maximum-sized clasts (Figure 4.3b).

The last sample erupted, $\rho 02$, has a unique combination of characteristics. It has the most pumice clasts (Figure 4.4), a clear example of post-fragmentation expansion (Figure 4.5j-l), the only unimodal VVD ($\rho 02$-T40, Figure 4.7), the least volume of vesicles in bins >1mm (Figure 4.7), the smallest-diameter vesicle size peak (0.15 mm) across all clasts/samples (e.g., $\rho 02$-T37 & $\rho 02$-T40, Figure 4.7). The combination of these factors rule out both a high degree of coalescence and multiple nucleation events. Furthermore, it was erupted through the surface of the lava lake. Examination of archived photographs from the episode 1 eruption (USGS Hawaiian Volcano Observatory library) shows the fountain widened as a result of eruption through the lava lake surface. This resulted in a larger cross-sectional area and enhanced thermal insulation of the wider core, and could be the reason for the increased number of expanded pumice clasts.

4.6 Discussion

4.6.1 Rinds and clast interiors

The relationship between rind and interior of single clasts is pivotal to understanding the total diversity of microtextures in the episode 1 products, including those clasts without

preserved rinds. Rinds contain high proportions of small vesicles which we infer to be quenched rapidly after fragmentation with limited opportunity for bubble growth and coalescence. We infer that the rinds represent a closer approximation to melt textures on fragmentation than do the interiors of clasts. Given the small size of the clasts, it follows that textures preserved in the interior of rimmed clasts (1) developed after quenching of the rind and (2) evolved from more primitive vesicle textures closely resembling those of the associated rinds. We thus can use the quantitative contrasts between rinds and interiors to constrain which processes took place between fragmentation and final quenching of clast interiors. Vesiculation processes potentially contributing to the contrast are: continued nucleation, growth of bubbles by expansion or diffusion, coalescence of adjoining bubbles and bubble escape or collapse (Figure 4.10).

For each pair of rind and interior textures, the trend seen is for a slight increase in VND and increasing V_G/V_L (Figure 4.10). Based on the interpretation for clast ρ02-P2 above, the bubble population in the clast interiors evolved via a combination of coalescence and continued bubble growth after rinds of clasts were quenched to lock in more primitive vesicle populations. Development of interior textures occurred in less than ~8 seconds during transport within the lava fountain. One may speculate that this could also reflect considerable bubble growth and coalescence during magma ascent in the subsurface after nucleation and before fragmentation.

The data from table 4.1 and the graph in figure 4.10 can be used in simple calculations to approximate the components of clast expansion. By separating the amount of vertical vesicle volume increase and horizontal vesicle number density (VND)

decrease (Figure 4.10), the relative amounts of growth versus coalescence can be determined. Using vesicle volume and the vesicle number density (VND) for the two zones of clast ρ02-P2, the mean diameter for a single bubble within the rind is 47 μm (volume = 5.6×10^{-5} mm^3) and 118 μm within the interior (volume = 8.6×10^{-4} mm^3). Therefore, the mean vesicle diameter increases by a factor of 2.50 from the rind to the interior. For clast ρ02-P2 to achieve the same vesicle to melt ratio as the interior (location of 1 on Figure 4.10), the average volume of bubbles in the rind must increase from 5.6×10^{-5} mm^3 to 8.1×10^{-5} mm^3 (53 μm mean diameter), a change which would account for a factor of 1.13 of the total factor of 2.50 mean vesicle diameter increase. The amount of coalescence necessary to achieve the observed decrease in VND from rind to interior requires the mean bubble volume at location 1 to increase from 8.1×10^{-5} mm^3 to 8.6×10^{-4} mm^3. Therefore, coalescence accounts for a factor of 2.20 of the mean vesicle diameter increase from rind to interior, and mean vesicle volume increases by a factor of 9.7. Based on these calculations, after rind approximating bubbles expand via growth by a factor of 1.13, up to 10 bubbles must coalesce to achieve the mean volume of bubbles in the interior of the clast. The processes of growth and coalescence occur within ≤ 8 seconds of travel time in the fountain, therefore 7.7×10^{-4} mm s^{-1} is the maximum growth rate and 1.2 events s^{-1} is the minimum coalescence rate which increases the diameter at a rate of 8.1×10^{-3} mm s^{-1}.

For comparison purposes, the same calculations can be made to account for the degree of growth and coalescence for a clast such as ρ09-P1 originating with the vesicle volume and VND as the rind of ρ02-P2. The mean vesicle diameter increases by a factor

of 1.44 from 47 μm to 68 μm, which is significantly less than the increase from rind to

interior and is due to the 6 times higher VND in ρ09-P1 relative to the interior of ρ02-P2

(N^m_{Vtot}, Table 4.1). Growth only, from ρ02-P2R to location 2 on Figure 4.10, would

account for a factor of 1.17 mean diameter increase (from 47 to 55 μm) resulting in a

bubble with a volume of 8.9×10^{-5} mm^3. Coalescence only, from location 2 on Figure

4.10 to ρ09-P1, would account for a factor of 1.24 mean diameter increase (from 55 to 68

μm) resulting in a final bubble volume of 1.6×10^{-4} mm^3 which is a factor of 1.83 mean

vesicle volume increase. Therefore, growth occurs at a maximum rate of 9.9×10^{-4} mm

s^{-1} and coalescence occurs at a minimum rate of 0.22 events s^{-1} increasing diameter at a

rate of 1.5×10^{-3} mm s^{-1}. By comparing these two end members (r02-P2 I and r09-P1), it

is clear that coalescence plays the most significant role in post-fragmentation expansion.

4.6.2 Origin of fluidal and pumice textures in homogeneous clasts
The strong microtextural similarities between (1) the rinds of rimmed clasts and fluidal

clasts lacking rinds and (2) the interior of rimmed clasts and rind-free pumice are the

keys to interpreting the homogeneous clasts. Diversity in clast texture is a product of

location, trajectory, and residence time within the lava fountain. Figure 4.12 indicates the

inferred location of origin within the fountain for each of the clast types.

Fluidal clasts have high proportions of small vesicles that quenched rapidly after

fragmentation and have undergone limited bubble growth and coalescence with respect to

pumice. In order to maintain large populations of small vesicles (e.g., ρ20-F9, ρ11-F12,

ρ02-F7), the fluidal clasts, like clast rinds, must have quenched shortly after

fragmentation, without experiencing significant post-fragmentation expansion. To

accommodate rapid quenching after eruption, fluidal clasts must have been transported away from the thermally-insulated core of the fountain, traveling along the perimeter of the fountain (Figure 4.12).

Pumice clasts contain the greatest volume of large vesicles, with strong bimodal VVDs (Figure 4.7) that closely resemble the interiors of clasts with rinds (Figure 4.8a, b), and we infer that they went through a similar extended history of post-fragmentation expansion. We infer that pumiceous clasts preserving the most mature vesiculation textures must have traveled within the thermally-insulated core of the lava fountain (Figure 4.12b), either never forming rinds or losing the rinds as a result of breakup either in the jet or on-landing.

4.6.3 The significance and origin of transitional clasts

The transitional clasts can generally be considered to preserve textures that quenched at some point along the path of melt evolution between fluidal and pumice. Homogeneous transitional clasts (Figures 4.6a-e, 4.9) traveled a path through the fountain that limited post-fragmentation expansion to less than the full range of vesicle evolution (i.e., to pumice morphology). This suggests that radial position in the fountain played a key role in influencing cooling rate of the pyroclasts (Figure 4.12c). The quench time for a given pyroclast is a combination of clast size and trajectory with respect to the axis of the fountain. In this model, higher-vesicularity transitional clasts are located closer to the core whereas lower-vesicularity clasts are located closer to the margins. The heterogeneous transition clasts (Figure 4.6f-l) formed in a similar way to the more vesicular rind/interior pumiceous-type clasts (e.g., ρ02-P2, Figure 4.5j-n) where the

107

exterior of the clast quenched while the interior continued to expand, though to a lesser

degree than the rimmed pumice-approximating clasts. Expansion likely encompassed a

combination of growth and coalescence (Figure 4.10), as evident in the vesicle shapes

within the clast interior (Figure 4.6j-l).
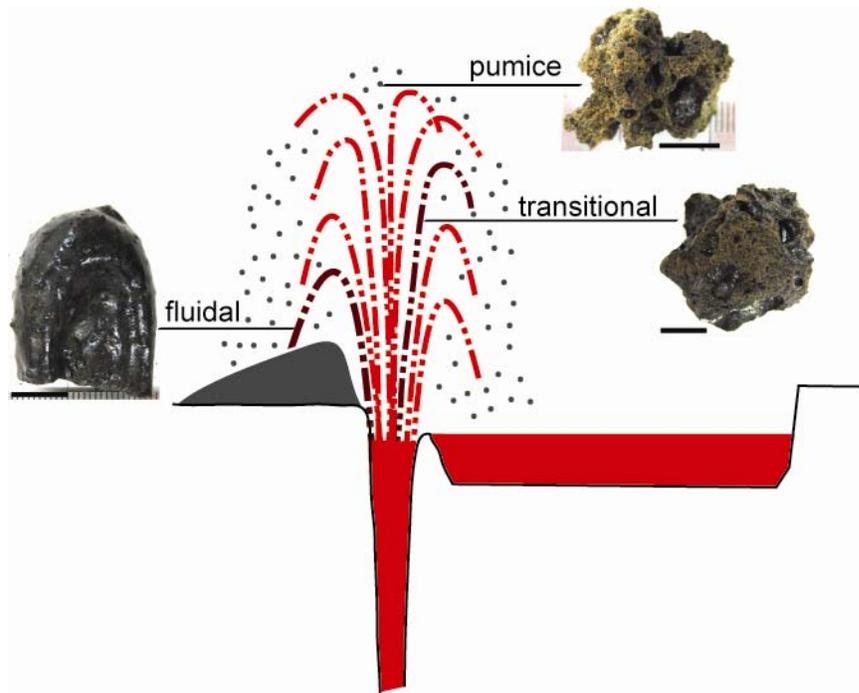
Figure 4.12 Clast type photographs and location of origin within the Kīlauea Iki
fountain.
Cartoon of Kīlauea Iki fountain and conduit with adjacent cone and lava lake. Clast types
and relative locations of quenching within the fountain are indicated by line adjacent to
clast. Scale bar below each clast equals 1 cm length. Cartoon is not to scale.

4.6.5 Model for fountaining behavior
Thermal gradients within the fountain drive textural diversity within Hawaiian tephra

(Figure 4.12). Clast interiors remain hottest and undergo minimal cooling before

sedimentation yielding clasts with mature vesicle populations. The clasts transported

principally in the fountain margins quench more rapidly and result in less-vesicular

fluidal textures (Figure 4.12) which preserve conditions within the conduit without a

108

significant overprint of post-fragmentation expansion. Hot gases streaming through the fountain glaze the outside of clasts (Thordarson et al., 1996) imparting a dark, glassy sheen on the exterior of clasts. Fluctuations in fountain height are not associated with bubbles seen in individual clasts but may reflect the passage of larger gas slugs, which are essentially mechanically decoupled and lost during the process of fragmentation (Parfitt, 2004). Richter et al. (1970) observed violent examples of this type of decoupled outgassing during episode 1, when gas bursts unaccompanied by liquid lava exploded from the vent area.

Figure 4.13 represents the progression for post-fragmentation expansion originating with fluidal-type melt and ending in pumice morphology. Initially fragmented melt (e.g., Figure 4.13a) contains abundant small, round bubbles (5–10-μm diameter) with thick glass walls and varying amounts of evenly distributed larger bubbles. As clast expansion continues, the proportion of small bubbles decreases due to growth and coalescence, resulting in larger amounts of bubbles between ~15–90-μm diameters (e.g., Figure 4.13b). Bubbles continue to coalesce and grow, via further fountain-insulated expansion, until bubbles >1 mm diameter form at the expense of smaller sizes (e.g., Figure 4.13c). Clasts traveling through the central, hottest portion of the fountain to its full height continue to expand through further coalescence and bubble relaxation prior to quenching, resulting in highly-vesicular pumice (Figure 4.13d).
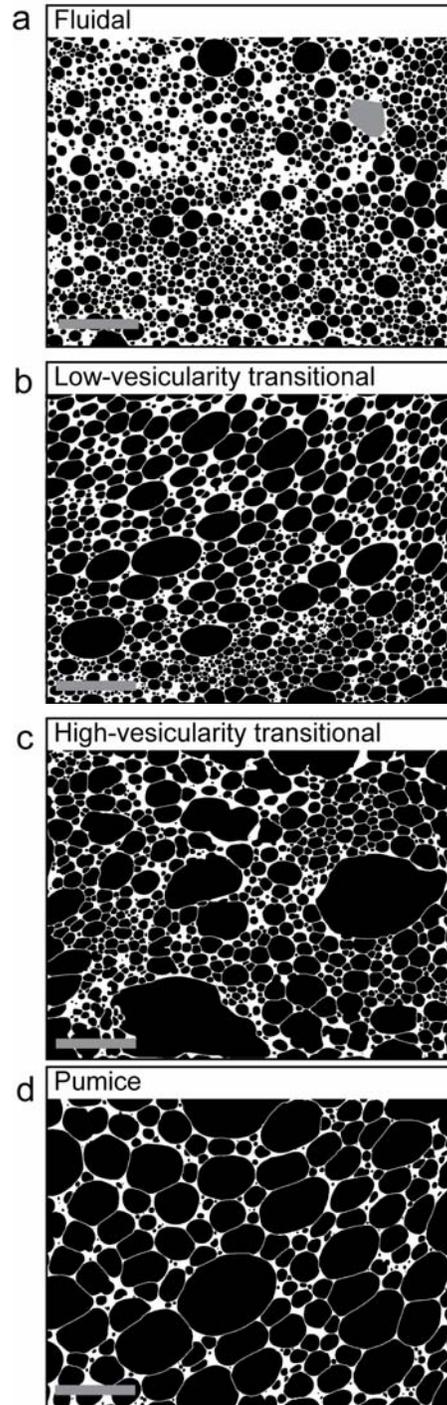
Figure 4.13 Collection of 25 × magnification grayscale SEM images representing fluidal to pumice transition within the fountain.

Fluidal (**a**), homogeneous-transitional (**b, c**), and pumice (**d**) clasts in order of increasing vesicularity. Full vesicle evolution for Hawaiian lava fountains at Kīlauea Iki originates with textures approximating **a** and mature to textures approximating **d**. Scale = 1.0 mm.

4.7 Conclusion

Our findings more clearly define the processes occurring in the fountain for a classic

powerful Hawaiian explosive eruption. There is a population of coupled bubbles which

is represented by the vesicle population we have studied. This gives validity, in one

sense, to the rise-speed dependent (RSD) model for Hawaiian eruptions (Head and

Wilson, 1987; Parfitt and Wilson, 1995; Parfitt and Wilson, 1999; Slezin, 2003; Wilson,

1980; Wilson and Head, 1981). It is known that exsolution depth scalses with bubble

size due to enhanced growth time by decompression (Parfitt, 2004). Under equilibrium

degassing conditions for Kīlauea Iki's reservoir-equilibrated magma, Gerlach (1986)

suggests a depth of <150 m for H_2O exsolution. This shallow level of degassing means

that magma must be transported to these depths by driving forces other than those

relating to upward momentum imparted by the near-surface exsolution of H_2O (Gerlach,

1986). This could have been achieved by upward forcing by a previously exsolved gas

phase (e.g., CO_2) or due to isostatic rise of magma as a result of excess reservoir pressure

imparted by the influx of new magma from 40-60 km depth (Eaton et al., 1987). This

raises a question as to what specific dynamics result in characteristic Hawaiian

fountaining and over what depth range and time scales these dynamics pertain.

The texture imparted to the 1959 magma by processes occurring in the subsurface

prior to fragmentation is overprinted by extended vesiculation within the lava fountain

after fragmentation. Radial thermal gradients in the fountain resulted in the formation of

pyroclasts with varying histories of vesicle growth. Clasts within the center of the

fountain remained thermally insulated, and bubbles continued to expand and coalesce

during transportation, resulting in the formation of pumice and the high-vesicularity

transitional clasts. Clasts traveling radially at the edges of the fountain quenched most

quickly, locking in higher abundances of small vesicle populations and producing fluidal

clasts.

CHAPTER 5
High fountaining Hawaiian eruptions:
episodes 15 and 16 of the 1959 Kīlauea Iki eruption

5.1 Introduction

5.1.1 High-fountaining Hawaiian eruptions

Hawaiian eruptions produce incandescent fountains of molten pyroclastic material that

can reach hundreds of meters in height. They occur at basaltic volcanoes such as Etna in

Italy (Alparone et al., 2003; Andronico et al., 2008; Bertagnini et al., 1990), Tolbachik in

Russia (Fedotov et al., 1980), and Kīlauea in Hawai'i (Heliker and Mattox, 2003; Richter

et al., 1970; Swanson et al., 1979). Lava fountaining eruptions typically begin as fissure-

fed discharges, increasing in intensity over several cycles, and reaching maximum

discharge and fountain height later in the eruption. Early activity in the 1983–1986 Pu'u

'Ō'ō eruption of Kīlauea, Hawai'i produced average fountain heights of ~170 m in the

first 23 episodes before eruption rates increased and fountains consistently reached >400

m high (470 m maximum) until the 39th episode (Heliker and Mattox, 2003). Similar

activity occurred in 1969 during the first 6 months of the Mauna Ulu eruption, Kīlauea,

Hawai'i. Relatively low initial fountaining episodes increased to 540 m height in the 9th

episode (Swanson et al., 1979). The eruption of Kīlauea Iki in 1959 also started from a

fissure and low fountaining before producing the highest fountain ever recorded for

Kīlauea (580 m) during the 15th of 17 episodes (Richter et al., 1970). Fedotov et al.

(1980) describe lava fountains during the 1975-76 Tolbachik eruption in Kamchatka,

Russia as 'pulsating ejections' at 60 to 80 per minute that reached between 50–300 m

height over the course of the eruption. Similar pulsations in discharge are seen in the

113

video footage of Kīlauea Iki. At Etna, lava fountain activity ranges from episodic (e.g.,

Alparone et al., 2003) to discrete, individual events (e.g., Andronico et al., 2008) with

fountain heights up to 800 m (Alparone et al., 2003). The commonality among individual

episodes of activity at all of these volcanoes is that lava fountaining ceased abruptly, with

little waning activity.
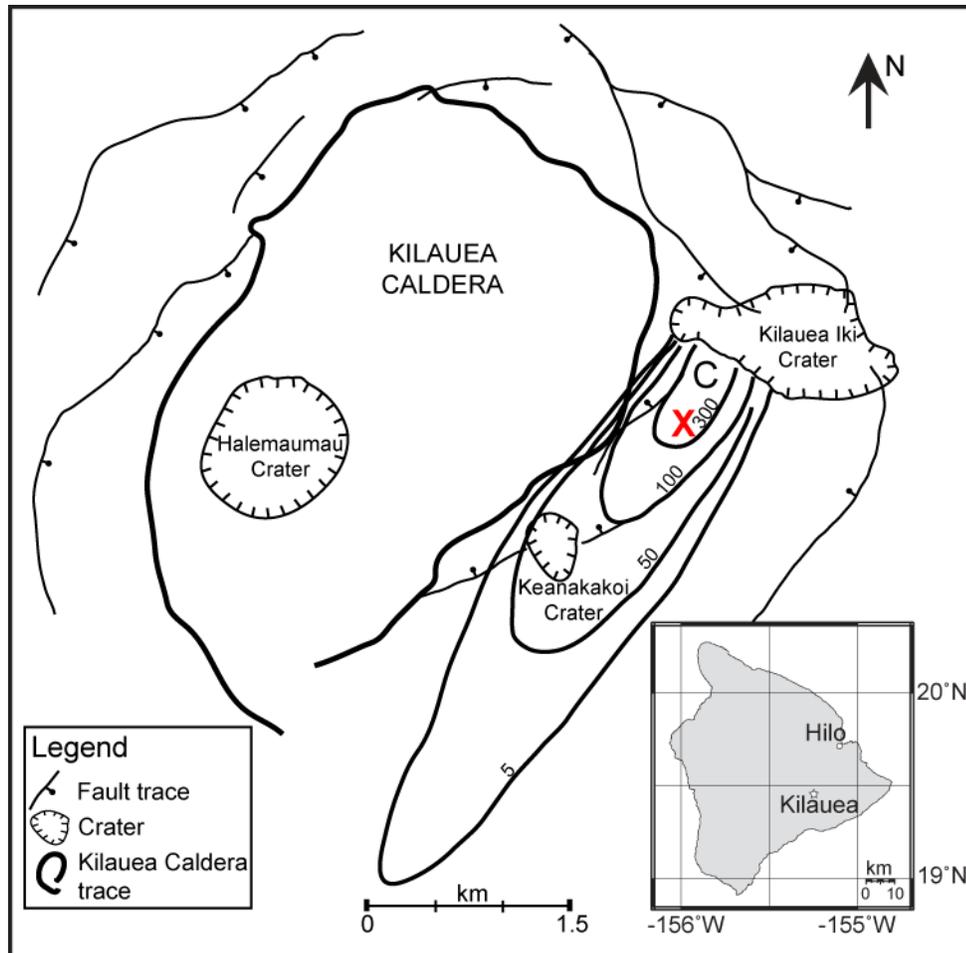
Figure 5.1 Location map of Kīlauea caldera and episode 15 and 16 study site.
(**a**) Kīlauea Caldera and Kīlauea Iki crater with tephra isopachs (thickness in cm, Houghton, unpublished data, 2008), Puʻu Puaʻi cone summit (C), and study site (X). (**b**) Island of Hawaiʻi with star marking location of Kīlauea.

5.1.2 Kīlauea Iki 1959 eruption

The 1959 eruption of Kilauea Iki (location shown in Figure 5.1) began on November 14th

and lasted 36 days (Figure 5.2). A steep-sided cone and a tephra blanket were deposited

southwest (downwind) of the main vent. Because the vent was on the wall of an existing

collapse crater, most of the erupted material formed a $\sim37\times10^6$ m^3 crater-filling lava lake.

Each episode was characterized by fountaining and lava effusion which led to filling of

the lake. Typically, low fountaining began each episode, and then the intensity increased

to produce a higher and more powerful fountain. Soon after the lake reached the level of

the vent, fountaining and effusion ceased, and lava immediately poured back down the

vent into the plumbing system to reach the summit storage region (Eaton et al., 1987).

Throughout the course of the eruption, episodes became shorter and typically more

closely spaced in time. The last two high-fountaining episodes, 15 and 16 (Figure 5.3),

were among the three highest during the entire eruption (Figure 5.2).
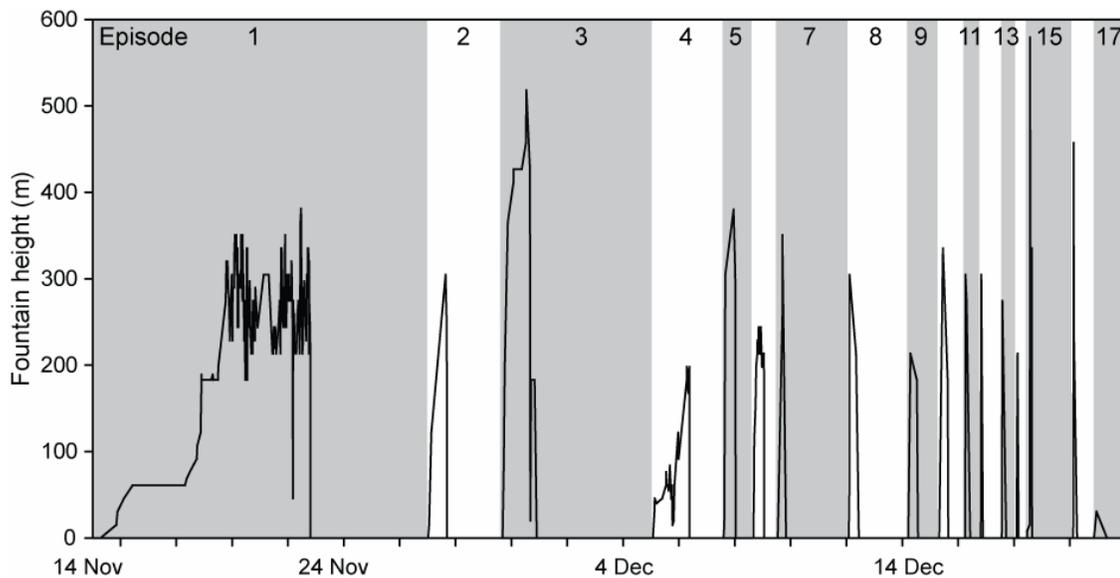
Figure 5.2 Kīlauea Iki eruption fountain height.
Numbers along the top and shaded stripes indicate individual episodes.

5.1.3 Purpose

This paper examines the vesiculation history of melt erupted in very high-fountaining Hawaiian eruptions. A secondary aim is to determine what effect, if any, melt draining back from the lava lake into the conduit had on fountain and eruptive behavior. This study also compares these last episodes with the opening episode of the Kīlauea Iki eruption (Chapter 4) in order to understand why some episodes reach exceptional fountaining heights when others do not, and what factors lead to the termination of Hawaiian fountaining episodes.

5.2 Background and previous work

5.2.1 Chronology of episodes 15 and 16

Richter et al. (1970) give a detailed account of the events of the 1959 eruption which is the basis for the following summary of episodes 15 and 16. The 15th episode lasted for slightly more than four hours, beginning at 11:10 AM December 17, 1959 with low fountaining (Figure 5.3a). During the first two hours, small lava fountains 8–15 m high erupted while a lava stream drained from the lake into the vent. Just before 2 PM, activity increased and within 12 minutes the fountain reached ~580 m (Figure 5.3b, c), the highest of the eruption. Activity was sustained at this peak for only a few minutes before fountain heights decreased to ~220 m, where they remained for ~30 minutes. Again, fountain heights surged to ~330 m for ~45 minutes. In the final minute of fountaining, lake lava began to drain into the vent. Hawaiian fountaining activity ceased rather abruptly at 3:32 PM while lava continued to pour into the vent from the lake. Drainback continued throughout the day on December 18th with decreasing flux, while draining, occasional non-eruptive splashing was observed at the vent.
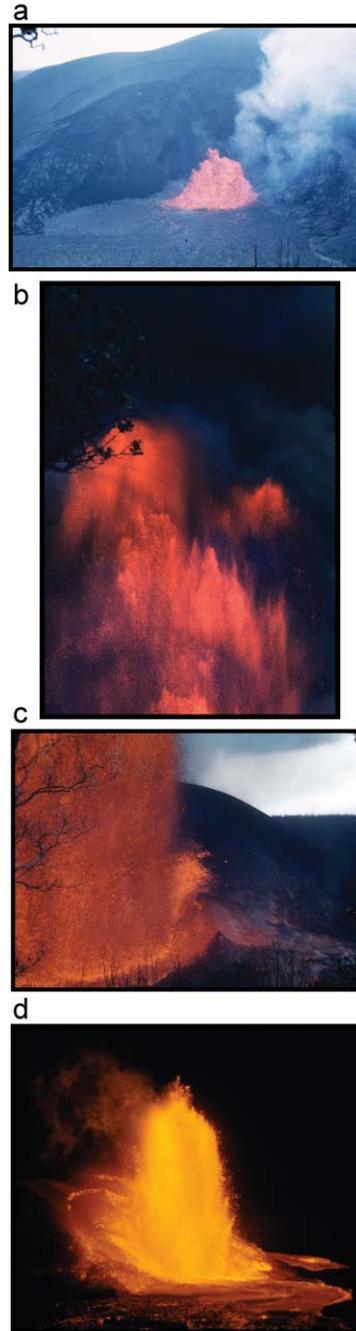
Figure 5.3 Photographs of Kīlauea Iki fountain during episodes 15 and 16.
Photos by J. Eaton from the HVO library archives. (**a**) Lava fountain at the start of episode 15, ~30 m high. (**b**) Top of episode 15 ~580-m-high fountain. (**c**) Lower portion of ~580-m-high fountain and cone with rheomorphic lava flows on cone flank. (**d**) Episode 16 ~240-m-high fountain.

On December 19th at 2:40 AM, after a 35 hour pause in fountaining activity, the 16th and last high-fountaining episode of the Kīlauea Iki eruption began. The 16th explosive phase started similarly to the 15th phase, but the early low spattering lasted only 20 minutes before the fountain height increased over 25 minutes to a height of ~460 m. Although lava fountains reached and maintained this great height for several minutes, lava also surged into the lake from the base of the fountain. The remaining 170 minutes of explosive activity were limited to Hawaiian fountains ~240 m high (Figure 5.3d). At 6:16 AM on the same day, fountaining ceased and drainback of lake lava into the vent began immediately as a ~60 meter wide flow encircling the vent.

5.2.2 Significance of episodes 15 and 16
These two episodes produced the last high fountains of the 1959 Kīlauea Iki eruption. Unlike the first episode of the eruption (detailed in Chapter 4), initial explosive fountaining needed to clear the conduit of any relatively degassed lava that drained back into the vent during the preceding episodes. Episode 15 produced the highest fountain at ~580 m (Figure 5.3b) and, of those affected by drainback, this was the episode preceded by the smallest volume of drainback lava (1.0 million m^3), which slowed from the lake into the vent over 7 hours 8 minutes. Episode 16 produced a ~460-m-high fountain and was preceded by 3.2 million m^3 of drainback lava over 26 hours after the end of episode 15. The coupling of high-fountaining activity and eruption of variable quantities of recycled, drained-back lava make the later episodes of the Kīlauea Iki eruption, and especially the occurrence of these short-lived high-fountain producing episodes, an intriguing case study for mechanisms driving Hawaiian fountaining eruptions.

118
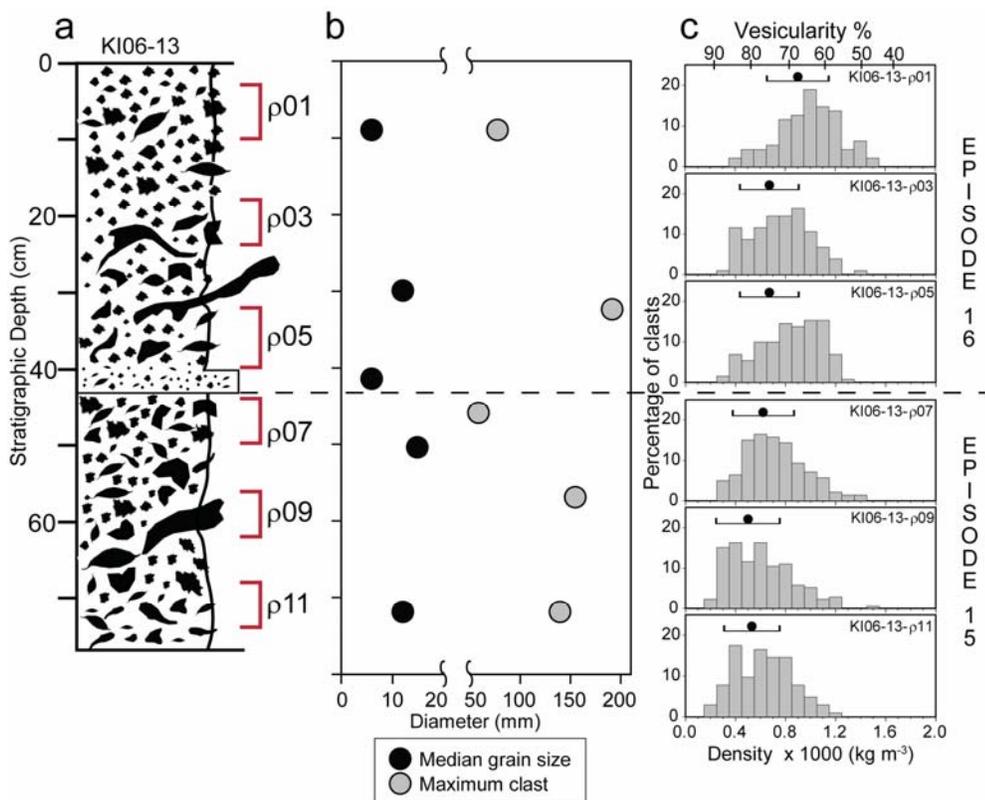
Figure 5.4 Kīlauea Iki eruption episode 15 and 16 stratigraphy, grain size, and bulk density.

(**a**) Stratigraphy with sample locations and (**b**) median grain size and maximum clast diameter. (**c**) Density distributions for samples taken from locations labeled in stratigraphy, dots above histograms indicate mean density, bars equal 1 standard deviation. Maximum clast diameters are calculated from the average of three axes for each of 5 clasts.

5.3 Techniques

All methodologies associated with sample collection and analyses are consistent with the

study of the first episode of the Kīlauea Iki eruption (Chapter 4). Samples of episodes 15

and 16 tephra were collected at ~5 cm intervals through the entire ~80 cm deposit at the

reference site (Figure 5.4a). Samples were field-sieved to select typically 100 clasts in

the 16-32 mm size fraction, then dried in an oven at 112º C for 24 hours to remove water.

Slight changes in sampling frequency and clast categorization were incorporated as

necessary. Additionally, chemical analysis of the glass component was conducted

following the discovery of heterogeneous zones of contrasting vesiculation and color within single clasts. Samples $\rho01$, $\rho03$, $\rho05$, $\rho07$ and $\rho09$ (Figure 5.4) were chosen for quantitative analysis of vesicle and crystal populations. This selection includes samples with maximum-sized clasts and those deposited at the end of each episode. Polished thin sections were made of clasts from the peak and extremes of the density distributions for these samples, to ensure capture and quantification of the full vesicularity range.

5.3.1 Clast morphologies
Componentry of the juvenile clasts was conducted in the laboratory and six morphological classes defined, but not every type is found in every sample (Figure 5.5a). *Pumice*, *fluidal* and *transitional* textures (Figure 5.5b,d and c) are as defined for the 1959 episode 1 tephra (Chapter 4). Clasts labeled T_O are transitional and contain domains of reddish-colored oxidized material (Figure 5.5e). Clasts labeled T_B are transitional clasts with a bread-crusted exterior surface. Very large spatter bombs (i.e., the maximum-sized clasts) always fall into this category and are typically either cow-dung or ribbon bombs (Figure 5.5f, g). These breadcrust bombs have interiors with vesicles up to 10 cm diameter.
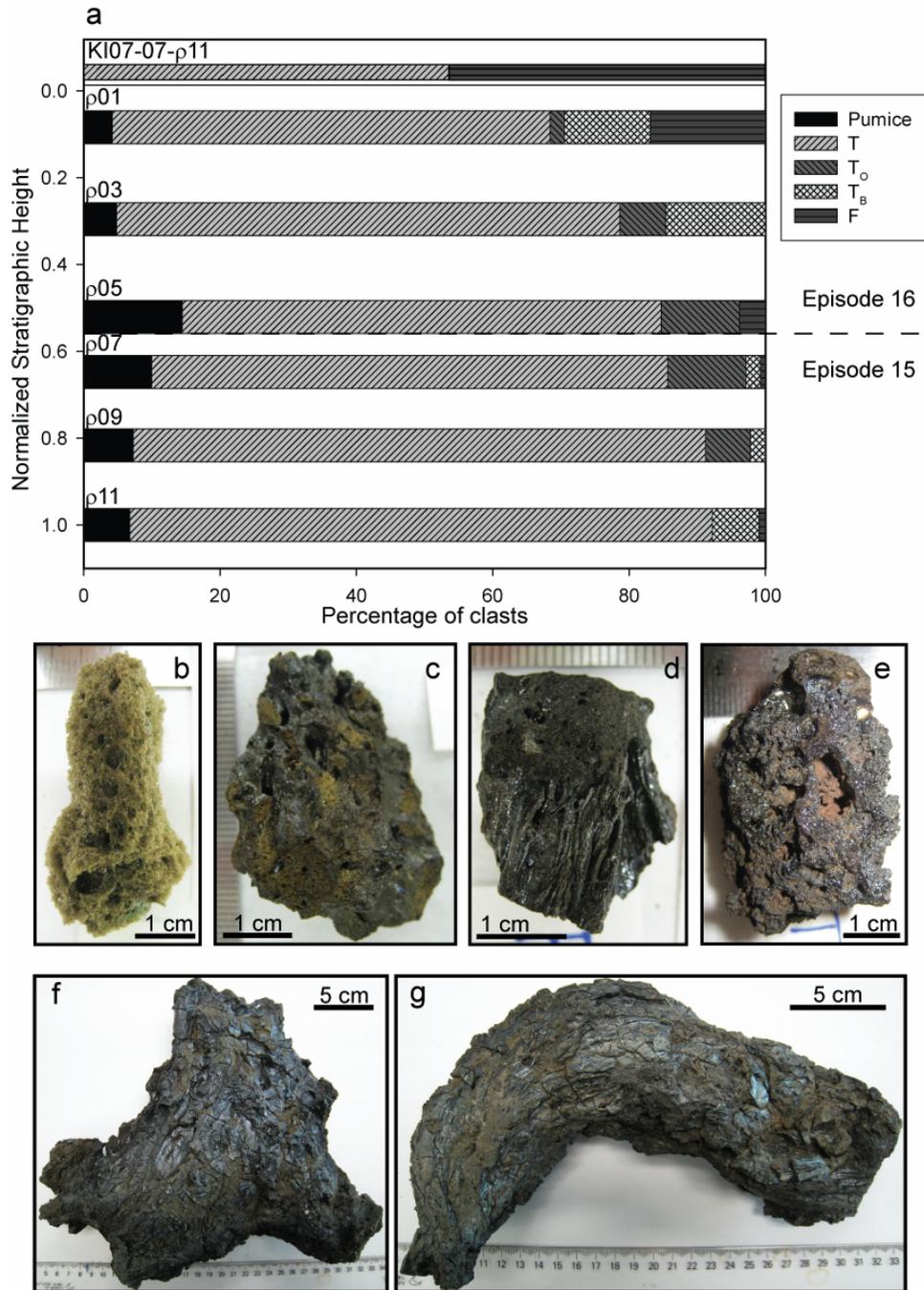
Figure 5.5 Componentry and clast photographs for episode 15 and 16 samples.

(**a**) Juvenile clast componentry for episodes 15 and 16 Kīlauea Iki tephra; clasts correspond to labeled stratigraphic position on Figure 5.4. Top bar is from episode 1 to assist comparison between eruptive episodes. Clast-types with 1 cm bar for scale: (**b**) pumice, (**c**) transitional, (**d**) fluidal, (**e**) oxidixed transitional, T_O, (**f & g**) transitional breadcrust bombs, T_B. Componentry data are derived from processing samples of at least 100 clasts of diameter 16-32 mm.

5.3.2 Electron microprobe analysis

To quantify and compare major-element chemistry within individual zones or domains in heterogeneous clasts (Figure 5.6), electron microprobe analysis was conducted with the 5 spectrometer JEOL JXA-8500F at the University of Hawaiʻi at Mānoa. Wavelength dispersive mode was used at 15 kV and 10 nA with a 10μm defocused beam to ensure minimal Na loss. Total counting times for each element were: Na=20 sec, SI=30 sec, Ti=20 sec, Al=30 sec, Fe=15 sec, Mn=20 sec, Mg=40 sec, Ca=30 sec, K=30 sec, P=30 sec, S=30 sec. Backgrounds were measured on both sides of the peak, each at half the counting time of the peak.
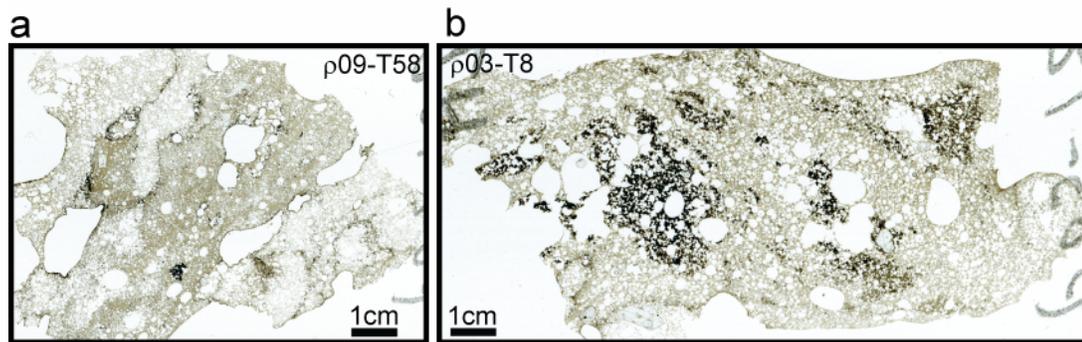
Figure 5.6 Thin section scans for heterogeneous clasts.
(**a**) Zones of variable vesicularity and (**b**) dark, microlite-rich zones within light, microlite-free glass.

5.4 Results

5.4.1 Deposit Characteristics

5.4.1.1 Stratigraphy

Kīlauea Iki tephra stratigraphy has been observed in a series of pits that extend up to 5 km downwind of the Puʻu Puaʻi cone (Figure 5.1). Existing collapse pits provide sections through the upper ~1–2 m of the deposit and expose stratigraphy that is

reconcilable at multiple locations. The tephra stratigraphy exposed in the upper pit walls must be associated with the last high-fountaining episodes (Figure 5.2).

Figure 5.4 includes the stratigraphy with sample locations, grain size and maximum clast data, and selected density distributions for the upper ~80 cm of a pit 685 m from the vent (Figure 5.1). The pit was chosen because it is located along the dispersal axis for episodes 15 and 16 fountaining and because tephra in this location is relatively proximal and yet not welded (as is the case within ~450 m of the vent along the same axis). Within the upper ~80 cm of tephra (Figure 5.4a), two distinct normally-graded sequences are separated by a ~3-4 cm markedly finer-grained achnelith-rich (Walker and Croasdale, 1972) layer with a sharp lower contact and slightly gradational upper contact. The uppermost 40 cm contains fine ash and grades downward from predominantly 3-mm- to 4-cm-diameter golden- to light-brown, highly-vesicular clasts to greater proportions of black-shiny clasts and vesicular spatter 5 mm–8 cm in diameter. Between 20 and 40 cm from the top, spatter clasts reach up to a maximum of 25 cm in diameter and appear flattened or elongate, whereas smaller spatter clasts are equant. The fine-grained achnelith-rich layer at 40 to 43 cm (Figure 5.4a) contains clasts between 3 mm–2 cm diameter but lacks fine ash. The second graded sequence extends from 43 cm from the top to ~78 cm and is similar to the one above the achnelith zone, except that the largest spatter clasts in the lower portion of the sequence are closer to 20 cm diameter. The lower contact of this graded sequence is marked by disappearance of large spatter and appearance of a zone dominated by pumice. Based on investigations in multiple pits, the similarity of the two sequences, and the achnelith parting between them, we infer the

upper graded sequence, including the achnelith-rich layer, was deposited during episode 16 and the lower graded sequence is the product of episode 15 fountaining (Figure 5.4).

5.4.1.2 Grain size
Bulk grain size samples were collected at five stratigraphic heights, sieved, and measured prior to this study. The median grain size (Figure 5.4b) of samples for the uppermost ~78 cm ranges between -2.6 and -3.9 ϕ (6–15 mm). At five stratigraphic levels, the 3 dimensions of the five largest clasts were measured and averaged to yield the mean-maximum clast size (Figure 5.4b). Maximum clast diameters within the upper portion of each normally graded sequence are between ~60 and 80 mm, whereas the lower portion of each sequence contains much larger clasts between ~150 and 200 mm diameter.

5.4.2 Density, bulk vesicularity and componentry
Density measurements of clasts from episodes 15 and 16 span a broad range and vary by 1000-1200 kg m^{-3} for every sample (Figure 5.4c). The least dense clasts, with highest vesicularity, are pumice, and the most dense clasts are T_O (oxidized transitional) or fluidal. Transitional clasts span an overlapping and intermediate range of vesicularity from ~90% to ~55%; in samples $\rho03$, $\rho05$ and $\rho09$, there are few fluidal clasts, and transitional clasts are the least-vesicular/densest clast used for quantitative micro-textural analysis.

Density distributions for episode 15 samples ($\rho11$, $\rho09$ and $\rho07$, Figure 5.3c) are all similar, with broad peaks and mean densities of 500-620 kg m^{-3} (82-78% vesicularity). Sample $\rho07$, erupted at the end of episode 15, has the widest diversity of clast types (Figure 5.5a) as well as the highest mean density (Figure 5.4c).

Episode 16 samples (ρ05, ρ03 and ρ01, Figure 5.4c) have distributions skewed

toward higher densities than in episode 15. The range of mean densities 670-900 kg m^{-3}

corresponds to 76-68 % vesicularity. The densest clasts in this study are in sample ρ01,

which was deposited during the final high-fountaining of the Kīlauea Iki eruption. It is

the only sample from either episode containing all six clast morphologies and has the

greatest amount of fluidal clasts (Figure 5.4a).

5.4.3 Qualitative microtexture observations

There are no significant qualitative microtextural differences between episode 15 (Figure

5.7) and episode 16 (Figure 5.8) clasts. Vesicles are round and variably sized between 5

µm and a few centimeters diameter, and the largest vesicles are the most irregularly

shaped (e.g., Figures 5.7d, 5.8d). Olivine phenocrysts are present in all except the most

vesicular clasts and their abundance seems unrelated to vesicle number or size

distribution (Figures 5.7, 5.8). On fresh surfaces, moderately- to highly-vesicular clasts

have a thin vesicle-poor rim (Figures 5.7d, 5.8g). Homogeneous clasts contain even

distributions of vesicles with a diversity of sizes (Figures 5.7a, 5.8a) separated by glass

walls that thin with increasing vesicularity (e.g., Figures 5.7 and 5.8, b to e to h

transition). The least vesicular clasts (Figures 5.7a-c, 5.8a-c) contain round vesicles

separated by relatively thick walls. Highest-vesicularity, pumice clasts (Figure 5.7g-i,

5.8g-i) are foams, with single-micron-thick vesicle walls that flatten against nearest

neighbors (e.g., Mangan and Cashman, 1996).

125
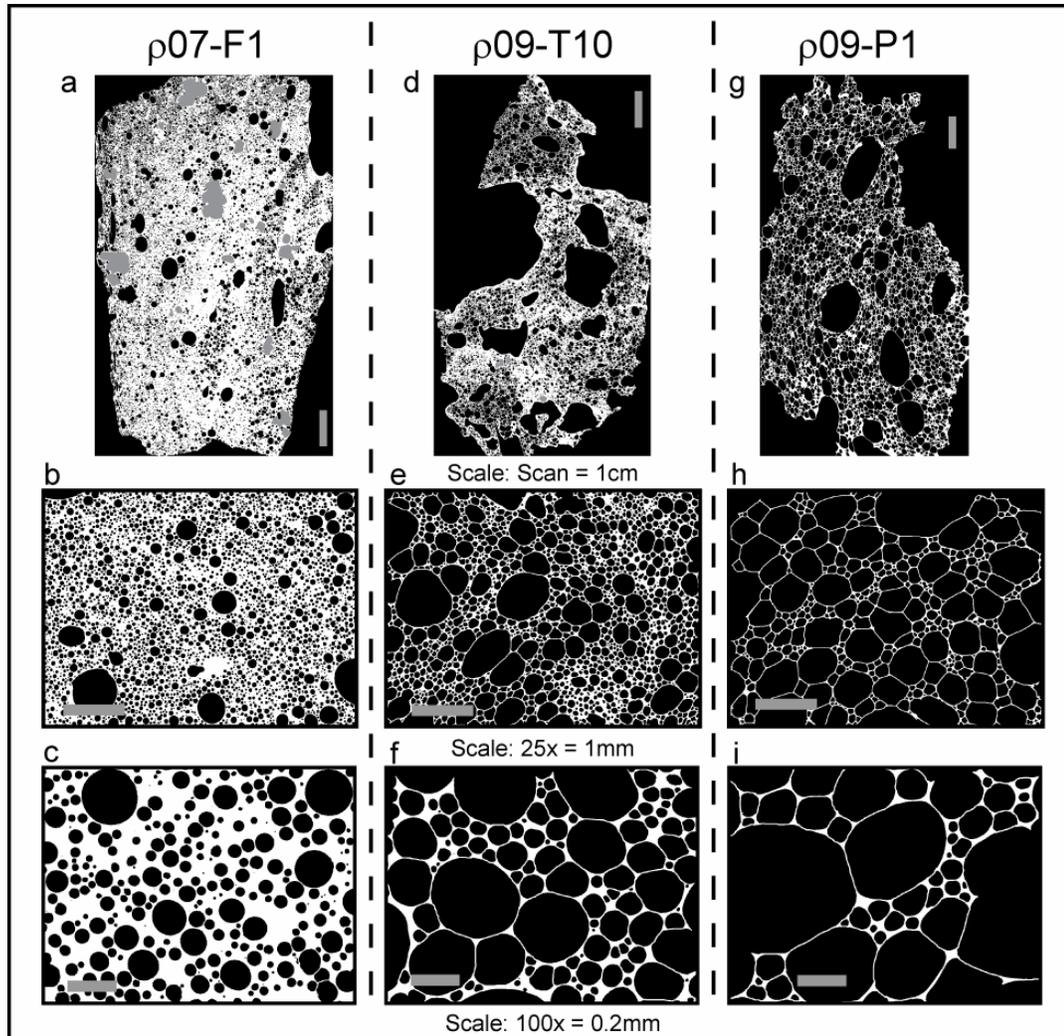
Figure 5.7 Grayscale processed images for episode 15 clasts.
(**a – c**) Low-vesicularity, fluidal clast, (**d – f**) intermediate-vesicularity transitional clast, and (**g – i**) high-vesicularity, pumice clast. Thin section scans in the top row, SEM 25×
magnification images in second row, SEM 100× magnification images in third row.
Vesicles are black, glass is white and crystals are gray.

Heterogeneous clasts come in two varieties characterized by: 1) mingled more-

vesicular (*MV*) and less-vesicular (*LV*) zones (Figure 5.6a) and 2) sharply-delineated,

opaque microlite-rich (*MLR*) zones within golden, translucent microlite-free (*MLF*) glass

(Figure 5.6b). In clasts with zones of variable vesiculation (Figure 5.6a), the MV regions

have thinner walls and more amoeboid vesicles. LV regions appear to contain larger

126

numbers of smaller, round vesicles. In MLF versus MLR zones, vesicle abundance and size is often approximately the same; within the microlite-rich zones, however, there are more amoeboid vesicles. Also within MLR regions, vesicle walls are less smooth and appear slightly irregular (Figure 5.8f) in comparison to smooth, round vesicle walls in MLF glass (Figures 5.7c, 5.8c).
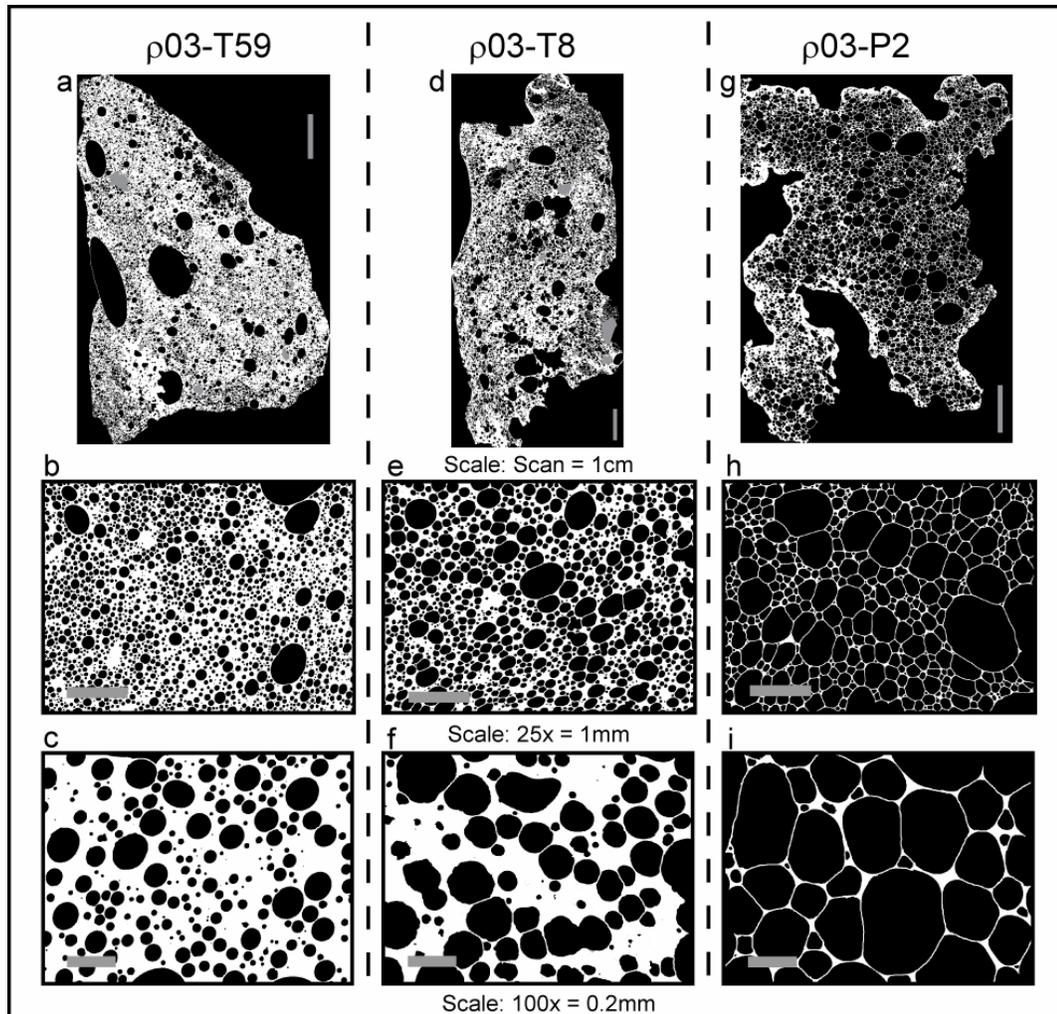
Figure 5.8 Grayscale processed images for episode 16 clasts.
(**a – c**) Low-vesicularity, transitional clast, (**d – f**) intermediate-vesicularity transitional clast, and (**g – i**) high-vesicularity, golden-pumice clast. Thin section scans in the top row, SEM 25× magnification images in second row, SEM 100× magnification images in third row. Vesicles are black, glass is white and crystals are gray.

127

There are two distinct types of microlite textures, thin stringers and intergrown, fasciculate patches. Stringers are elongate 30–100-μm-wide bands of pyroxene microlites that appear most commonly in transitional to fluidal clasts. The edges are distinct and defined by prismatic terminations of radiating spherulites or dendrites that originate at the centerline of the stringer. They sometimes separate MV and LV zones, but are also located within uniformly-vesicular clasts. MLR zones contain clusters of microlites with fasciculate texture comprised of intergrown plagioclase and pyroxene crystals that range in length from 0.1 to 0.4 mm. The MLR regions are ~1 and 15 mm in diameter, and the crystal morphology at the boundary of MLF glass is similar to the point-centered radiating pyroxene dendrites of the stringers. At the MLR zone boundaries there are occasionally rounded lobes of slightly darker golden glass that protrude into the adjacent, lighter-golden MLF zone.

5.4.4 Quantitative microtexture observations

Quantitative microtextural analysis of episodes 15 and 16 tephra adds to the study of Kīlauea Iki's opening episode (Chapter 4) and gives further insight into processes occurring in Hawaiian eruptions. Vesicle volume distributions (VVDs) for homogeneous clasts, included in Figure 5.9, are organized according to trends in vesicle to melt (liquid) ratio (V_G/V_L; after (Gardner et al., 1996) and changes in the number density (*VND*), i.e., number of vesicles per unit volume of melt, N^m_{Vtot} (Figure 5.10, Table 5.1). Clasts with vesicularity <75% contain significant numbers of vesicles with equivalent diameter smaller than 10 μm, which account for only minor volume fractions and do not appear on VVDs.

128

VVDs for all clasts are bi- to tri-modal. Low V_G/V_L clasts ρ03-T59, ρ07-F1 and

ρ09-T42 have the smallest modal diameters (0.1 mm, left column in Figure 5.9) and also

contain the largest N^m_{Vtot} (Figure 5.10). In general, as vesicularity and therefore V_G/V_L

increase, the smallest-diameter volume peak coarsens in size and the second mode near

1.0 mm increases in volume. Additionally, increasing vesicularity results in a dominant

second mode between 1.0 and 2.5 mm (right column P-clasts, Figure 5.9).

Episode 15 clasts have generally higher vesicle number densities (Table 5.1) and

span a wider vesicle size range (Figure 5.9) than do episode 16 clasts. For this highest-

fountaining episode in 1959, number densities (N_{Vtot}) are 2.4×10^5 cm^{-3} to 6.4×10^6 cm^{-3}

with melt referenced values (N^m_{Vtot}) between 3.9×10^6 cm^{-3} and 1.8×10^7 cm^{-3}. In

comparison to other basaltic explosive volcanism (Table 5.1), vesicle number densities

for episode 15 are higher than those of the 1983-1986 Puʻu ʻOʻo tephra (Mangan and

Cashman, 1996), 2002 Stromboli lapilli (Lautze and Houghton, 2007), and recent

Strombolian and Hawaiian products from Etna (Polacci et al., 2009; Polacci et al., 2006).

There is partial overlap in number density with 2004 products from Villarrica volcano

(Gurioli et al., 2008) and the basaltic-plinian eruption of Etna in 122 BC (Sable et al.,

2006). The ranges of N^m_{Vtot} for episodes 15 and 16 and episode 1 are nearly the same,

though episode 15 contains more clasts with number densities ~10^7 cm^{-3}.

Table 5.1. Vesicularity data for episode 15 and 16 clasts.

Study	Density x1000 (kg/m^{-3})	Density-derived ves %[a]	crystal correct ves %[b]	N_{Atot}[c] (cm^{-2})	N_{Vtot}[d] (cm^{-3})	N^{m}_{Vtot}[e] (no cm^{-3})
Kīlauea						
Kīlauea Iki Episode 15						
ρ09-P1	0.17	93.9	93.9	2.1E+03	2.4E+05	3.9E+06
ρ09-T10	0.33	88.2	88.8	6.7E+03	1.2E+06	1.1E+07
ρ07-T11	0.62	77.9	82.0	1.0E+04	2.0E+06	1.1E+07
ρ09-T9	0.53	81.1	81.1	1.3E+04	2.7E+06	1.4E+07
ρ07-F1	1.13	59.6	64.6	1.9E+04	6.4E+06	1.8E+07
ρ09-T42	1.11	60.4	62.5	1.5E+04	5.6E+06	1.5E+07
Kīlauea Iki Episode 16						
ρ05-P11	0.29	89.6	90.8	3.3E+03	5.6E+05	6.2E+06
ρ03-P2	0.27	90.4	90.4	2.7E+03	4.3E+05	4.5E+06
ρ01-P1	0.36	87.1	88.3	3.0E+03	8.1E+05	6.9E+06
ρ03-T20	0.32	88.6	89.2	4.0E+03	7.3E+05	6.7E+06
ρ05-T14	0.75	73.2	76.2	7.7E+03	2.0E+06	8.5E+06
ρ01-T19	0.94	66.4	71.2	9.6E+03	2.0E+06	6.9E+06
ρ03-T8	0.85	69.6	70.6	6.3E+03	2.0E+06	7.0E+06
ρ03-T59	1.15	58.9	59.5	1.5E+04	5.9E+06	1.5E+07
ρ05-T50	1.21	56.8	58.0	1.1E+04	3.9E+06	9.2E+06
Kīlauea Iki epi 1 Chapter 4	0.34-1.5	50.0-87.9	53.8-87.9	2.6E+03-1.2E+04	6.3E+05-6.8E+06	3.8E+06-1.2E+07
Pu'u 'O'o Mangan and Cashman 1996		77-97			1.1E+02-1.8E+07	
Stromboli Lautze and Houghton 2007				7.1E+02-6.9E+03	9.3E+04-1.3E+06	1.9E+05-3.4E+06
Villarrica Gurioli et al., 2008	0.23-1.4	47.8-88.8		9.3E+02-8.5E+03	6.4E+04-2.1E+06	7.4E+05-1.4E+07
Etna						
Hawaiian Polacci et al., 2009		52.0-81.0		3.0-9.0E+02		
Strombolian Polacci et al., 2009		52.0-73.2		1.0-4.0E+02		
Basaltic Plinian Sable et al., 2006						2.6E+06-6.1E+07

[a]Vesicularity calculated from density and DRE of 2800 kg m^{-3} computed using formula of (Bottinga and Weill, 1970) based on known composition of episode 1 Kīlauea Iki lava (Richter et al., 1970).
[b]Vesicularity calculated from density of clast minus percent density of olivine. Percent of olivine determined by amount of clast containing olivine in thin section.
[c]N_{Atot} values are the sum of bins from 0.005 to 40 mm.
[d]N_{Vtot} is the number of vesicles per unit volume of clast matrix, phenocrysts subtracted.
[e]N^{m}_{Vtot} is referenced to melt only, calculation based on phenocryst corrected (e) or N_{Vtot}-derived (f) vesicularity.
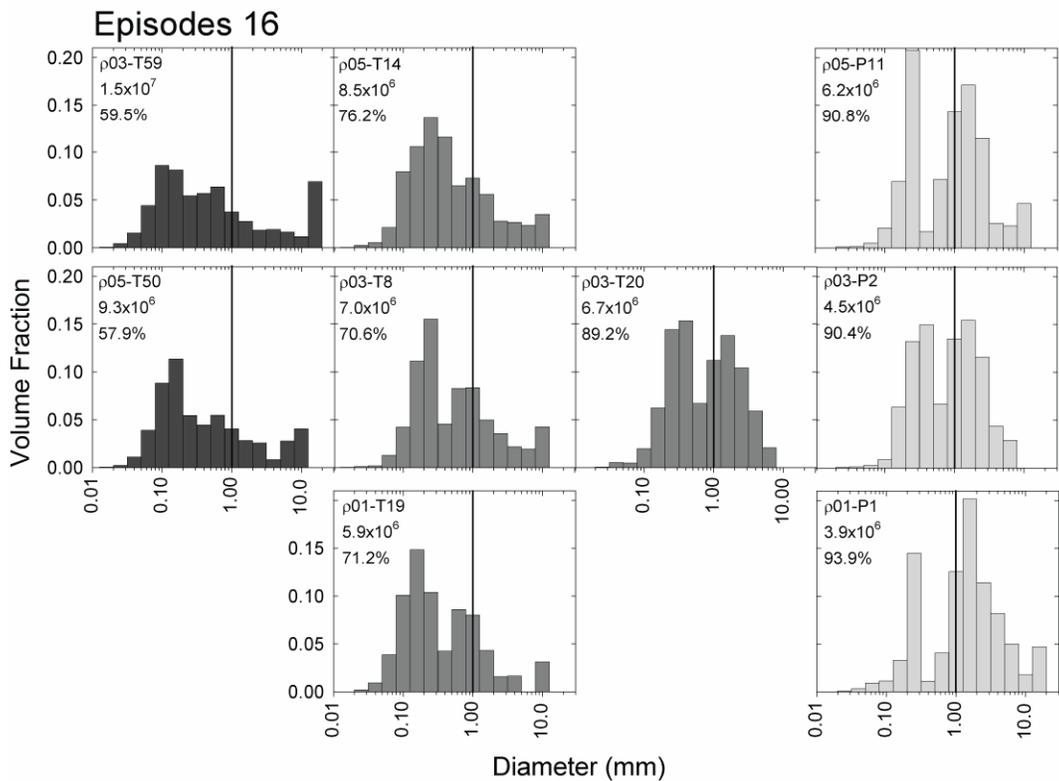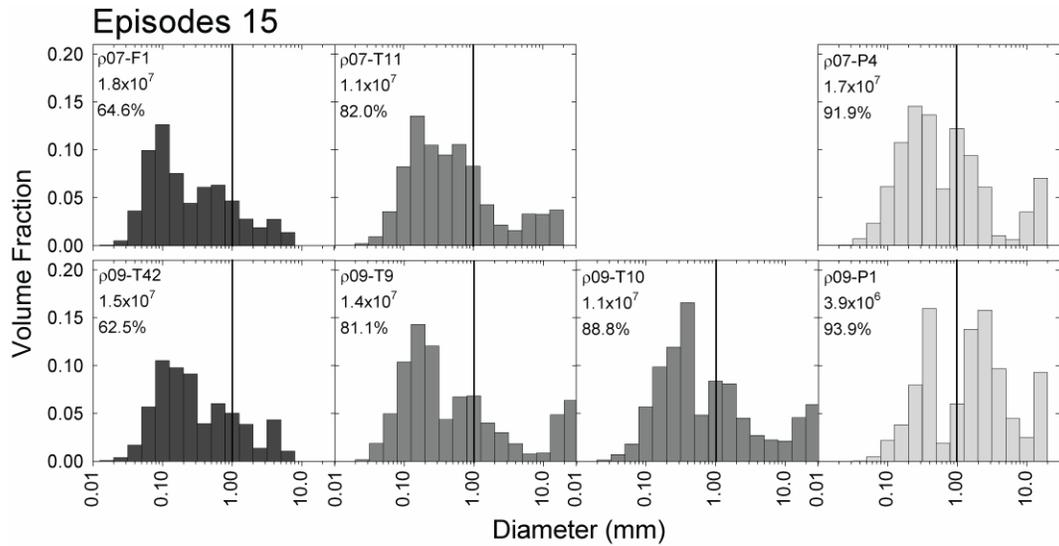
Figure 5.9 Vesicle volume distributions for episode 15 and 16 clasts.

Distributions of volume fraction of vesicles within a specific size range (VVD) arranged according to vesicle number density and vesicle to melt ratio (see also Figure 5.10). Sample number, vesicularity, and vesicle number density per cubic centimeter are included with each histogram (also found in Table 5.1). Dark- to light-gray shading corresponds with vesicularity grouping. Vertical lines are drawn at 1.0 mm vesicle diameter to assist comparison.

5.4.5 Glass chemistry

Chemical analyses of glass in MLR versus MLF and MV versus LV zones (Figure 5.6) of

tephra from the late high-fountaining episodes of Kīlauea Iki are included in Table 5.2.

Relative to the MLF zones, the matrix glass within MLR regions is slightly higher in

TiO_2 and FeO and slightly less MgO and CaO. MV and LV glasses are chemically

identical.
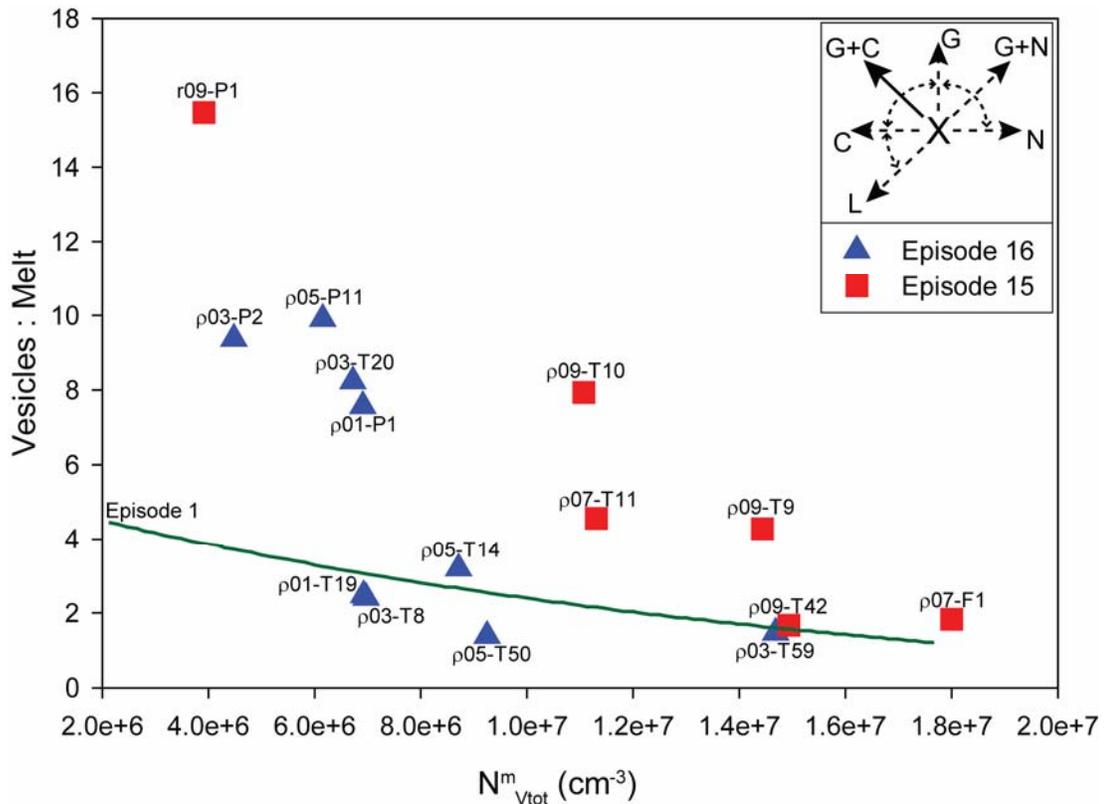
Figure 5.10 Volume ratio of vesicles to melt versus vesicle number density for episode
15 and 16 clasts.

Data points are labels of clast name and green line represents trend of data for episode 1
clasts. Inset graph depicts vesiculation trends originating at X proceeding via growth
only (G), growth plus nucleation (G+N), growth plus coalescence (G+C), coalescence
only (C), and vesicle loss (L). Our study indicates low V_G/V_L ratio and high N^m_{Vtot} clasts
most closely preserve the textures of melt at the time of fragmentation, with further
vesiculation processes proceeding in the fountain.

Table 5.2. Chemical analysis of glass matrix in heterogeneous zones.

Zone		SiO_2	TiO_2	Al_2O_3	FeO	MnO	MgO	CaO	Na_2O	K_2O	P_2O_5	Tot.
MV	Avg.	49.33	2.75	13.39	11.18	0.16	7.15	11.47	2.20	0.56	0.28	98.48
N=11	Std. dev.	0.26	0.09	0.07	0.13	0.03	0.07	0.07	0.07	0.02	0.02	0.84
LV	Avg.	49.26	2.76	13.39	11.25	0.17	7.14	11.52	2.26	0.56	0.28	98.59
N=14	Std. dev.	0.33	0.09	0.09	0.12	0.02	0.08	0.08	0.03	0.02	0.02	0.88
ML free	Avg.	49.69	2.73	13.44	11.12	0.17	7.04	11.43	2.16	0.56	0.28	98.59
N=12	Std. dev.	0.34	0.10	0.14	0.20	0.02	0.31	0.07	0.11	0.02	0.04	1.34
ML rich	Avg.	49.76	3.00	13.45	12.04	0.17	6.28	10.90	2.30	0.68	0.32	98.91
N=10	-Evo.[a]	49.82	2.89	12.94	11.46	0.16	7.69	12.08	2.09	0.54	0.28	99.95
	+Evo.[a]	49.56	3.00	13.64	12.19	0.16	5.89	10.63	2.25	0.67	0.33	98.31

[a]Less (-) evolved (Evo.) and more (+) evolved analyses span the full array of chemical data. MV, LV and ML free were averaged because there is no fractional crystallization trend.

5.5 Interpretation

5.5.1 Interpretation of macroscopic data

Deposits from episodes 15 and 16 have similar stratigraphy (Figure 5.4a) and both are dominated by transitional material (Figure 5.5a), but variations arise in concentration of other clast types (Figure 5.5a) and in the density distributions of clasts within samples (Figure 5.4c). In episodes 15 and 16, the transitional material with an oxidized core (T_O, Figure 5.5e) is likely to represent material from the cone that was seen to tumble back into the vent to mingle with melt and be subsequently re-erupted. After being erupted, some transitional clasts (T_B, Figure 5.5f, g) quenched on the exterior while the interior of the clast continued to expand, imparting a cracked, breadcrust surface to the clasts. Some degree of expansion probably occurred within the fountain but must have also occurred after external surface quenching. This interior expansion, therefore, may have taken place either after clast exteriors were quenched in flight or, for the largest clasts, after

133

deposition of clasts. Bomb-sized clasts are significantly larger than lapilli and will take longer to quench completely.

In episode 15 (samples ρ11, ρ09, and ρ07, Figure 5.4), minor variations in density (Figure 5.4c) and componentry (Figure 5.5a) correlate with the median grain size, maximum clast size, and increasing stratigraphic height (Figure 5.4b). Density distributions for ρ11 and ρ09 (Figure 5.4c) are similar, with a mean near 500 kg m^{-3} corresponding to the two maximum-grain-size intervals in episode 15 (Figure 5.4b). Mean density shifts to slightly higher values at the end of the eruptive episode in sample ρ07 (650 kg m^{-3}). As the episode 15 eruption progressed, there was a slight increase in both pumice and T_O clasts, the latter with the highest density of any component, suggesting an increasing proportion of cone material failing and sliding into the vent.

The stratigraphic break at ~43 cm depth is inferred to represent the first material deposited during episode 16. Low spattering in the vent lasted only 20 minutes at the start of episode 16 before the fountain reached heights sufficient (~100 m) to result in deposition at the study site (Figure 5.1). The volume of lava that drained back into the vent after episode 15 was ~3.2 million m^3 (Richter et al., 1970) some of which must have been cleared from the conduit during the first 20 minutes of low fountaining in episode 16. However, degassed, drained-back lake lava was probably still being expelled from the vent when high fountaining ensued. The fountain steadily increased from ~100 to 460 m in height over 25 minutes, producing the layer between 40 and 43 cm depth (Figure 5.4a). Coincidently, clasts from this stratigraphic level contain the greatest

frequency (80%) and largest patches (up to 1.5 cm diameter) of MLR regions, which are probably portions of drained-back lake lava.

Episode 16 samples (ρ05, ρ03, and ρ01, Figure 5.4) vary more than episode 15 in componentry, grain size and density. The earlier-erupted samples, ρ05 and ρ03, have mean densities of ~700 kg m^{-3} and correspond to the maximum-sized clasts deposited. However, mean density increases to near ~900 kg m^{-3} and grain size decreases (Figure 5.4b, c) at the close of the last high-fountaining phase of the entire eruption. Additionally, clasts in the last erupted sample include the full range of clast morphologies, indicating a greater variety of thermal histories for individual clots of magma. At the close of the high fountaining, contemporary videos show the lava lake interacting with the fountain, resulting in large spurts in height and therefore, greater variety in residence times for clasts within the more wildly-fluctuating fountain.

5.5.2 Interpretation of microscopic data

5.5.2.1 Similarities in clast vesicle data
Although clasts vary in vesicularity and morphology, they were all derived from the same parent magma and exhibit some common properties. Vesicle number densities span less than an order of magnitude (3.9×10^{6} cm^{-3} to 1.8×10^{7} cm^{-3}, Table 5.1), indicating similar early vesiculation history within the conduit. The dominance of spherical vesicles in all clasts suggests that although coalescence likely contributed to relatively larger vesicle sizes, most vesicles were able to relax back to spherical forms prior to quenching.

135

5.5.2.2 Variability in clasts across the range of vesicularity

In Chapter 4, I interpret the high number densities and low vesicularities of fluidal clasts from episode 1 as indicating that clasts of this type quenched relatively early and preserve a record of the vesiculation state of magma near the time of fragmentation. The high-vesicularity, pumiceous clasts with fewer and larger bubbles appear to have undergone significant post-fragmentation expansion, presumably in the thermally-insulated core of the fountain. Transitional clasts were interpreted as representing quenching at intermediate points along a post-fragmentation path of growth and coalescence of bubbles within clasts inside the fountain. The episodes 15 and 16 clasts define similar trends on the number density versus V_G/V_L diagram (Figure 5.10), and thus we infer a similar history to apply to these clast categories in the episodes 15 and 16 deposits. The distribution of vesicle sizes in clasts of low to high vesicularity (Figure 5.11) indicates that the earliest-quenched, smallest vesicles are within low-vesicularity clasts, whereas the high-vesicularity clasts lack small vesicles and contain relatively abundant larger-diameter vesicles. Clasts with small vesicles have low vesicularity (Figure 5.11) and traveled along the fountain periphery quenching shortly after fragmentation (Sparks et al., 1997). Pumice forms the highest-vesicularity clasts (~85–93 %) in the products of the 1959 eruption, and are only slightly less vesicular than reticulite (≥95 %) from Puʻu ʻŌʻō in 1983-86, inferred to have expanded within the core of a Hawaiian fountain (Mangan and Cashman, 1996; Chapter 4). Assuming these high-vesicularity clasts were erupted with similar N^m_{Vtot} as low-vesicularity clasts, some coalescence must have occurred after fragmentation and within the fountain (Chapter 4) to achieve lower N^m_{Vtot} at the time of quenching (Figure 5.10).

5.5.2.3 Interpretation of vesicle number densities

Number densities are, on average, lower in clasts from episode 16 than episode 15

(Figures 5.9, 5.10, N^m_{Vtot} in Table 5.1). This assessment strengthens the argument that

vesicle number density scales with intensity of activity (Polacci et al., 2006; Sable et al.,

2006), since we know that episode 15 produced higher fountains than episode 16.
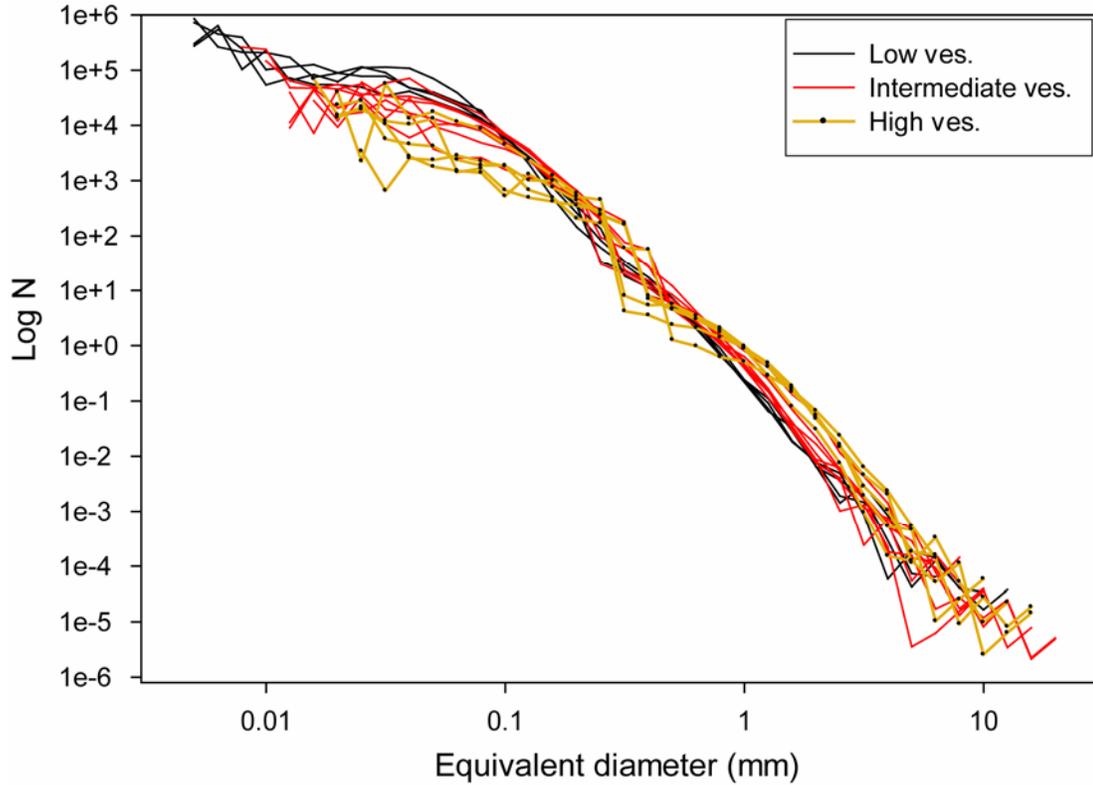
Figure 5.11 Number of vesicles per equivalent diameter bin for episode 15 and 16 clasts. Number of vesicles (N), low-vesicularity clasts represented by the black line contain the smallest vesicles of all clasts and intermediate- to high-vesicularity clasts contain the most abundant large vesicles.

5.5.2.4 Glass chemistry within zones and microlite textures

Major element analysis of heterogeneous zones defined by vesiculation and lack or

presence of microlites yield very similar compositions (Table 5.1). MV, LV, and MLF

glass chemistries are identical and represent the same batch of magma. Because the

chemistry is identical in MV and LV zones, we cannot correlate these regions to two

137

separate batches of magma with varying initial volatile contents. The variation in values between glass in MLR and MLF regions can be explained by crystallization of the enclosed plagioclase and pyroxene microlites.

Although some clasts have MLR and MLF zones, vesicle size and shape are generally consistent between the two regions in the same clast. In order to form fasciculate intergrowths of pyroxene and plagioclase microlites, MLR regions cooled slowly enough that pyroxene, which will crystallize alone and first at fast cooling rates, grew in combination with plagioclase due to suppressed supercooling and a reduced temperature separation between the two phases (Walker et al., 1978). We interpret this to have occurred in the lava lake, where sufficient cooling time resulted in coprecipitation of both minerals. Lava lake material that drained back into the vent, mingled with hot, previously unerupted, magma and was re-erupted during later fountaining. The incorporated lava lake material must have been hot and fluid when mixed with conduit magma, because blobs of melt from within MLR zones intruded into the lighter-colored adjacent MLF glass. Furthermore, to maintain similar vesicle textures between the two zones, drained-back melt must retain a primary vesicle population in addition to residual dissolved H_2O that can undergo further outgassing when re-erupted (Gerlach, 1986).

Microlite stringers contain only dendritic or spherulitic pyroxene, which can be attributed to rapid formation relative to the MLR fasciculate textures. Cooling experiments on lunar picritic (Walker et al., 1976) and quartz normative basalt (Grove and Raudsepp, 1978) indicate feldspar formation is suppressed relative to pyroxene when the cooling rate is high and crystallization occurs rapidly. Additionally, Walker et al.

138

(1978) found that differential cooling at fast rates results in pyroxene crystallization

without the interference of plagioclase. The spatial limitation and dendritic texture of the

pyroxene stringers indicates that they formed rapidly in the melt in which they reside, not

during previous cooling and incorporation like the MLR zones.   The dendritic pyroxene

microlites along the edges of MLR zones indicate to rapid crystallization relative to the

interior and are likely formed when the cooler MLR patch contacted the MLF melt and

acted to supercool the MLF melt and induce pyroxene dendrite crystallization.

5.6 Discussion

5.6.1 Contrasts between extremely-high (episodes 15 and 16) and high (episode 1) lava
fountains

5.6.1.1 Variability in clast componentry and extent of post-fragmentation expansion
There is a greater variety of clast types in deposits from episodes 15 and 16 than in those

from episode 1 (Figure 5.5). Clast morphology differences are imparted after

fragmentation and while traveling in the fountain (Chapter 4), suggesting that there was

more thermal variability in the extremely high fountaining episodes. There are fewer

pumice and more fluidal clasts in episode 1 tephra, indicating a combination of more

abundant low-angle trajectory clasts that cooled at the fountain periphery and lesser

amounts of fully expanded clasts from within the fountain core. For episode 1, fountain

heights never reached more than ~380 m and averaged near ~250 m for most of the

episode. However, episodes 15 and 16 produced fountains that peaked at ~580 m and

~460 m, respectively, and were sustained near 300 m height. Higher fountains yield a

prolonged period of thermal insulation for clasts, resulting in higher proportions of

pumice in the episode 15 and 16 tephra. Additionally, the higher fountains consisted of

larger clasts (Richter et al., 1970), which retain sufficient heat to impart breadcrust margins to larger transitional clasts and bombs. The greater magma ascent rates resulted in higher fountains and longer fountain-residence times, even for the clasts located around the perimeter, resulting in enhanced post-fragmentation vesiculation prior to quenching and limited fluidal textures. The absence of T_O clasts in episode 1, and their occurrence in the latter episodes, is a simple factor of the over-steepened geometry of the much larger cone resulting in frequent sliding of inner-wall material back into the vent in later episodes.

5.6.1.2 Variability in vesicle size for similar vesicularity clasts
The dominant vesicle size is smaller and the V_G/V_L is larger in the extremely high fountaining episodes. The lowest vesicularity clasts from episode 1 tephra have a dominant vesicle diameter of ~0.25 mm, whereas similar vesicularity clasts from episodes 15 and 16 tephra have vesicle size peak at 0.1 mm. This trend is consistent among all similar V_G/V_L clasts of the two comparable fountain-height deposits; there is always a smaller vesicle size peak in the episode 15 and 16 clasts. We previously interpreted greater degrees of thermal insulation and therefore post-fragmentation expansion for the extremely high lava fountains. Therefore, the higher fountaining episodes must have continued to nucleate bubbles longer relative to the lower fountaining, first episode of the eruption. In order to achieve smaller dominant vesicle populations, despite evidence for significant bubble coalescence for similar clast types across the two types of episodes,

5.6.2 Controls on extremely high fountaining behavior

To achieve the high fountain heights of the 1959 Kīlauea Iki eruption, the magma must have been erupted at great velocities. Fountain height increases with the mass fraction of exsolved volatiles (Sparks et al., 1997) but can be limited by the degree of coupling between the gas and melt phases (Parfitt and Wilson, 1995) as well as the influence of an overlying lava lake (Wilson et al., 1995). VNDs for the Kīlauea Iki eruption are high and indicate sufficient exsolved volatiles to drive the observed lava fountains to sustained heights between 200 – 400 m (Richter et al, 1970). The range of N^m_{Vtot} for episode 1 is encompassed within those for episodes 15 and 16, but is lower on average (Table 5.1). Overall, N^m_{Vtot} values are highest for episode 15, the highest-fountaining episode of the eruption. Therefore, it appears that higher-fountaining episodes are associated with greater degrees of nucleation during eruption which results in higher conduit ascent rates.

5.7 Conclusion

This study of the last two high-fountaining episodes of the 1959 eruption gives further evidence of post-fragmentation processes occurring within Hawaiian fountains (Mangan and Cashman, 1996; Chapter 4). Clast morphology and vesicularity correlate with VND across both episodes (Figure 5.10) and indicate that the number density of vesicles decreases as a result of coalescence when erupted material experiences greater degrees of post-fragmentation expansion within the fountain.

Episode 15 and 16 clasts contain varying percentages of secondary microlite aggregates composed of previously erupted material, which is absent in the products from episode 1. Microlite-rich (MLR) zones in clasts must have cooled slowly enough to form fasciculate textures and were therefore probably not quenched rapidly after eruption.

141

Based on these factors, MLR zones must be remnants of lake lava melt that drained back into the vent and were incorporated into newly vesiculating primary melt.

A question remains regarding the factors leading to termination of fountaining episodes at Kīlauea Iki and other Hawaiian eruptions. It has been assumed that encroachment of partially-degassed lake lava into the vent at Kīlauea Iki added sufficient overpressure to the conduit to inhibit further vesiculation of magma (Eaton et al., 1987). Wilson et al. (1995) use parameters from the Kīlauea Iki eruption to model the effect of vent-confining lava ponds on fountain height and determined that fountain height decreases as overlying pond depth increases. During Hawaiian activity, the fountain entrains relatively-degassed, and therefore higher-density lava as it erupts through the ponded material. Therefore, it is conceivable that continued eruption and deepening of lava overlying the vent at Kīlauea Iki acted to suppress the fountain sufficiently so that gas exsolution from primary magma could no longer overcome the confining pressure imparted by the entrainment of increasing amounts of high-density material. However, this does not explain why cessation of fountaining in episodes 15 and 16, as well as in other episodes, occurred abruptly rather than gradually.

Based on this and the study of episode 1 tephra (Chapter 4), the vesicle population preserved in lapilli originates from late exsolution of volatiles, principally H_2O (Gerlach, 1986; Wilson et al., 1995), which is the controlling factor for the rate of late-stage ascent and high fountaining. Assuming that exsolution of this gas phase occurred within the last ~120 m of the surface (Mangan and Cashman, 1996), we must presume that another process transported the magma to this depth from the storage region. Eaton et al. (1987)

142

suggest that between fountaining stages, reservoir exsolution of CO_2, and the resulting formation of a gas phase, would reduce the density of reservoir magma by $5 - 10$ percent and cause gravitational rise of gas-rich magma. Between fountaining stages, reservoir pressure was enhanced by the influx of volatile-rich magma from depth, the resulting formation of CO_2-rich gas inclusions, and also by drainback of lava from the lake. If initial magma rise was most affected by the exsolution and decoupling of an earlier exsolved volatile species, it is possible that a stage of fountaining comes to an end when the supply of this gas is exhausted. However, excess pressure within the reservoir was also relieved as magma was erupted during each episode. At this stage it is unclear which of these factors, or perhaps a combination of encroachment of lava into the vent, exhaustion of primary exsolved gas phase, or decrease in reservoir pressure resulted in the termination of fountaining at Kīlauea Iki.

What is known, however, is that later in the eruption enhanced reservoir pressure, resulting from the combined drainback of lake lava and influx of magma from depth, caused a dike-like zone to open in the region of the upper east rift zone (Eaton et al. 1987). As the Kilauea Iki eruption proceeded and the reservoir pressure built, more lava was forced into the east rift zone (Eaton et al. 1987) during later stages of drainback. It is possible that this pathway became well established, and by the end of the final episode, was being utilized as the dominant magma passage away from the summit reservoir. The Kīlauea Iki conduit then ceased to be utilized, and the eruption ended. In mid-January the pressurized east-rift zone erupted at Kapoho.

143

CHAPTER 6

Conclusions

6.1 Summary

This dissertation has evaluated lava lake processes and eruption dynamics during the

1959 Kīlauea Iki eruption at Kīlauea volcano.

Part of the surface of the Kīlauea Iki lava lake preserves the frozen record of a

final, incomplete, crustal-overturn cycle. Mapping this region and sampling, and

measuring density of, portions of the foundering crust, as well as the overriding and

underlying lava, shows how the process is driven by large differences in the density of

the foundering crust relative to the over-riding and under-lying lava (200 and 720 kg m^{-3}

respectively). These differences led, inevitably, to frequent crustal renewal: the density

differences make the upper layers of the lake highly unstable.

During repeated episodes in 1959, a cyclic pattern of lake filling to above vent

level, followed by drainage back to vent level, preserved features associated with both

filling and draining. These features can be described and characterized, on length scales

from centimeters to hundreds of meters, in a fashion analogous to descriptions of lava

flows. A vertical rind of lava coating the lake walls formed during each filling stage as

the lake deepened and lava solidified against vertical faces. Rind thickness from the top

to bottom of vertical faces increases due to greater submergence time for the lower

portions of the lake walls. Simple thermal diffusion calculations indicate that the 18

hours available during episode 16 drainage corresponds to the time needed to form the

associated ~20-cm-thick central portion of the outermost rind. Each drainage of the lake

resulted in uneven formation of sub-horizontal lava shelves on the lakeward edge of the vertical rinds; the shelves correlate with stable, staggered lake stands. Shelves formed in two ways: as broken relict slabs of lake crust that solidified in contact with the wall, or by accumulation, accretion, and widening at the lake surface in a dynamic lateral flow regime. Thin discontinuous lava shelves reflect an initially dynamic environment with rapid lake lowering. Slower and more staggered drainage is accompanied by the formation of thicker, more laterally continuous shelves. This study was the first to explore the formation of such features along the margins of a lava lake. These processes may occur at all lava lakes experiencing stages of filling and draining and form similar sets of features. Measuring vertical rinds and lava shelves, even remotely using capabilities such as LIDAR, at active or ancient lava lakes would result in a more sophisticated understanding of dynamics occurring for other lava lake systems.

The process of post-fragmentation expansion of bubble populations exerts a substantial overprint on the pre-fragmentation vesicle textures and size distributions in the products of Hawaiian fountaining eruptions. Comparison of the quenched rinds and expanded cores of individual clasts from episode 1 of the 1959 eruption allows study of these processes occurring on short length scales. Lower vesicle number density and larger bubble diameters in clast interiors can be modeled as a combination of continued free growth and coalescence of a bubble population. I have been able to use quantitative data to infer similar histories for clasts that lack preserved rinds. The sole remaining strong evidence of the conditions in the shallow conduit that led to sustained fountaining is high vesicle number densities recorded from all episode 1 clasts, even those

145

substantially affected by post-fragmentation vesiculation processes. Values of 3.8×10^6 cm^{-3} to 1.6×10^7 cm^{-3} are significantly higher than those for Strombolian explosions and other documented Hawaiian deposits and imply a similar mechanism of mechanical coupling of the late-exsolved water-rich portion of the magmatic volatiles in the shallow conduit.

Pyroclastic products from the last, and extremely high fountaining, episodes of the Kīlauea Iki eruption, episodes 15 and 16, differ from those of episode 1 due to greater vesicle abundances and the presence of microlite enclaves in the ejecta. Vesicle number density scales with the height of the lava fountains, and episode 15 clasts consistently have greater VND (average = 1.1×10^7 cm^{-3}) than do episode 16 clasts (average = 7.4×10^6 cm^{-3}). Because of the higher fountain heights, clast residence time was longer within the fountain during episodes 15 and 16 than during episode 1 resulting in a greater variety of clast morphologies with higher V_G/V_L ratios when compared to episode 1. Bubble nucleation time was prolonged until closer to the surface, therefore occurring over a greater depth range, in the closing episodes as evident by the smaller peak vesicle sizes within the products of extremely-high fountains. Patches rich in intergrown pyroxene and plagioclase microlites within golden glass are interpreted remnants of drained-back lava lake material that mingled with newly-arrived vesiculating melt within the conduit and reservoir.

6.2 Limitations on current research

6.2.1 Tephra size and coarsest vesicle populations
The lapilli used for analysis do not capture vesicle populations larger than a few cm in diameter. The largest clasts of Kīlauea Iki tephra are fragile bombs; based on occurrence of broken surfaces on individual clasts, most of the pyroclasts probably broke upon landing. Additionally, when sampling the episode 15 and 16 deposits, the largest clasts often break. Based on examination of sampled intact clasts, the bombs from episodes 15 and 16 contain vesicles up to 10 cm diameter. Larger vesicles can also be seen as imprints on the exteriors of lapilli. Other than limitations in sampling the largest clasts, and therefore the largest intact vesicles, the very largest bubble populations are probably destroyed during eruption. The gas fraction represented by these vesicles may play an important role in transportation of magma to the depth where excess nucleation results in the smaller population of vesicles characterized in my research. However, some of the larger vesicles in breadcrust bombs are likely to have formed as a result of post-fragmentation growth and coalescence.

One potential way to capture this vesicle population is to examine more closely large intact bombs from episode 15 and 16 tephra. These bombs could be carefully sawn in half and the cut surfaces scanned. Similar image processing methodologies could be used to characterize and analyze the size and distribution of large vesicles in bomb sized clasts. However, it would be difficult to infer pre-fragmentation dimensions of these vesicle populations because, to some degree, they would have expanded to their present size during post-fragmentation processes. Again, this limits the capacity of

147

understanding the geometry and distribution of large vesicles and an earlier exsolved gas phase within the conduit at Kīlauea Iki.

6.2.2 Gas partitioning in eruption dynamics

Based on the included vesicle studies from the 1959 Kīlauea Iki tephra, there are likely to be multiple phases of degassing that drive Hawaiian-style eruptions. Unfortunately, a lack of real-time gas studies associated with fountaining eruptions precludes knowing what types of volatile species are responsible for the buoyancy forces which initially cause magma to rise to the depth of H_2O-dominant vesiculation. If a gas species is causing the magma to rise it is most likely that CO_2 since SO_2 exsolves later than H_2O. To capture this gas speciation, it would be ideal to conduct simultaneous gas measurements, ejecta sampling, and video recording of fountain activity. Gas species such as SO_2, CO_2 and H_2O can be measured using remote sensing tools including: Airborne Visible/Infrared Imaging Spectrometer (AVIRIS), correlation spectrometer (COSPEC), nondispersive infrared sensor (NDIR), CO_2 analyzer, and (or) closed path Fourier Transform infrared spectrometer (CP-FTIR). If there were to be another easily accessible Hawaiian fountaining eruption at Kīlauea, real-time measurements of erupted gas species would help to constrain the amounts and types of degassing that produce feed into Hawaiian-style volcanism.

6.3 Ideas for future work

During the course of my research, many questions arose that were not addressed in the time available. If explored, they could lead to further understanding of processes associated with Hawaiian fountaining and lava lake processes.

My work has opened up the following avenues of future research:

1. Similar textural studies can be conducted on thin sections from pyroclasts associated with the high-fountaining episode 3. This would act as a mid-eruption comparison with the results from the microtextural studies of the opening and closing episodes that are included in this dissertation.

2. Detailed quantitative study of microlites within MLR zones and stringers in clasts would result in a more complete understanding of crystal formation. By quantification of the changing abundance and nature of the microlite types in prepared thin sections from episodes 3, 15 and 16, it may be possible to determine the timing and rates of microlite formation.

3. Thin sections could be made of remnant lava lake shelves to compare textures with those of the MLR zones within pyroclasts, thereby ensuring MLR zones are lava lake material. Shelves from the upper portion of the north margin wall would be the most appropriate for this comparison, because they represent lake lava that cooled during the initial stages of drainback. Timing of solidification of these shelves is therefore on par with the residence time of lava in the lake that drained back to form the MLR zones within pyroclasts.

4. Using the wealth of vesicle data acquired during the study of episode 1, 15 and 16, mathematical models can be created to quantify the specific amounts and timing for post-fragmentation growth and coalescence that occur within Hawaiian fountains.

5. Because Hawaiian fountains are thermally well insulated, it is impossible to use erupted pyroclasts to see the vesicle populations associated with conduit dynamics. Decompression experiments and associated vesicle studies of rapidly quenched tholeiitic basalt would help in understanding processes that lead to explosive Hawaiian-style volcanism.

Appendix

Field and laboratory research in addition to the work presented in this dissertation are

included as supplementary work within this appendix.

A.1 Lava lake high-stand ledge

There are two distinct sides of the lava lake: east and west. Much of the eastern lake is

characterized by flat pahoehoe microtopography, whereas the west lake surface is

composed of a jumbled mix of rheomorphic 'a'a flows mixed with shelly and slabby

pahoehoe. A continuous high-stand ledge surrounds the entire lake. A laser range finder

was used to make three cross sections from north to south through the east portion of the

lake. Each section end-point is separated by approximately 150 m along the lake's edge.

Figure A.1 shows that the height of the upper ledge is the same on both sides of the lake.

This level can be correlated to the 8th episode lake high stand equivalent to 126 m deep.

There is a second bench below the top that can probably be correlated to at least one if

not several of other lake high stands resulting from lake filling to 9 – 10 m lower than the

maximum depth attained in episode 8. This research was included in a poster

presentation at the Fall 2006 American Geophysical Union General Assembly meeting in

conjunction with preliminary results from lava shelves and rinds discussed in Chapter 3.
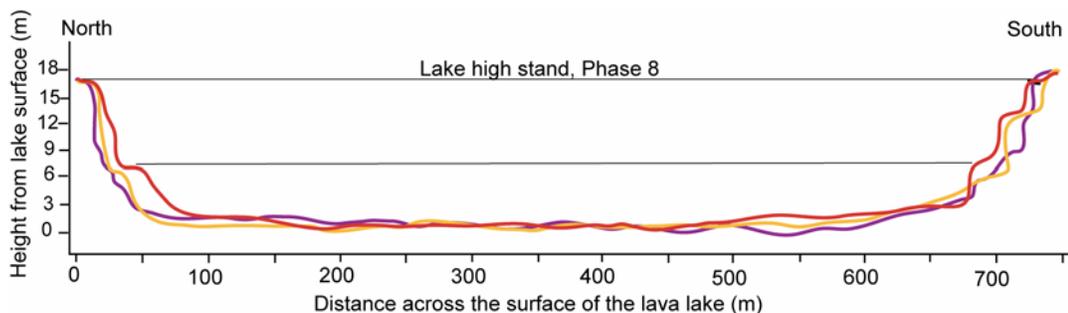
Figure A. 1 Lava lake surface cross sections

Measurements taken using a laser range finder. High stand correlates from north to south across the lake surface and was reached at the end of the fountaining phase of the 8th episode. Lower high stand marker between 7-8 m from lake surface must correlate to another lake high stand(s).

A.2 Kīlauea Iki episode 3 tephra density measurements

Samples additional to those from episodes 15 and 16 were collected for density

measurement from pit KI06-13 (Chapter 5). Samples $\rho14$ to $\rho30$ are determined to be

associated with episode 3, based on stratigraphic marker horizons found within KI06-13

and other tephra pits excavated prior to this study. Samples were sieved in the field to

collect the $16 - 32$ size fraction. Individual clast density measurements were made on 10

of these samples using the methods of Houghton and Wilson (1989) also discussed in

Chapter 4. Resulting density distributions are displayed in Figure A.2 and are labeled

with stratigraphic level.
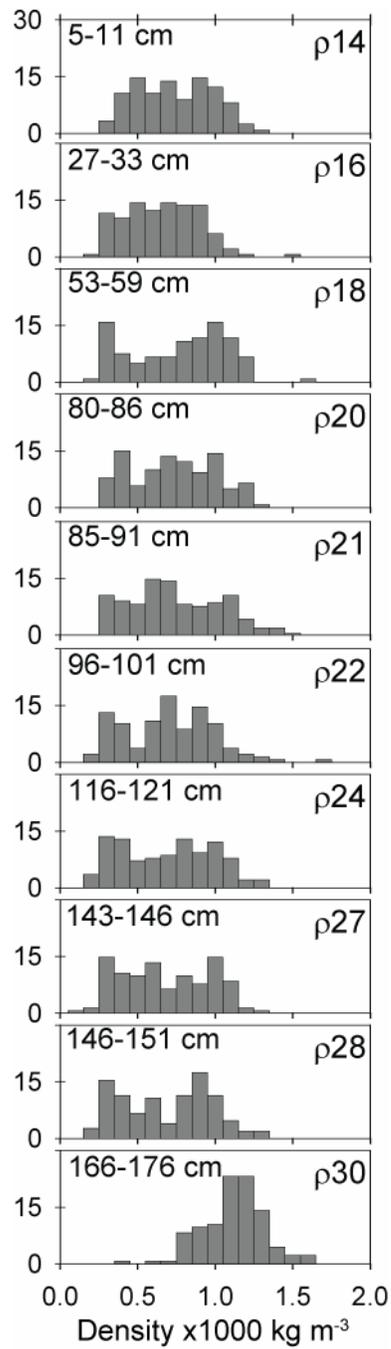
Figure A. 2 Episode 3 density measurements
Stratigraphic level inset on left and referenced to ashy parting at top contact of inferred episode 3 deposit. Sample number inset on right.

References

Adams, N.K., Houghton, B.F. and Hildreth, W., 2006. Abrupt transitions during
sustained explosive eruptions: examples from the 1912 eruption of Novarupta,
Alaska. Bulletin of Volcanology, 69: 189-206.

Alparone, S., Andronico, D., Lodato, L. and Sgroi, T., 2003. Relationship between tremor
and volcanic activity during the Southeast Crater eruption on Mount Etna in early
2000. Journal of Geophysical Research, 108: 2241-2254.

Anderson, A.T. and Brown, G.G., 1993. CO_2 contents and formation pressures of some
Kilauean melt inclusions. American Mineralogist, 78: 794-803.

Andronico, D., Cristaldi, A. and Scollo, S., 2008. The 4-5 September 2007 lava fountain
at South-East Crater of Mt Etna, Italy. Journal of Volcanology and Geothermal
Research, 173: 325-328.

Ault, W.U., Richter, D.H. and Stewart, D.B., 1962. A temperature measurement probe
into the melt of the Kīlauea Iki lava lake in Hawai'i. Journal of Geophysical
Research, 67: 2809-2812.

Barth, G.A., Kleinrock, M.C. and Helz, R.T., 1994. The magma body at Kīlauea Iki lava
lake: Potential insights into mid-ocean-ridge magma chambers. Journal of
Geophysical Research, 99: 7199-7217.

Bertagnini, A. Calvari, S., Coltelli, M., Landi, P., Pompilio, M., Scribano, V., 1990. The
1989 eruptive sequence. In: Barberi, F., Bertagnini, A., Landi, P. (Editors), Mt.
Etna: the 1989 eruption. Giardini, Pisa, pp. 10-22.

Bottinga, Y. and Weill, D.F., 1970. Densities of liquid silicate systems calculated from
partial molar volumes of oxide components. American Journal of Science, 269:
169-182.

Cashman, K.V. and Mangan, M.T., 1994. Physical aspects of magmatic degassing II:
Constraints on vesiculation processes from textural studies of eruptive products.
In: M.R. Carroll and J.R. Holloway (Editors), Volatiles in Magmas. Reviews in
Mineralogy. Mineralogical Society of America, Fredericksburg, pp. 447-478.

Chester, D.K., Duncan, A., Guest, J. and Kilburn, C.R.J., 1985. Mount Etna, The
Anatomy of a Volcano. Chapman and Hall, London.

Chouet, B. Saccorotti, G., Martini, M., Dawson, P., De Luca, G., Milana G., Scarpa, R.,
1997. Source and path effects in the wave fields of tremor and explosions at
Stromboli volcano, Italy. Journal of Geophysical Research, 102: 15129-15150.

Decker, R.W., 1987. Dynamics of Hawaiian volcanoes: an overview. In: R.W. Decker,
T.L. Wright and P.H. Stauffer (Editors), Volcanism in Hawai'i. U.S. Geological
Survey Professional Paper, 1350: 997-1018.

Duffield, W.A., 1972. A naturally occurring model of global plate tectonics. Journal of
Geophysical Research, 77: 2543-2555.

Dvorak, J.J. and Okamura, A.T., 1987. A hydraulic model to explain variations in summit
tilt rate at Kīlauea and Mauna Loa volcanoes. In: R.W. Decker, T.L. Wright and
P.H. Stauffer (Editors), Volcanism in Hawai'i. U.S. Geological Survey
Professional Paper, 1350: 1281-1296.

Eaton, J.P., 1959. A portable water-tube tiltmeter. Bulletin of the Seismological Society of America, 39: 301-316.

Eaton, J.P., 1962. Crustal structure and volcanism in Hawaiʻi. American Geophysical Union Monograph, 6: 13-29.

Eaton, J.P. and Murata, K.J., 1960. How volcanoes grow. Science, 132: 925-938.

Eaton, J.P., Richter, D.H. and Krivoy, H.L., 1987. Cycling of magma between the summit reservoir and Kīlauea Iki lava lake during the 1959 eruption of Kīlauea volcano. In: R.W. Decker, T.L. Wright and P.H. Stauffer (Editors), Volcanism in Hawaiʻi. U.S. Geological Survey Professional Paper, 1350: 1307-1334.

Eichelberger, J.C., 1995. Silicic Volcanism: Ascent of Viscous Magmas from Crustal Reservoirs. Annual Review of Earth and Planetary Sciences, 23: 41-63.

Eichelberger, J.C., Carrigan, C.R., Westrich, H.R. and Price, R.H., 1986. Non-explosive silicic volcanism. Nature, 323: 598-602.

Fedotov, S.A., Chirkov, A.M., Gusev, N.A., Kovalev, G.N. and Slezin, Y.B., 1980. The large fissure eruption in the region of Plosky Tolbachik volcano in Kamchatka, 1975-1976. Bulletin of Volcanology, 43: 47-60.

Fiske, R.S. and Kinoshita, W.T., 1969. Inflation of Kīlauea volcano prior to its 1967-68 eruption. Science, 165: 341-349.

Flynn, L.P., Mouginis-Mark, P.J., Gradie, J.C. and Lucey, P.G., 1993. Radiative temperature measurments at Kupaianaha lava lake, Kīlauea volcano, Hawaiʻi. Journal of Geophysical Research, 98: 6461-6476.

Frey, F.A. and Rhodes, J.M., 1983. Intershield geochemical differences among Hawaiian volcanoes: implications for source composition, melting processes and magma ascent paths. Philosophical Transactions of the Royal Society of London, 342: 121-136.

Gardner, J.E., Thomas, R.M.E., Jaupart, C. and Tait, S., 1996. Fragmentation of magma during Plinian volcanic eruptions. Bulletin of Volcanology, 58: 144-162.

Gerlach, T.M., 1986. Exsolution of H_2O, CO_2, and S during eruptive episodes at Kīlauea volcano, Hawai'i. Journal of Geophysical Research, 91: 12177-12185.

Grove, T.L. and Raudsepp, M., 1978. Effects of kinetics on the crystallization of quartz normative basalt 15597: an experimental study, Proceedings of the Lunar and Planetary Science Conference, 9: 585-599.

Gurioli, L., Harris, A.J.L., Houghton, B.F., Polacci, M. and Ripepe, M., 2008. Textural and geophysical characterization of explosive basaltic activity at Villarrica volcano. Journal of Geophysical Research, 113: B08206, doi: 10.1029/2007JB005328.

Gurioli, L., Houghton, B.F., Cashman, K.V. and Cioni, R., 2005. Complex changes in eruption dynamics during the 79 AD eruption of Vesuvius. Bulletin of Volcanology, 67: 144-159.

Harris, A.J.L., 2008. The pit-craters and pit-crater-filling lavas of Masaya volcano. Bulletin of Volcanology, doi: 10.1007/s00445-008-0241-y.

Harris, A.J.L., Carniel, R. and Jones, J., 2005. Identification of variable convective regimes at Erta Ale lava lake. Journal of Volcanology and Geothermal Research, 142: 207-223.

Head, J.W. and Wilson, C.J.N., 1987. Lava fountain heights at Puʻu ʻŌʻō Kīlauea, Hawaiʻi: Indicators of amount and variations of exsolved magma volatiles. Journal of Geophysical Research, 92: 13715-113719.

Head, J.W. and Wilson, C.J.N., 1989. Basaltic pyroclastic eruptions: Influences of gas-release patterns and volume fluxes on fountain structure, and the formation of cinder cones, spatter cones, rootless flows, lava ponds and lava flows. Journal of Volcanology and Geothermal Research, 37: 261-271.

Heliker, C. and Mattox, T.N., 2003. The first two decades of the Puʻu ʻŌʻō-Kupaianaha eruption: chronology and selected bibliography, The Puʻu ʻŌʻō-Kupaianaha eruption of Kīlauea volcano, Hawai`i: the first 20 years. U.S. Geological Survey Professional Paper, 1676: 1-27.

Heliker, C. and Wright, T.L., 1991. The Puʻu ʻŌʻō - Kupaianaha eruption of Kīlauea. Eos Transactions AGU, 72(47): 521.

Helz, R.T., 1987. Diverse olivine types in lava of the 1959 eruption of Kīlauea volcano and their bearing on eruption dynamics. In: R.W. Decker, T.L. Wright and P.H. Stauffer (Editors), Volcanism in Hawaiʻi. U.S. Geological Survey Professional Paper, 1350: 691-722.

Helz, R.T., 1993. Drilling report and core logs for the 1988 drilling of Kīlauea Iki lava lake, Kīlauea volcano, Hawaiʻi, with summary descriptions of the occurrence of

foundered crust and fractures in the drill core. Open File Report, U.S. Geological Survey 93-15: 1-57.

Helz, R.T. and Thornber, C.R., 1987. Geothermometry of Kīlauea Iki lava lake, Hawaiʻi. Bulletin of Volcanology, 49: 651-668.

Herd, R.A. and Pinkerton, H., 1997. Bubble coalescence in basaltic lava: its impact on the evolution of bubble populations. Journal of Volcanology and Geothermal Research, 75: 137-157.

Hon, K., Kauahikaua, J.P., Denlinger, R. and MacKay, K., 1994. Emplacement and inflation of pahoehoe sheet flows: observations and measurements of active lava flows on Kīlauea volcano, Hawaiʻi. Geological Society of America Bulletin, 106: 351-370.

Houghton, B.F. and Wilson, C.J.N., 1989. A vesicularity index for pyroclastic deposits. Bulletin of Volcanology, 51: 451-462.

Jaggar, T.A., 1947. Origin and Development of Craters. The Memoir Series, Memoir 21. Waverly Press, Inc., Baltimore, MD.

Jaupart, C., 1996. Physical models of volcanic eruptions. Chemical Geology, 128: 217-227.

Jaupart, C. and Vergniolle, S., 1988. Laboratory models of Hawaiian and Strombolian eruptions. Nature, 331: 58-60.

Jaupart, C. and Vergniolle, S., 1989. The generation and collapse of a foam layer at the roof of a basaltic magma chamber. Journal of Fluid Mechanics, 203: 347-380.

Karlstrom, L. and Manga, M., 2006. Origins and implications of zigzag rift patterns on lava lakes. Journal of Volcanology and Geothermal Research, 154: 317-324.

Keszthelyi, L., 1994. Calculated effect of vesicles on the thermal properties of cooling basaltic lava flows. Journal of Volcanology and Geothermal Research, 63: 257-266.

Klug, C. and Cashman, K.V., 1996. Permeability development in vesiculating magmas: implications for fragmentation. Bulletin of Volcanology, 58: 87-100.

Klug, C., Cashman, K.V. and Bacon, C.R., 2002. Structure and physical characteristics of pumice from the climactic eruption of Mount Mazama (Crater Lake), Oregon. Bulletin of Volcanology, 64: 486-501.

Lautze, N.C. and Houghton, B.F., 2007. Linking variable explosion style and magma textures during 2002 at Stromboli volcano, Italy. Bulletin of Volcanology, 69: 445-460.

Lovering, T.S., 1935. Theory of heat conduction applied to geological problems. Bulletin of the Geological Society of America, 46: 69-94.

Macdonald, G.A., 1962. The 1959 and 1960 eruptions of Kīlauea volcano, Hawaiʻi and the construction of walls to restrict the spread of the lava flows. Bulletin Volcanologique, 24: 249-294.

Macdonald, G.A., 1972. Volcanoes. Prentice Hall, Inc., Englewood Cliffs.

Macdonald, G.A., Abbott, A.T. and Peterson, F.L., 1983. Volcanoes in the Sea. University of Hawaiʻi Press, Honolulu.

Mangan, M.T., 1990. Crystal size distribution systematics and the determination of magma storage times: The 1959 eruption of Kīlauea volcano, Hawaiʻi. Journal of Volcanology and Geothermal Research, 44: 295-302.

Mangan, M.T. and Cashman, K.V., 1996. The structure of basaltic scoria and reticulite and inferences for vesiculation, foam formation, and fragmentation in lava fountains. Journal of Volcanology and Geothermal Research, 73: 1-18.

Mangan, M.T., Cashman, K.V. and Newman, S., 1993. Vesiculation of basaltic magma during eruption. Geology, 21: 157-160.

Marske, J.P., Pietruszka, A.J., Weis, D., Garcia, M.O. and Rhodes, J.M., 2007. Rapid passage of a small-scale mantle heterogeneity through the melting regions of Kīlauea and Mauna Loa volcanoes. Earth and Planetary Science Letters, 259: 34-50.

Mastin, L.G., Christiansen, R.L., Thornber, C.R., Lowenstern, J.B. and Beeson, M., 2004. What makes hydromagmatic eruptions violent? Some insights from the Keanakakoi Ash, Kīlauea volcano, Hawaiʻi. Journal of Volcanology and Geothermal Research, 137: 15-31.

Moore, J.G. and Clague, D.A., 1992. Volcano growth and evolution of the island of Hawaiʻi, GSA Bulletin, 104: 1471-1484.

Murata, K.J., 1966. An acid fumarolic gas from Kīlauea Iki, In: The 1959-60 Eruption of Kīlauea volcano, Hawaiʻi. U.S. Geological Society Professional Paper, 537-C: C1-C6.

Murata, K.J. and Richter, D.H., 1966. Chemistry of the lavas of the 1959-60 eruption of Kīlauea Volcano, Hawaiʻi. In: The 1959-60 eruption of Kīlauea volcano, Hawaiʻi. U.S. Geological Survey Professional Paper, 537-A: A1-A26.

Namiki, A. and Manga, M., 2008. Transition between fragmentation and permeable outgassing of low viscosity magmas. Journal of Volcanology and Geothermal Research, 169: 48-60.

Nichols, R.L., 1938. Grooved lava. Journal of Geology, 46: 601-614.

Nichols, R.L., 1939. Surficial banding and shark's-tooth projections in the cracks of basaltic lava. American Journal of Science, 237: 188-194.

Oze, C. and Winter, J.D., 2005. The occurrence, vesiculation, and solidification of dense blue glassy pahoehoe. Journal of Volcanology and Geothermal Research, 142: 285 - 301.

Parfitt, E.A., 1998. A study of clast size distribution, ash deposition and fragmentation in a Hawaiian-style volcanic eruption. Journal of Volcanology and Geothermal Research, 84: 197-208.

Parfitt, E.A., 2004. A discussion of the mechanisms of explosive basaltic eruptions. Journal of Volcanology and Geothermal Research, 134: 77-107.

Parfitt, E.A. and Wilson, L., 1995. Explosive volcanic eruptions IX. The transition between Hawaiian-style lava fountaining and Strombolian explosive activity. Geophysical Journal International, 121: 226-232.

Parfitt, E.A. and Wilson, L., 1999. A Plinian treatment of fallout from Hawaiian lava fountains. Journal of Volcanology and Geothermal Research, 88: 67-75.

Parfitt, E.A., Wilson, L. and Neal, C.A., 1995. Factors influencing the height of Hawaiian lava fountains: implications for the use of fountain height as an indicator of magma gas content. Bulletin of Volcanology, 57: 440-450.

Peck, D.L., 1978. Solidification of Alae lava lake. In: Cooling and vesiculation of Alae lava lake, Hawai'i. U.S. Geological Survey Professional Paper, 935-B: 1-59.

Peck, D.L. and Minakami, T., 1968. The formation of columnar joints in the upper part of Kilauean lava lakes, Hawai'i. Geological Society of America Bulletin, 79: 1151-1166.

Peck, D.L., Wright, T.L. and Moore, J.G., 1966. Crystallization of tholeiitic basalt in Alae lava lake, Hawai'i. Bulletin of Volcanology: 29: 629-655.

Pietruszka, A.J. and Garcia, M.O., 1999. The size and shape of Kīlauea volcano's summit magma storage reservoir: a geochemical probe. Earth and Planetary Science Letters, 167: 311-320.

Polacci, M., Burton, M.R., La Spina, A., Mure, R., Favretto, S., Zanini, F., 2009. The role of syn-eruptive vesiculation on explosive basaltic activity at Mt. Etna, Italy. Journal of Volcanology and Geothermal Research, 179: 265-269.

Polacci, M., Corsaro, R.A. and Andronico, D., 2006. Coupled textural and compositional characterization of basaltic scoria: insights into the transition from Strombolian to fire fountain activity at Mount Etna, Italy. Geology, 3: 201-204.

Poland, M. et al., 2008. New episodes of volcanism at Kīlauea volcano, Hawai'i. Eos Transactions AGU, 89(5), doi:10.1029/2008EO050001.

Rathbun, J.A., Spencer, J.R., Davies, A.G., Howell, R.R. and Wilson, L., 2002. Loki, Io; a periodic volcano. Geophysical Research Letters, 29(10): 84-1 - 84-4.

Richter, D.H., Eaton, J.P., Murata, K.J., Ault, W.U. and Krivoy, H.L., 1970. Chronological narrative of the 1959-60 eruption of Kīlauea volcano, Hawaiʻi. In: The 1959-60 eruption of Kīlauea volcano, Hawaiʻi. U.S. Geological Survey Professional Paper, 537-E: E1-E73.

Richter, D.H. and Moore, J.G., 1966. Petrology of the Kīlauea Iki lava lake Hawaiʻi. In: The 1959-60 eruption of Kīlauea volcano Hawaiʻi. U.S. Geological Survey Professional Paper, 537-B: B1-B26.

Richter, D.H. and Murata, K.J., 1966. Petrography of the lavas of the 1959-60 Eruption of Kīlauea Volcano, Hawaiʻi. In: The 1959-60 eruption of Kīlauea volcano Hawaiʻi. U.S. Geological Survey Professional Paper, 537-D: D1-D12.

Rupke, L.H. and Matthias, H., 2004. The impact of side wall cooling on the thermal history of lava lakes. Journal of Volcanology and Geothermal Research, 131: 165-178.

Sable, J.E., Houghton, B.F., Del Carlo, P. and Coltelli, M., 2006. Changing conditions of magma ascent and fragmentation during the Etna 122 BC basaltic Plinian eruption: Evidence from clast microtextures. Journal of Volcanology and Geothermal Research, 158: 333-354.

Sahagian, D.L. and Proussevitch, A.A., 1998. 3D particle size distributions from 2D observations - Stereology for natural applications. Journal of Volcanology and Geothermal Research, 84: 173-196.

Schenk, P. and Jackson, M.P.A., 1993. Diapirism on Triton: A record of crustal layering and instability. Geology, 21: 299-302.

Shaw, H.R., Kistler, R.W. and Evernden, J.F., 1971. Sierra Nevada plutonic cycle: part II, tidal energy and a hypothesis for orogenic-epeirogenic peridicities. Geological Society of America Bulletin, 82: 869-896.

Slezin, Y.B., 2003. The mechanism of volcanic eruptions. Journal of Volcanology and Geothermal Research, 122: 7-50.

Sparks, R.S.J. et al., 1997. Volcanic Plumes. John Wiley & Sons Ltd., Chichester.

Stearns, H.T., 1926. The Keaiwa or 1823 lava flow from Kīlauea volcano, Hawai'i. Journal of Geology, 34: 336-351.

Stovall, W.K., Houghton, B.F., Harris, A.J.L. and Swanson, D.A., 2008. A frozen record of density-driven crustal overturn in lava lakes: the example of Kīlauea Iki 1959. Bulletin of Volcanology, 71: 313-318.

Swanson, D.A., Duffield, W.A., Jackson, D.B. and Peterson, D.W., 1973. The complex filling of Alae Crater, Kīlauea volcano, Hawai'i. Bulletin of Volcanology, 36: 105-126.

Swanson, D.A., Duffield, W.A., Jackson, D.B. and Peterson, D.W., 1979. Chronological narrative of the 1969-71 Mauna Ulu eruption of Kīlauea volcano, Hawai'i. U.S. Geological Survey Professional Paper, 1056: 1-55.

Taddeucci, J., Pompilio, M. and Scarlato, P., 2004. Conduit processes during the July-August 2001 explosive activity of Mt. Etna (Italy): inferences from glass

chemistry and crystal size distribution of ash particles. Journal of Volcanology and Geothermal Research, 137: 33-54.

Tazieff, H., 1984. Mt. Niragongo: Renewed activity of the lava lake. Journal of Volcanology and Geothermal Research, 20: 267-280.

Tazieff, H., 1994. Permanent lava lakes: observed facts and induced mechanisms. Journal of Volcanology and Geothermal Research, 63: 3-11.

Thordarson, T., Self, S., Óskarsson, N. and Hulsebosch, T., 1996. Sulfur, chlorine and fluorine degassing and atmospheric loading by the 1783-1784 AD Laki (Skaftár Fires) eruption in Iceland. Bulletin of Volcanology, 58: 205-225.

Tilling, R.I., 1987. Fluctuations in surface height of active lava lakes during 1972-1974 Mauna Ulu eruption, Kīlauea volcano, Hawai'i. Journal of Geophysical Research, 92: 13721-13730.

Tilling, R.I. and Dvorak, J.J., 1993. Anatomy of a basaltic volcano. Nature, 363: 125-133.

Turcotte, D.L. and Schubert, G., 2001. Geodynamics. Cambridge University Press, Cambridge.

Vergniolle, S., 1996. Bubble size distribution in magma chambers and dynamics of basaltic eruptions. Earth and Planetary Science Letters, 140: 269-279.

Vergniolle, S. and Jaupart, C., 1986. Separated two-phase flow and basaltic eruptions. Journal of Geophysical Research, 91: 12842-12860.

Vergniolle, S. and Jaupart, C., 1990. Dynamics of degassing at Kīlauea volcano, Hawai'i. Journal of Geophysical Research, 95: 2793-2809.

Vergniolle, S. and Mangan, M.T., 2000. Hawaiian and Strombolian eruptions. In: H. Sigurdsson, B.F. Houghton, S. McNutt, H. Rhymer and J. Stix (Editors), Encyclopedia of Volcanoes. Academic Press, San Diego, pp. 447-461.

Walker, D., Kirkpatrick, R.J., Longhi, J. and Hays, J.F., 1976. Crystallization history of lunar picritic basalt sample 12002: phase-equilibria and cooling-rate studies. Geological Society of America Bulletin, 87: 646-656.

Walker, D., Powell, M.A., Lofgren, G.E. and Hays, J.F., 1978. Dynamic crystallization of a eucrite basalt. Proceedings of the Lunar and Planetary Science Conference, 9: 1369-1391.

Walker, G.P.L., 1973. Explosive volcanic eruptions - a new classification scheme. Geologische Rundschau, 62: 431-446.

Walker, G.P.L. and Croasdale, R., 1972. Characteristics of some basaltic pyroclastics. Bulletin of Volcanology, 35: 303-317.

Wilson, L., 1980. Relationships between pressure, volatile content and ejecta velocity in three types of volcanic explosions. Journal of Volcanology and Geothermal Research, 8: 297-313.

Wilson, L. and Head, J.W., 1981. Ascent and eruption of basaltic magma on the Earth and Moon. Journal of Geophysical Research, 86: 2971-3001.

Wilson, L., Parfitt, E.A. and Head, J.W., 1995. Explosive volcanic eruptions VIII. The role of magma recycling in controlling the behaviour of Hawaiian-style lava fountains. Geophysical Journal International, 121: 215-225.

Witham, F. and Llewellin, E.W., 2006. Stability of lava lakes. Journal of Volcanology and Geothermal Research, 158: 321-332.

Witter, J.B., Kress, V.C., Delmelle, P. and Stix, J., 2004. Volatile degassing, petrology and magma dynamics of the Villarrica Lava Lake, Southern Chile. Journal of Volcanology and Geothermal Research, 134: 303-337.

Worster, M.G., Huppert, H.E. and Sparks, R.S.J., 1993. The crystallization of lava lakes. Journal of Geophysical Research, 98: 15891-15901.

Wright, T.L., 1973. Magma mixing as illustrated by the 1959 eruption, Kīlauea volcano, Hawai'i. Geological Society of America Bulletin, 84: 849-858.

Wright, T.L. and Fiske, R.S., 1971. Origin of the differentiated and hybrid lavas of Kīlauea volcano, Hawai'i. Journal of Petrology, 12: 1-65.

Wright, T.L. and Kinoshita, W.T., 1968. March 1965 Eruption of Kīlauea Volcano and the Formation of Makaopuhi Lava Lake. Journal of Geophysical Research, 73: 3181-3205.

Wright, T.L. and Okamura, R.T., 1977. Cooling and crystallization of tholeiitic basalt, Makaopuhi lava lake, Hawai'i. U.S. Geological Survey Professional Paper, 1004: 1-78.

Yang, X., Davis, P.M., Delaney, P.T. and Okamura, A.T., 1992. Geodetic analysis of dike intrusion and motion of the magma reservoir beneath the summit of Kīlauea volcano, Hawai'i: 1970-1985. Journal of Geophysical Research, 97: 3005-3324.